ISSN 2587-1366

TUJE

TURKISH JOURNAL OF ENGINEERING

VOLUME 4 ISSUE 4 OCTOBER 2020

TURKISH JOURNAL OF ENGINEERING (TUJE)

Turkish Journal of Engineering (TUJE) is a multi-disciplinary journal. The Turkish Journal of Engineering (TUJE) publishes the articles in English and is being published 4 times (January, April, July and October) a year. The Journal is a multidisciplinary journal and covers all fields of basic science and engineering. It is the main purpose of the Journal that to convey the latest development on the science and technology towards the related scientists and to the readers. The Journal is also involved in both experimental and theoretical studies on the subject area of basic science and engineering. Submission of an article implies that the work described has not been published previously and it is not under consideration for publication elsewhere. The copyright release form must be signed by the corresponding author on behalf of all authors. All the responsibilities for the article belongs to the authors. The publications of papers are selected through double peer reviewed to ensure originality, relevance and readability.

AIM AND SCOPE

The Journal publishes both experimental and theoretical studies which are reviewed by at least two scientists and researchers for the subject area of basic science and engineering in the fields listed below:

Aerospace Engineering
Environmental Engineering
Civil Engineering
Geomatic Engineering
Mechanical Engineering
Geology Science and Engineering
Mining Engineering
Chemical Engineering
Metallurgical and Materials Engineering
Electrical and Electronics Engineering
Mathematical Applications in Engineering
Computer Engineering
Food Engineering

PEER REVIEW PROCESS

All submissions will be scanned by iThenticate® to prevent plagiarism. Author(s) of the present study and the article about the ethical responsibilities that fit PUBLICATION ETHICS agree. Each author is responsible for the content of the article. Articles submitted for publication are priorly controlled via iThenticate ® (Professional Plagiarism Prevention) program. If articles that are controlled by iThenticate® program identified as plagiarism or self-plagiarism with more than 25% manuscript will return to the author for appropriate citation and correction. All submitted manuscripts are read by the editorial staff. To save time for authors and peer-reviewers, only those papers that seem most likely to meet our editorial criteria are sent for formal review. Reviewer selection is critical to the publication process, and we base our choice on many factors, including expertise, reputation, specific recommendations and our own previous experience of a reviewer's characteristics. For instance, we avoid using people who are slow, careless or do not provide reasoning for their views, whether harsh or lenient. All submissions will be double blind peer reviewed. All papers are expected to have original content. They should not have been previously published and it should not be under review. Prior to the sending out to referees, editors check that the paper aim and scope of the journal. The journal seeks minimum three independent referees. All submissions are subject to a double blind peer review; if two of referees gives a negative feedback on a paper, the paper is being rejected. If two of referees gives a positive feedback on a paper and one referee negative, the editor can decide whether accept or reject. All submitted papers and referee reports are archived by journal Submissions whether they are published or not are not returned. Authors who want to give up publishing their paper in TUJE after the submission have to apply to the editorial board in written. Authors are responsible from the writing quality of their papers. TUJE journal will not pay any copyright fee to authors. A signed Copyright Assignment Form has to be submitted together with the paper.

PUBLICATION ETHICS

Our publication ethics and publication malpractice statement is mainly based on the Code of Conduct and Best-Practice Guidelines for Journal Editors. Committee on Publication Ethics (COPE). (2011, March 7). Code of Conduct and Best-Practice Guidelines for Journal Editors. Retrieved from http://publicationethics.org/files/Code%20of%20Conduct_2.pdf

PUBLICATION FREQUENCY

The TUJE accepts the articles in English and is being published 4 times (January, April, July and October) a year.

CORRESPONDENCE ADDRESS

Journal Contact: tuje@mersin.edu.tr

CONTENTS

Volume 4 – Issue 4

ARTICLES

Turkish Journal of Engineering

Turkish Journal of Engineering (TUJE)
Vol. 4, Issue 4, pp. 169-175, October 2020
ISSN 2587-1366, Turkey
DOI: 10.31127/tuje.631481
Research Article

TENSILE AND COMPRESSIVE BEHAVIORS OF THE PULTRUDED GFRP LAMINA

Yasin Onuralp Özkılıç [1], Emrah Madenci [2] and Lokman Gemi *[3]

[1] Necmettin Erbakan University, Faculty of Engineering and Architecture, Department of Civil Engineering, Konya, Turkey
ORCID ID 0000 – 0001 – 9354 – 4784
yoozkilic@gmail.com

[2] Necmettin Erbakan University, Faculty of Engineering and Architecture, Department of Civil Engineering, Konya, Turkey
ORCID ID 0000 – 0001 – 8279 – 9466
emadenci@erbakan.edu.tr

[3] Necmettin Erbakan University, Meram Vocational School, Konya, Turkey
ORCID ID 0000 – 0002 – 9895 – 6574
lgemi@erbakan.edu.tr

* Corresponding Author

Received: 09/10/2019 Accepted: 02/01/2020

ABSTRACT

The use of composite materials in civil engineering is increasing day by day due to their superior priorities such as high strength to weight ratio, high corrosion resistance, and durability. One of the recent materials used in the civil engineering application is pultruded glass fiber reinforced polymer (GFRP). Many studies are available in the literature related to the behavior of component (structural) level of the pultruded GFRP; however, very limited data is available related to the behavior of the lamina level of the pultruded GFRP. Since the behaviors of the pultruded GFRP in longitudinal and transverse directions are quite distinct, it is aimed to provide the tensile and compressive behavior of the pultruded GFRP in terms of stiffness, capacity and failure modes. Pursuant to this goal, longitudinal and transverse direction of the pultruded GFRP laminas were tested under both compressive and tensile forces according to ASTM standards. A total of 12 specimens, three replicates for each type, were tested. Moreover, these tests were modelled with the aid of Abaqus. The numerical and experimental results revealed that the transverse strength of pultruded GFRP is much weaker than its longitudinal strength for both compressive and tensile forces. While the damages in tensile tests started in micro dimension and continued as macro and the result of the damage was progressive damage, the rapid progression of damages in compression experiments led to the development of catastrophic damage.

Keywords: *Composite Material, Pultruded GFRP, Tensile, Compressive, Damage Analysis*

1. INTRODUCTION

Many studies are available in the literature related to use of composite material in civil engineering applications (Ozbakkaloglu, 2013; Kara *et al*. 2015; Kara *et al*. 2016; Gemi *et al*. 2018; Gemi *et al.* 2019; Madenci 2019; Özütok and Madenci, 2017; Madenci and Özütok, 2017; Özütok *et al.* 2014; Özütok and Madenci, 2013). One of the newest composite materials used in civil engineering applications is pultruded glass fiber reinforced polymer (GFRP) (Gemi and Köroğlu, 2018). GFRP composites produced by pultrusion method are used both as a main material and as complementary material in the field engineering area. This type of composite materials have a long-lasting strength compared to other materials, high performance against environmental factors, lightweight, resistance to corrosion effects, electricity insulation, low density, effective mechanical resistance use has increased gradually (Gemi *et al.* 2020; Gemi, 2018). Due to high demand to these advanced materials, the understanding of mechanical behavior of pultruded GFRP composite structures is important for design. The studies of the pultruded GFRP to use as a structural member such as column, beam and etc. are gained attention (Yu *et al*. 2016; Lokuge *et al*. 2019; Muttashar *et al.* 2016; Kara *et al*. 2019).

In addition to studies related to structural (component) level of the pultruded GFRP, a limited research on pultruded GFRP as lamina level has been found in the literature (Al-saadi *et al*. 2019; Haj-Ali and Kilic, 2002; Bai *et al*. 2008; Feo *et al*. 2012; Xin *et al*. 2017). Zhang *et al.* (2018) performed tensile tests to examine the effects of the fiber orientation on material properties of the pultruded GFRP. Eight different fiber orientations were studied and it is concluded that fiber orientation has significant effect on the mechanical properties of the pultruded GFRP. Al-saadi *et al.* (2019) conducted a series of experiments to determine mechanical properties of the pultruded GFRP with different fiber orientations of [0°, ±50°], [0°, ±45°], [0°, ±56°] and [0°, ±71°]. The result of the study revealed that strength and modulus of elasticity depend on the fiber orientation.

Production of multi-directional pultruded GFRP is rather stringent; therefore, uni-directional pultruded GFRP is generally manufactured due to the easy of production. In this study, single-layer pultruded GFRP composite laminas with fiber orientation of [0°] and [90°] were selected for experimental mechanic tests. Material properties are obtained by tensile and compressive tests according to ASTM standards. Modulus of elasticity, capacity and failure modes of pultruded GFRP composite laminas are analyzed and investigated. The specimens were cut out of the composite plates in the characteristic directions dictated by the fiber: (1) test in the direction of the fiber and (2) test in the direction transversal in the fiber.

2. EXPERIMENTAL STUDY

Tensile and compressive tests were conducted in order to obtain the mechanical properties of the pultruded GFRP composite, such as strengths and modulus of elasticity. The specimens were cut and tested according to ASTM standard test methods. The specimens are cut out of the composite plates in the characteristic directions dictated by the fiber: (1) test in the direction of one of the yarn systems of the fiber (warp/weft for woven fabrics; braiding/inlay yarns for braids); and (2) test in the direction transversal or bias to the direction of the yarn systems in the fiber (bias for woven fabrics, perpendicular to the production direction for braids). A total of twelve specimens which can be categorized into four groups are taken from the pultruded GFRP profile. Three specimens used in tensile test and three specimens are used in compressive test for each group (longitudinal direction: 0^{o} and transverse directions: 90^{o})

2.1. Tensile Test

The tensile test was performed according to ASTM D638 (Standard Test Method for Tensile Properties of Plastics). The test was conducted using a Shimadzu universal testing machine with a capacity of 100 kN. The test setup is depicted in Fig. 1. Tensile tests were conducted on the specimens with nominal dimensions of 250×25×6 mm (length-width-thickness) and 150×25×6 mm, in order to determine the tensile strength and the displacement in the longitudinal and transverse directions, respectively. The distances between the claws were 190 mm and 90 mm for longitudinal and transverse directions, respectively.

Fig. 1. Tensile test setup

2.2. Compressive Test

The compressive test is also conducted using Shimadzu universal testing machine and the test was performed according to ASTM D695 (Standard test method for compressive properties of rigid plastics). The test setup is illustrated in Fig. 2.

Fig. 2. Compressive test setup

In this case test speed is 1.5 mm/min. Compressive tests were conducted on the specimens with nominal dimensions of 150×25×6 mm (length-width-thickness) in both the longitudinal direction and the transverse direction, in order to determine the compressive strength and the displacements for both directions.

3. NUMERICAL STUDY

Numerical study was conducted in order to verify experimental results. The commercial software Abaqus was used to model compressive and tensile tests. Shell elements were utilized to mesh the pultruded GFRP. For this purpose S4R general purpose linear 4-sided shell element with reduced integration was used. Elastic properties of the pultruded GFRP was defined using elastic type of “Lamina”. Boundary conditions were defined to the region between the claws to simulate experimental study. The numerical model and boundary conditions are illustrated in Fig. 3.

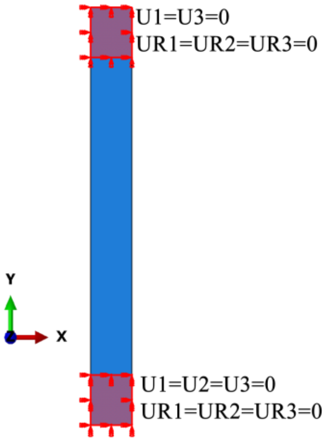

Fig. 3. The numerical model and boundary conditions

4. RESULTS

4.1. Tensile Test Results

Fig. 4 and Fig. 5 demonstrate the tensile test results of the longitudinal and transverse direction respectively as well as the numerical results. According to the test results, average modulus of elasticity is approximately 23 GPa and 7 GPa for longitudinal and transverse directions, respectively (Madenci *et. al.* 2020). The test results showed that the tensile strength of longitudinal direction was 7.25 times higher than that of transverse direction. The average tensile strengths of the specimens for the longitudinal and transverse direction are 290 MPa and 40 MPa, respectively. The numerical results are also substantiate to the experimental results.

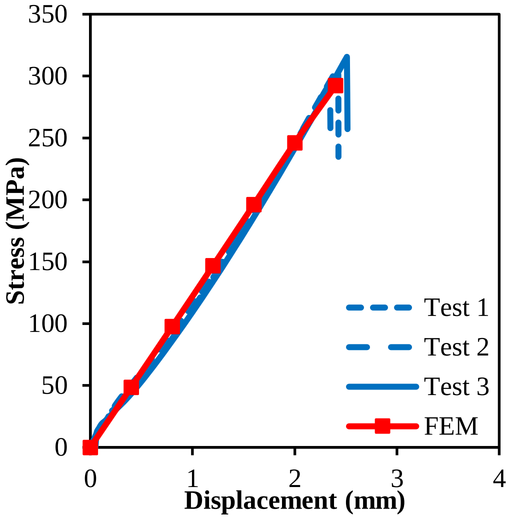

Fig. 4. The tensile test results of longitudinal direction

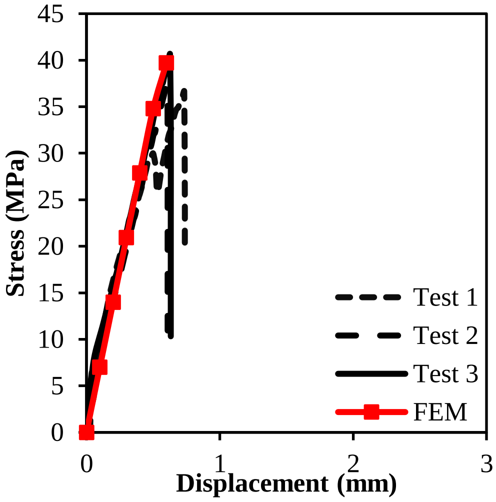

Fig. 5. The tensile test results of transverse direction

When the test results of the specimens (Fig. 4) and the photographs of the damage (Fig. 6) are investigated together, final failure was observed at stress value of 313 MPa and displacement value of 2.5 mm. Matrix crack sounds started to emerge at approximately 280 MPa stress and 2.26 mm displacement as initial damage. Addition to matrix cracks, it was observed that transfer cracks with debonding damage were occurred at the stress and displacement value close to final failure in (0°) fiber layers. As the loading continues, intra-interlaminar cracks occurred in the longitudinal direction and then fiber breakage together with veil damage has started to occur. As a result of fiber breaks in the other layers, final failure has occurred.

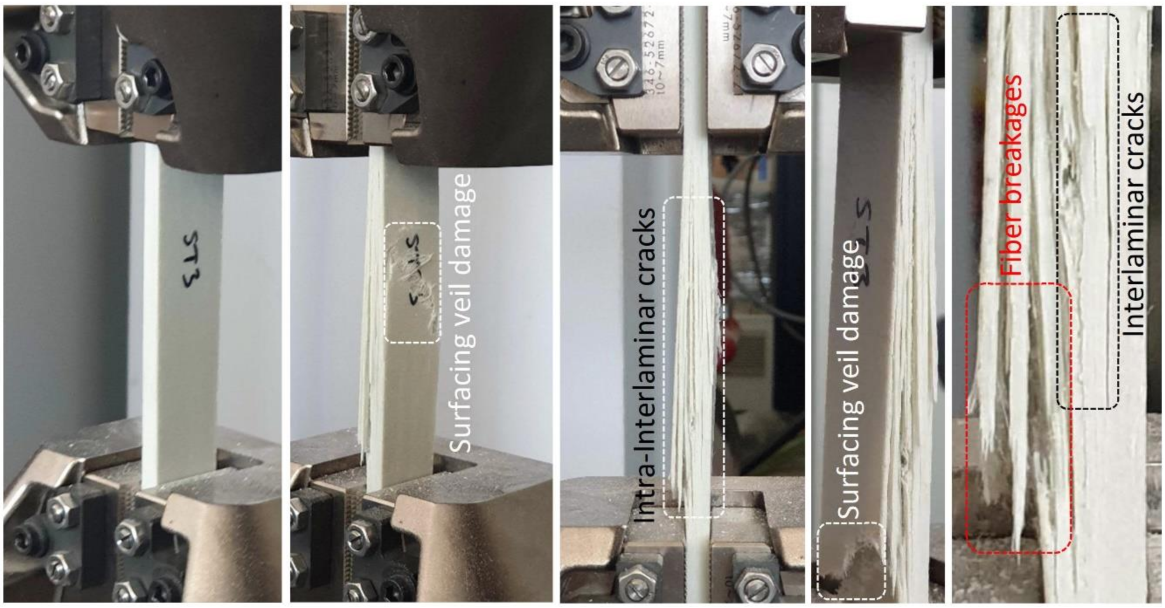

Fig. 6. Tensile test failure in the longitudinal direction

When the test results (Fig. 5) and the photographs of the damage (Fig. 7) of the specimens which were exposed to transverse tensile forces, maximum of 40.6 MPa stress and 0.62 mm displacement were observed among three specimens. Fluctuations at stress value of 35 MPa and displacement value of 0.5 mm were observed in the graph due to debonding damage occurring between the fibers perpendicular to the loading direction. Different from other specimens, debonding damage was observed at 29.7 MPa and 0.46 mm in Test 1. Matrix crack sounds were observed at same stress value in other specimens and it has continued to increase up to the resulting damage. While before debonding damage the load was carried together by (90°) fibers and veil surface, after debonding damage the load was carried by only veil surface. Damage to the transverse (90°) layer has progressed due to the damage occurred at randomly generated veil layers. Dense matrix damages were observed at cross section of the specimen as a result of separation of fiber matrix interfaces. The final failure for all three specimens was formed as splitting damage after surfacing veil damage.

4.2. Compressive Test Results

Fig. 8 and Fig. 9 demonstrate the compressive test results of the longitudinal and transverse direction, respectively. Test results revealed that compressive strength of longitudinal direction was much higher than that of transverse direction. Compressive strengths of the specimens for the longitudinal and transverse direction are 280 MPa and 85 MPa, respectively. Moreover, excellent correlation was obtained between numerical and experimental results.

The test results (Fig. 8) and the photographs of the damage (Fig. 10) of the specimens exposed to longitudinal compressive forces are investigated in detail. Maximum displacement (0.52 mm) and maximum stress (281 MPa) were obtained from Test 1. In compression tests, unlike tensile tests, after a certain stress value (about 250 MPa), deformation due to buckling was observed in the specimen. With the buckling damage, matrix crack sounds started to appear in the specimen.

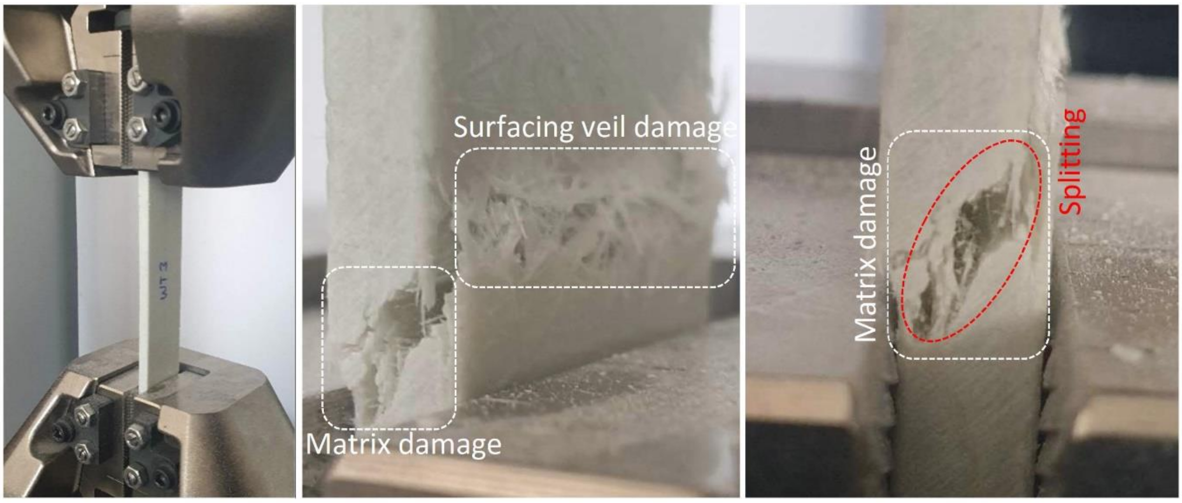

Fig. 7. Tensile test failure in the transverse direction

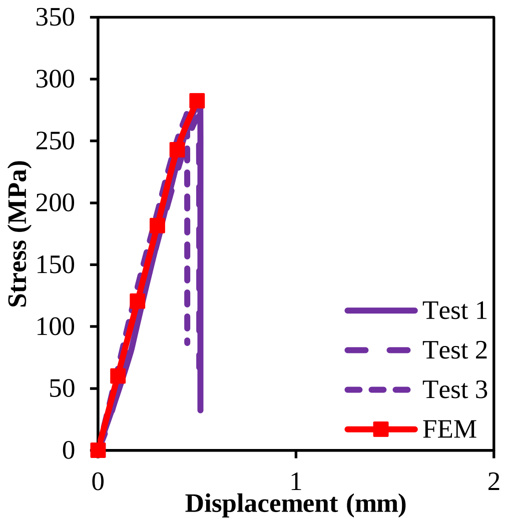

Fig. 8. The compressive test results of longitudinal direction

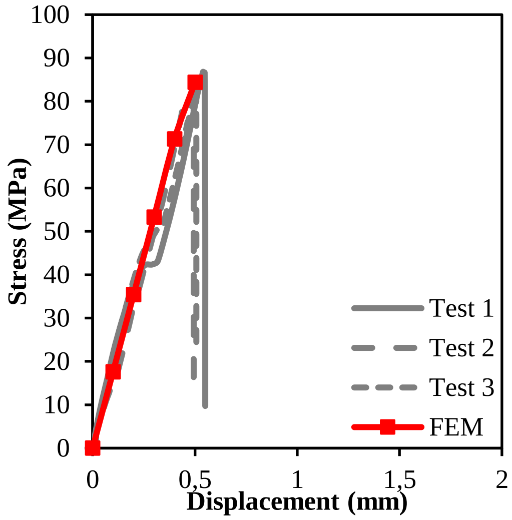

Fig. 9. The compressive test results of transverse direction

Local delamination damage has started to occur in the fiber direction between the layers and veil surfaces with the increase of intra-interlaminar cracks. At the maximum stress level, delamination damages on the specimen progressed rapidly and the final failure occurred. When the damage photographs are examined, the delamination between the layers and the interlayers formed by the effect of micro buckling on all layers is clearly observed. In the delamination zone, longitudinal direction (0°) fibers showed debonding damage, while fiber breakages were observed in the veil surfaces.

The test results (Fig. 9) and the photographs of the damage (Fig. 11) of the specimens which were exposed to transverse compressive forces are given. When Fig. 9 is examined, it is interpreted that debonding damage and matrix cracks occurred due to compression effect in transverse direction fiber layers at 39-53 MPa for Test 1 and 2, and at 76 MPa for Test 2. Despite the formation of debonding and matrix cracks, the veil surfaces surrounding the fiber layers (90°) continued to carry load. When the test graph of Test 1 is examined, it is seen that it represented better damage development during compression and the formation of matrix cracks in the stress value of 83 MPa at veil surfaces caused fluctuations in stress value. With the increase of the applied load, the debonding and matrix crack damages on the specimens were combined and the final failure was formed as splitting at an angle of 45°at 0.55 mm displacement and 86.6 MPa stress value. When the damage photographs given in Fig. 11 are examined closely, it is observed that there is intensive debonding and matrix cracks damages in transverse direction (90°) fibers and fiber breakage damages occur in the veil surfaces due to micro buckling. In all three specimens, the final failure can be interpreted as the damage caused by the transverse direction (90°) fibers which leads to splitting damage in the form of shear planes at an angle.

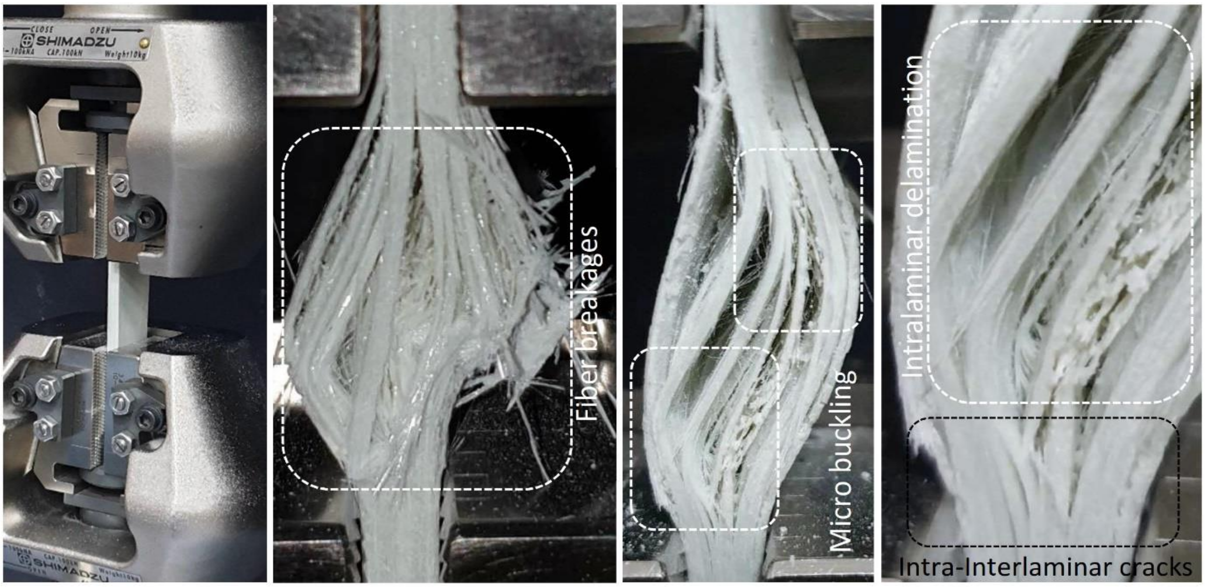

Fig. 10. Compressive failure in the longitudinal direction

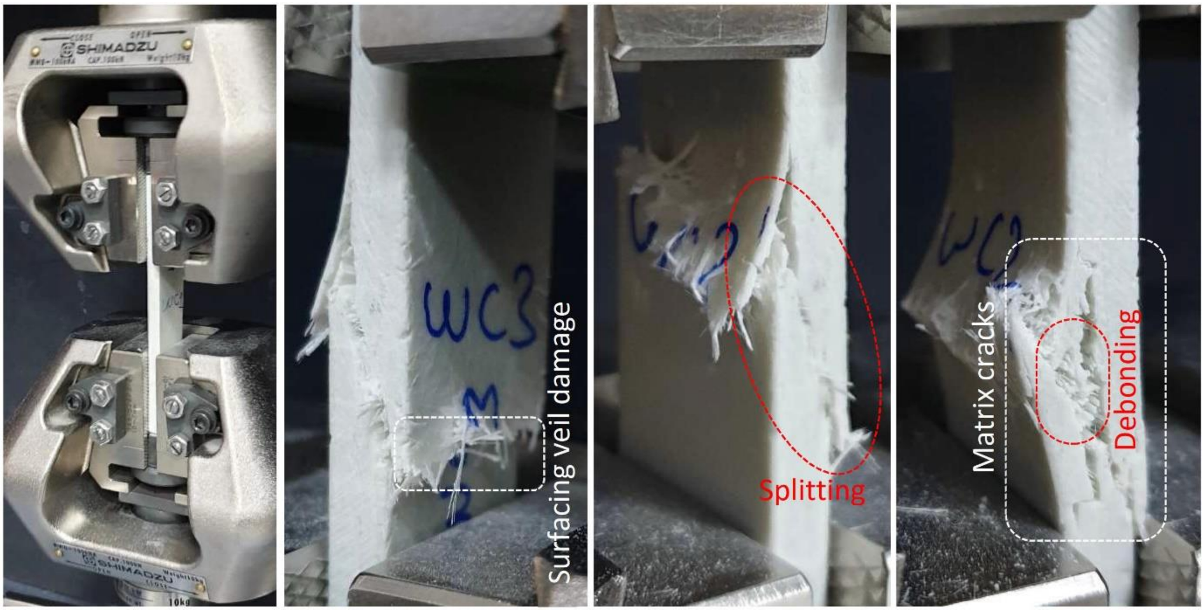

Fig. 11. Compressive test failure in the transverse direction

5. CONCLUSION

In this present study, the mechanical behavior of the pultruded GFRP laminas in terms of tensile and compressive behaviors was examined in detail. For this purpose, tensile and compressive tests were carried out. The following conclusions can be drawn from this study:

✓ The tensile strength and elastic modulus of pultruded GFRP in the transverse direction are very low compared to that of the longitudinal direction. The average tensile strength is 290 MPa and elastic modulus are 23 GPa for the longitudinal and 40 MPa and 7 GPa for transverse direction of pultruded GFRP beam, respectively.

✓ In all tensile tests, it was observed that the damage started with micro-matrix cracks and showed progressive damage in the form of fiber rupture after the formation of delamination in the micro-layer.

✓ The compressive strength of pultruded GFRP in the transverse direction is low compared to that of the longitudinal direction. The average compressive strengths are 280 MPa and 85 MPa for the longitudinal and transverse direction of pultruded GFRP beam, respectively.

✓ The tensile and compressive stress of longitudinal direction are very similar. The ratio of tensile stress to compressive stress in the longitudinal direction is 1.04. However, the compressive stress is more than twice tensile stress in transverse direction. The ratio of compressive stress to tensile stress in the transverse direction is 2.13.

✓ It was observed that the damages in the compression tests proceeded very fast in the specimens and the final failure occurred as catastrophic damage.

✓ In the longitudinal direction specimens, the damage modes that occur after compression and tensile tests are intense; matrix cracks, in-layer delamination, micro-buckling, and fiber break.

✓ Damage modes in transverse direction specimens; matrix cracks, debonding, dense matrix damage and splitting damage at 45° angle.

REFERENCES

Al-saadi, A. U., Aravinthan, T., and Lokuge, W. (2019). “Effects of fibre orientation and layup on the mechanical properties of the pultruded glass fibre reinforced polymer tubes.” *Engineering Structures*, Vol. 198, pp. 109448.

Bai, Y., Post, N. L., Lesko J. J., and Keller, T. (2008). “Experimental investigations on temperature-dependent thermo-physical and mechanical properties of pultruded GFRP composites.” *Thermochimica Acta*, Vol. 469, No. (1-2), pp. 28-35.

Bowlby, L. K., Saha, G. C., and Afzal, M. T. (2018). “Flexural strength behavior in pultruded GFRP composites reinforced with high specific-surface-area biochar particles synthesized via microwave pyrolysis.” *Composites Part A: Applied Science and Manufacturing* Vol. 110, pp. 190-196.

Feo, L., Marra, G., and Mosallam, A. S. (2012). “Stress analysis of multi-bolted joints for FRP pultruded composite structures.” *Composite Structures*, Vol. 94, No. 12, pp. 3769-3780.

Gemi, L., Kayrıcı, M., Uludağ, M., Gemi, D. S., and Şahin, Ö. S. (2018). “Experimental and statistical analysis of low velocity impact response of filament wound composite pipes.” *Composites Part B: Engineering*, Vol. 149, pp. 38-48.

Gemi, L., Köroğlu, M. A., and Ashour, A. (2018). “Experimental study on compressive behavior and failure analysis of composite concrete confined by glass/epoxy±55 filament wound pipes.” *Composite Structures*, Vol. 187, pp. 157-168.

Gemi, L., and Köroğlu, M. A. (2018). “Çekme bölgesi lifli beton olan cam fiber takviyeli polimer (GFRP) ve çelik donatılı etriyesiz kirişlerin eğilme etkisi altındaki davranışı ve hasar analizi.” *Selçuk Üniversitesi Mühendislik, Bilim ve Teknoloji Dergisi*, Vol. 6, No. 4, pp. 654-667.

Gemi, L., Aksoylu, C., Yazman, Ş., Özkılıç, Y. O., and Arslan, M. H. (2019). "Experimental investigation of shear capacity and damage analysis of thinned end prefabricated concrete purlins strengthened by CFRP composite." *Composite Structures,* Vol. 229, pp. 111399.

Gemi, L., Morkavuk, S., Köklü, U., and Yazman, Ş. (2020). "The effects of stacking sequence on drilling machinability of filament wound hybrid composite pipes: Part-2 damage analysis and surface quality." *Composite Structures,* Vol. 235, pp. 111737.

Gemi, L., Köklü, U., Yazman, Ş., and Morkavuk, S. (2020). "The effects of stacking sequence on drilling machinability of filament wound hybrid composite pipes: Part-1 mechanical characterization and drilling tests." *Composites Part B: Engineering,* Vol. 186, pp. 107787.

Gemi, L. (2018). "Investigation of the effect of stacking sequence on low velocity impact response and damage formation in hybrid composite pipes under internal pressure. A comparative study." *Composites Part B: Engineering,* Vol. 153, pp. 217-232.

Haj-Ali, R., and Kilic, H. (2002). "Nonlinear behavior of pultruded FRP composites." *Composites Part B: Engineering*, Vol. 33, No. 3, pp. 173-191.

Kara, I. F., Ashour, A. F., and Köroğlu, M. A. (2015). "Flexural behavior of hybrid FRP/steel reinforced concrete beams." *Composite Structures*, Vol. 129, pp. 111-121.

Kara, I. F., Ashour, A. F., and Köroğlu, M. A. (2016). "Flexural performance of reinforced concrete beams strengthened with prestressed near-surface-mounted FRP reinforcements." *Composites Part B: Engineering*, Vol. 91, pp. 371-383.

Kara, I., Ashour, A., Bilim, C. (2019). "Flexural Behavior of Hybrid FRP-Concrete Bridge Decks." *Turkish Journal of Engineering*, Vol. 3, No. 4, pp. 206-217.

Li, Z., Khennane, A., Hazell, P. J., and Brown, A. D. (2017). "Impact behaviour of pultruded GFRP composites under low-velocity impact loading." *Composite Structures,* Vol. 168, pp. 360-371.

Lokuge, W., Abousnina, R., and Herath, N. (2019). "Behaviour of geopolymer concrete-filled pultruded GFRP short columns." *Journal of Composite Materials,* Vol. 53, No. 18, pp. 2555-2567.

Ozbakkaloglu, T. (2013). "Compressive behavior of concrete-filled FRP tube columns: Assessment of critical column parameters." *Engineering Structures*, Vol. 51, pp. 188-199.

Madenci, E. (2019). "Refined functional and mixed formulation to static analyses of fgm beams." *Structural Engineering and Mechanics*, Vol. 69, No. 4, pp. 427-437.

Madenci, E., and Özütok, A. (2017). "Variational approximate and mixed-finite element solution for static analysis of laminated composite plates." *Solid State Phenomena*, Vol. 267, pp. 35-39.

Madenci, E., Özkılıç, Y. O., and Gemi, L. (2020). Experimental and Theoretical Investigation on Flexure Performance of Pultruded GFRP Composite Beams with Damage Analyses. *Composite Structures*, Vol. 242, pp. 112162.

Ozutok, A., Madenci, E., and Kadioglu, F. (2014). "Free vibration analysis of angle-ply laminate composite beams by mixed finite element formulation using the Gâteaux differential." *Science and Engineering of Composite Materials*, Vol. 21, No. 2, pp. 257-266.

Özütok, A., and Madenci, E. (2017). "Static analysis of laminated composite beams based on higher-order shear deformation theory by using mixed-type finite element method." *International Journal of Mechanical Sciences*, Vol. 130, pp. 234-243.

Özütok, A., and Madenci, E. (2013). "Free vibration analysis of cross-ply laminated composite beams by mixed finite element formulation." *International Journal of Structural Stability and Dynamics,* Vol. 13, No. 2, pp. 1250056-17.

Vieira, P.R., Carvalho, E.M.L., Vieira, J.D. and Toledo Filho, R.D. (2018). "Experimental fatigue behavior of pultruded glass fibre reinforced polymer composite materials." *Composites Part B: Engineering,* Vol. 146, pp. 69-75.

Yang, X., Bai, Y., Luo, F. J., Zhao, X. L., & Ding, F. (2016). "Dynamic and fatigue performances of a large-scale space frame assembled using pultruded GFRP composites." *Composite Structures*, Vol. 138, pp. 227-236.

Muttashar, M., Karunasena, W., Manalo, A., and Lokuge, W. (2016). "Behaviour of hollow pultruded GFRP square beams with different shear span-to-depth ratios." *Journal of Composite Materials,* Vol. 50, No. 21, pp. 2925-2940.

Zhang, S., Caprani, C., and Heidarpour, A. (2018). "Influence of fibre orientation on pultruded GFRP material properties." *Composite Structures*, Vol. 204, pp. 368-377.

Turkish Journal of Engineering

Turkish Journal of Engineering (TUJE)
Vol. 4, Issue 4, pp. 176-182, October 2020
ISSN 2587-1366, Turkey
DOI: 10.31127/tuje.639314
Research Article

LATMOS GEOPARK (BEŞPARMAK MOUNTAINS) WITH HERAKLEIA-LATMOS ANTIQUE HARBOUR CITY AND BAFA LAKE NATURAL PARK IN TURKEY

Aziz Cumhur Kocalar *[1]

[1] Niğde Ömer Halisdemir University, Architecture Faculty, City and Regional Planning, Niğde, Turkey
ORCID ID 0000 – 0003 – 0580 – 9530
azizcumhurkocalar@gmail.com

* Corresponding Author

Received: 28/10/2019 Accepted: 06/01/2020

ABSTRACT

LATMOS (mountain range), which can be a geopark, is located near Lake Bafa Nature Park on the border of Aydın and Muğla. The region has a deep history dating back to many years and valuable natural, archaeological and geological heritage sites. In this study, the geomorphological structure of the region is examined in general terms, especially research area in terms of geotourism has quite interesting features. The elevations at the end point of the Büyük Menderes Basin reach up to pretty high for sub-Aegean geological formations and have an geostrategically important position and wide viewing area. In history, these mountains, which were considered sacred especially in the Carian period, have always been in an important position in terms of human culture. The presence of traces of rock settlements dating to the Neolithic period in the mountains is also known today. Scattered rock paintings in the region were the most important findings. However, they have survived to the present day by being damaged. These and similar rock churches and monaster, as well as military castles and walls, leaving many distinctive and interesting cultural traces, these mountainous areas, which are inhabited, are expected to be constantly preserved and renewed. In history, there are also other ruins of the Carian State, which spread to a much larger background in the sub-Aegean. The port city of Herakleia (now Kapıkırı village) is located on the shores of Lake Bafa. Massive rock formations that have undergone metamorphic changes in the process are in need of investigation in many aspects of volcanic, magnetic and mineralogical aspects. These rocks also have qualities that can be salty due to their relationship with the sea. In summary, this region is composed of mountain ranges (Latmos Mountains), valleys with different features of archelogical sites and a very special lake that have an important natural park feature. In addition to its interesting natural structure, rock formations and geoheritage areas, it must be protected with the awareness of geotourism. It should not be forgotten that in order to transfer the traces of many different cultural settlements within the rocks to the next generations in a healthy way, the region is obliged to be carefully conserved together with a conservation aimmed development plan.

Keywords: *Geopark of Latmos, Urban Geology, Geoheritage-Geotourism-Geosite, Urban Geography, Cultural Heritage Conservation, City and Regional Planning.*

1. INTRODUCTION

The aim of this study was to explore the rural development planning approaches towards geotourism potential in Turkey. The structure of geotourism makes a discussion for the possible effects on the processes of Turkey's rural development. Also, theorical approaches are cited in the inter-disciplinary areas (tourism, public management, planning, art history, etc.) about subject.

2. TOURISM FOR RURAL DEVELOPMENT

The starting point of sustainability objectives in ecological approaches are increasing with interest in the development of interdisciplinary researches of alternative-tourism related subjects. Tourism alternatives for rural economy and/or rural development can research with different dimensions. Rural legislation is also covered here.

2.1. Alternative Tourism

One of them is eco-tourism for rural development, especially cittaslow movement is interesting with festivals. Geotourism also another alternative for rural economy and/or rural development.

2.1.1. Eco-tourism and Cittaslow

Eco-tourism trends are accelerating in the world. Turkey can be created in rural development with Eco-tourism opportunities. But building pressure in rural sites with new generations also critical reason, new generations need jobs. If they are not be able to job, are migrate to big cities.

Cittaslow movement, pioneered by settlements such as Seferihisar-Izmir, draws attention to domestic products and has various potentials for eco-tourism and rural development (Bostancı, 2017).

The slow city movement started in Italy on the Mediterranean coast was accepted in our country, but the practices were left superficial. In Turkey, those ten cities are slow city at below:

Seferihisar (İzmir), Akyaka (Muğla), Gökçeada (Çanakkale), Taraklı (Sakarya), Yenipazar (Aydın), Yalvaç (Isparta), Vize (Kırklareli), Halfeti (Şanlıurfa), Perşembe (Ordu), Şavşat (Artvin).

"Developing a 'One Village-One Product (OVOP)' in Model for the Rural Economy Diversification and Intensification Program in the Final Report of the Eastern Black Sea Regional Development Plan (DOKAP) prepared by the Japanese International Cooperation Agency (JICA) in 2000 was proposed in order to have various fruits and increase the production in general by the Harşit Stream" (JICA, 2000; Yücer, 2016).

Turkey also partially initiated at the local OVOP Project as Table 1 at below . The Governorship Special Administrative Directorates and the Provincial Directorate of Agriculture were supporting with the institutions of these OVOP projects.

Table 1. Some sample villages and products for Cityslow OVOP practice in Turkey. (Yücer, 2016).

Year	City	Place	Products
2002	Giresun	Espiye/ İbrahimşeyh	mandarin and fruit growing.
2003	Tokat	Villages	sour cherry, walnut, peach, vegetables.
2007	Hakkari	Villages	walnut, vegetables, rugs.
2007	Kütahya	Simav Villages	fruit and vegetables

Eel can become a gastronomically important product for Bafa Lake region. It is a fish that has adapted to the salinity of the lake containing salty rocks so it is very clever and much more researched. Region is very interesting in different aspects. Bafa Lake Natural Park and Latmos Mountains has very potential area (Fig. 1).

Fig. 1. Bafa Lake Natural Park from Latmos Mountains.

There can be also different projects, for ex. a project news about ecology (Ertuğrul, 2015). Sub-Aegean region in where Büyük Menderes River is dominant, is very powerful area in history. The view of the mountains of Herakleia Latmos was presented in 1765 with Lake Bafa in front of it (Fig. 7). Special rural areas like Latmos Geopark and Bafa Lake that characterized with geotourism (geosite, geomorphocyte, geopark, geotope), are conserved with current conditions (Fig. *1*, 2, 3, 4, 8, *9*, 10, 11, 1*2*).

2.1.2. Geo-parks and Geo-tourism

A UNESCO definition of global geopark is a unified area with a geological heritage of international significance (UNESCO, 2015). Geoparks use that heritage to promote awareness of key issues facing society in the context of our dynamic planet. There are many geoparks in all over the world (Fig. 2).

Fig. 2. UNESCO Geoparks.

They promote awareness of geological hazards, including volcanoes, earthquakes and tsunamis and many help prepare disaster mitigation strategies with local communities.

Geoparks embody records of past climate changes and are indicators of current climate changes. They are demonstrating a "best practise" approach to using renewable energy and employing the best standards of "green tourism".

Tourism industry promotion in geoparks, as a geographically sustainable and applicable tourism model. They aims to sustain, and even enhance, the geographical character of a place.

Geoparks also inform about the sustainable use and need for natural resources, while at the same time they are promoting respect for the environment and the integrity of the landscape.

The Global Geoparks Network (GGN) is a UNESCO activity established in 1998. According to UNESCO, for a geopark to apply to be included in the GGN, it needs to:

- have a management plan designed to foster socio-economic development that is sustainable based on geotourism
- demonstrate methods for conserving and enhancing geological heritage and provide means for teaching geoscientific disciplines and broader environmental issues
- have joint proposals submitted by public authorities, local communities and private interests acting together, which demonstrate the best practices with respect to Earth heritage conservation and its integration into sustainable development strategies.

Geotourism adds to ecotourism's principal focus on plants (flora) and animals (fauna) by adding a third dimension of the abiotic environment. Thus it is growing around the world through the growth of geoparks as well as independently in many natural and urban areas where tourism's focus in on the geological environment.

The initiatives of the local and/or central authorities have just stayed for tourism and the adoption of sustainability of stakeholders that owners of alternatives tourism ideas not yet been achieved in geotourism.

Most of the world defines geotourism as purely the study of geological and geomorphological features. So geotourism can also be supported by international funding but need to coordination with national authorities again (Fig. 3).

Photographers, climbers, mountain hiking and art groups, nature travelers are interested in the region. Tours, workshops and festivals can be organized in this area. Especially, Spring and Autumn periods are suitable for these kind of activities.

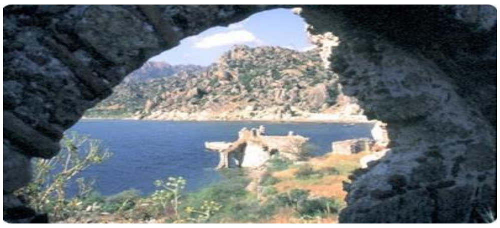

Fig. 3. Latmos Geopark and Bafa Lake views.

2.2. Legislation

Legislation changed in last years for village management subjects. There are some critical points for the future in rural lands. This legislation is also covered below:

"Current discussion in rural development: in 2012, arrangements made with the Law No. 6360, expanding the municipal boundaries of cities in 30 provinces (these are metropolitan municipalities), changes the statue of villages to neighborhoods" (Albayrak; Eryılmaz, 2018).

The characteristics of rural settlements in the metropolitan areas are affected with these changed. These rural areas must be protected in the future.

3. HISTORICAL-NATURAL-CULTURAL STRUCTURE AND ALSO GEOLOGICAL AREAS-"LATMOS GEOPARK"

Recommended as "Latmos Geopark", the region on the shores of Bafa Lake Nature Park on the border of Aydın and Muğla is interesting with its geological history dating back 500 million years.

The geomorphological structure of the region, which has been studied in the mountainous areas and valleys, has quite different features especially in terms of geo-tourism like figures (Fig. 3, 4, 5).

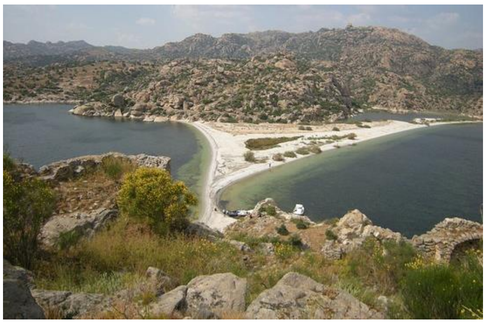

Fig. 4. Latmos Geopark and Bafa Lake connections.

Massive masses undergoing metamorphic changes in the process are expected to be investigated from a mineralogical and petrographical point of view.

Located in the Büyük Menderes Basin, Latmos Mountain (wheel shaped at the top of it) is dominated by a wide range of elevations with elevations reaching 1375 meters. It is understood from the historical structures of the Karia king, which is unearthed as well as the fortress and city walls where the mountains are geostrategically important in history.

3.1. The fortress city of Herakleia-Latmos Antique Harbour City (Kapıkırı Village) and Urban Geology

The fortress city of Herakleia (Kapıkırı village), which is the dominant city and the coast and sea as an end port city on the borders of the Aegean Sea, has been on the shore of the lake today.

This region, which is located on the Aegean Sea borders of Caria State, which has been spread to a wide background in the lower Aegean, is an end port city. In the ancient period, the port city of Herakleia (Kapıkırı village) is a fortress-type city which is dominated by the shore and the sea (Fig. 4, 5, 7, 8, 9). Today, the city is on the shore of the lake.

The region has many different values in terms of educational tourism. These values are at below:

Historical, cultural, artistic, art history, sociology, psychology, coastline changing, global warming, climate changing, natural history, flora-fauna and biodiversity (birds, fishes) etc.

Fig. 5. Herakleia findings (Kapıkırı village).

The cultivated areas like as Kapıkırı, transforming year by year for residences and/or summer houses (Fig. 7, 10), etc. against the rural development with conservation. (Kocalar, 2018a).

3.2. Traces of Rock Settlements and Rock Paintings (Art History)

In addition, traces of rock settlements dating to the Neolithic period were also found at different points of the area and the pictures scattered in the region were the most important findings. However, they have been damaged by external influences and vandalism.

It should not be forgotten that the skirts of the mountainous area where the ancient city and the scattered rock paintings are located, must be carefully protected together with the conservation aimed development plan.

It is of great importance that the lake is prevented from pollution. On the large scale it is necessary to complete the Büyük Menderes Basin Plan, and that it provides a unity with the conservation aimed development plan. Lastly, a holistic protection consciousness should be created in the area.

The rock paintings discovered in the Latmos Mountains in recent years are one of the most important discoveries concerning the prehistoric archeology of Anatolia. These paintings shed light on the thought world of prehistoric societies which have been settled by virtue of their unique depiction language and their repertoire.

Unlike the glacial cave paintings of Western Europe, which consist of magnificent animal depictions, human beings are in the foreground in Latmos rock paintings (Fig. 6) and they are depicted as a part of a community. The transition to the settled order and the change in its forms appear in rock painting art with these examples for the first time (Peschlow-Bindokat, 2006). (Archeology Art History, 2011).

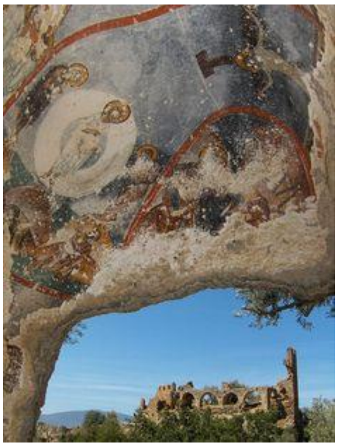

Fig 6. Rock Paintings

In a thesis, "Determination of Mineralogical and Petrographical Properties of Tafonization Processes in Latmos-Beşparmak Mountains (Muğla)". They tried to elaborate the tafoni processes and formation mechanisms in rocks (Söyler, 2020). This work is related paintings, because one of the aims of the thesis is to study rock groups in which pictures are made.

3.3. Natural Park Features

The Natural Park is suitable for use with its status and area management, while preserving its natural thresholds (Kocalar, 2018b). Fishing is important for village people. Flora and fauna are very rich for biodiversity around the lake. In order to be able to convey the traces of many different cultural settlements within the rocks to the next generations in a healthy way, the priority should be given to the evaluation of the region for purposes of natural history education and through alternative tourism functions.

Area; Because of its natural structure, rock formations and geo-heritage areas, it must be protected within the framework of geo-tourism awareness. Bafa Lake is a historical lake (Fig. 7).

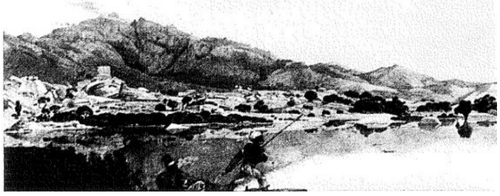

Fig. 7. The view of the mountains of Herakleia-Latmos (1765) with Lake Bafa (Peschlow-Bindokat, 2005, pp. 41). (Distelrath, 2008, pp. 2).

3.4. Conservation Aimmed Plan

In 1989, the whole city structure of Herakleia was protected by official authorities. However, a current assessment of the monuments (Fig. D) could not be made. However, only a usage and conservation plan can be prepared on the basis of this evaluation (Distelrath, 2008, pp.105-112). Coastline of ancient period was very different and village was a coastline city in past (Fig. 8).

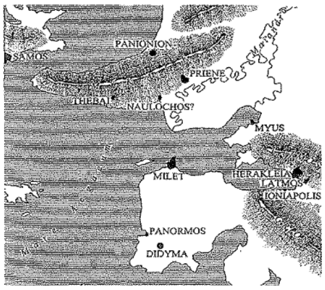

Fig. 8. Coastline of ancient period and relationship of the lake with the sea (Abb.9) (Distelrath, 2008, pp. 13).

The relationship of the lake with the sea is still strong. The traces of the past connection with the Aegean Sea over the Gulf of Latmos are better understood when looking from the mountains towards the sea (Fig. 9).

Fig. 9. Coastline of ancient period and relationship of the lake with the sea.

The village development plan should be explored in detail as in the source (Fig. 10) (Distelrath, 2008, pp.112-119) after Conservation Aimmed Plan.

Fig. 10. Herakleia (Kapıkırı Village) (Abb.70) (Distelrath, 2008, 115).

Regulatory proposals for old and new buildings should be brought (Peschlow-Bindokat, 2006, pp.119-125). New development trends of the village should be thoroughly evaluated (Peschlow-Bindokat, 2006, pp.125-132).

The development phases of the village in the previous years (2005) should be taken into consideration as in the source (Distelrath, 2008, pp.153-165). Rural life in village with Latmos and Bafa Lake should be conserved in future.

The land use plan of the village and the protected areas were documented (Fig. 11) (Distelrath, 2008, pp.165-166).

With the silhouette of Herakleia city (Fig. 7, 10, 12), visual inventory of the works in today's village areas should be completed and intermittent monitoring should be made.

3D models should be made using terrestrial laser scanners as done in the mausoleum (Alptekin, Çelik, Yakar, 2019).

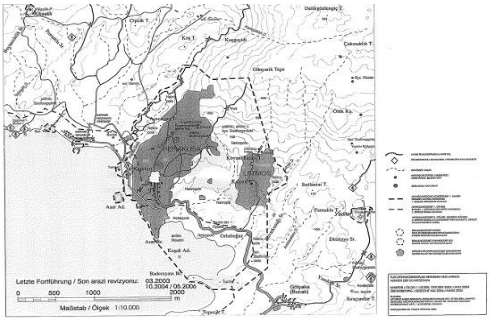

Fig. 11. General Plan - Land use plan of the village and documentation of the protected areas (Abb.A25) (Distelrath, 2008, pp.165).

This site workings after Distelrath, published a book, named “Latmos, Miras 1, Heritage in Context”, the project supported by Deutsches Archäologisches Institut Istanbul, (Bachmann, Maner, Tezer, and Göçmen, 2011).

3.5. Geotourism Potential in Geoheritage Areas in Latmos Mountains

These mountainous geological-archaeological sites, which have witnessed permanent settlements with their rock churches and monasteries as well as their military and commercial structures and with many distinct and interesting cultural traces, should be carefully preserved and renewed in tourism. Latmos Mountains are very near Lake at below (Fig. 12).

Fig. 12. Latmos Mountains and Bafa Lake.

The Latmos Mountains and Bafa Lake are a whole. The surrounding quarries are an important danger for this geopark. Also lake pollution of the lake is another important danger every summer. Fish farm and olive oil processing factories should be taken under control.

Geosite: The rock-mineral-fossil assemblage which shows an event, sequence, geological structure, texture type, formation or evolution during the formation or evolution of the earth's crust, is a scientific document a natural entity with the visual beauty in some cases. (Wimbledon, 1996) (ProGEO Group, 1998; www.progeo.se).

Geological heritage: It is a rare geosite under threat of extinction that will destroy the information and geological document of the region in case it is destroyed (Wimbledon, 1996; Kazancı, 2010).

4. CONCLUSION

Geo-tourism is important for this site research in the rural development of Turkey. Geological values discussed with other values in the selected site where is Latmos Mountains in the near of Bafa Lake.

Latmos Mountains and walleys are also very special natural area as geological and other cumulative characteristics in historical, archelogical, cultural, architectural, natural, sport, and educational. So geotourism will bring awareness for village people in the region with opportunities values to support for rural life.

The main feature of this kind of study is to develop a marked area from the original values of special geological and natural also rural areas. Also, to determine the deterioration of the characteristics of these areas.

The most critical issue for Turkey is the villages which turned into neighborhoods by the new metropolitan law. These kinds of special lands must be protected and also can’t be converted into second homes.

The cultivated areas like as Herakleia-Latmos (Kapıkırı village), transforming year by year for residences and/or summer houses, etc. against the rural development with conservation.

Latmos surrounding quarries can’t acceptable for this geopark, they can’t work near this area. They are affecting ground and upper ground structure. Also rock paintings and rock churches can be damaged.

Lake pollution, fish farm and olive oil processing factories are other important dangers, they should be taken under control and no new licenses should be issued.

Additional researches should increase the database and methodological approaches to develop the theoretical and practical bases at the national level in geological sites. Local efforts should be given priority in the design and implementation of initiatives in the world for these types of sites.

After Kula (Manisa), Latmos mountains will be an important geopark area, reflecting the character of the Lower Aegean Region. Latmos mountains are proposed to join to the European Geoparks Network in this paper.

ACKNOWLEDGEMENTS

Thanks for project partners that’s named “Lake Bafa Nature Park, Caria City State - Harbour City (Herakleia-Latmos) (Kapıkırı Village) and the Geopark Character of the Latmos Mountains, the Great Menderes River Basin Protection Project” (2010-2018).

This paper was presented with first draft of it with Geopark concept in the CISET 2019. Also thanks for this organization.

Kocalar, A. C. (2019). Herakleia Karia Ancient Port City with Geoheritage Areas and Urban Geology-Latmos Geopark (Beşparmak Mountains), CISET - 2nd Cilicia International Symposium on Engineering and Technology, Proceedings Book, 10-12 October, 2019, (CISET 2019), Mersin Üniversitesi. Mersin / TURKEY. https://azizcumhurkocalar.blogspot.com/2019/10/bildiri40-herakleia-karia-ancient-port.html

This paper was also related with 2018 draft of it with historical conservation concept:

Kocalar, A. C. (2018). Conservation Issues: Karia State Antique Harbor City "Herakleia-Latmos" and "Bafa Lake Natural Park", II. International Urban, Environment and Health Congress, Abstract Book and Proceedings Book, 18-20.04.2018 Cappadoccia, Ürgüp, Nevşehir, Türkiye. p. 539, pp. 117-132. https://azizcumhurkocalar.blogspot.com.tr/2018/04/koruma-sorunlar-karia-devleti-antik.html

This paper was related and presented with 2014 draft of it with regional conservation concept, too:

Kocalar, A. C. (2014). Büyük Menderes Havzası, Bafa Gölü ve Çevresine Yönelik Çevresel Risklerin Analizi ve Mekansal Etkilerinin Değerlendirilmesi”, ISEM 2014 2nd International Symposium on Environment and Morality, Proceedings Book, 24-26 Oct 2014, pp: 1173-1187, Adıyaman University, Adıyaman – Turkey. https://azizcumhurkocalar.blogspot.com/2014/07/cevre-koruma-kuramlarna-aykr-gerceklik.html

REFERENCES

2012 dated and Law No. 6360, *Legal Arrangements*.

Albayrak, A. N., Eryılmaz, Y. (2018). “From Rural to Urban: Transformation of Villages at the Border of Metropolitan Cities”, *CAUMME 2018: Conference of Architecture and Urbanism in the Mediterranean and the Middle East Proceedings*. Ed., Girginkaya Akdağ, S.; Soygeniş, S.; Vatan, M., Bahçeşehir University, İstanbul.

Alptekin, A., Çelik, M., Yakar, M. (2019). Anıtmezarın Yersel Lazer Tarayıcı Kullanarak 3B Modellenmesi. *Türkiye Lidar Dergisi*, 1 (1) , 1-4 . Retrieved from https://dergipark.org.tr/tr/pub/melid/issue/50713/641560

Archeology Art History, (2011). Retrieved from https://www.arkeolojisanat.com/shop/kategori/kitap/sanat-tarihi_16_71.html [Accessed 27 Nov 2019].

Bostancı, S. H. (2017). *Sustainable Urban Model Approaches of Local Governments in Turkey*. Management & Education/Upravlenie i Obrazovanie, 13.

Bachmann, M., Maner, Ç., Tezer S., and Göçmen, D., (2011). *“Latmos, Miras 1, Heritage in Context – Konservierung und Site Management im natürlichen, urbanen und sozialen Raum”*, Istanbul.

Distelrath, A. (2008). Miras 1, *Siedeln und Wohnen in einer Ruinenstatte. Ein denkmalpflegerisches Konzept für Herakleia am Latmos. / Yerleşim ve Yaşam Alanı Olarak Ören Yeri. Herakleia (Latmos) için bir Koruma Konsepti,* Ein denkmalpflegerisches Projekt für Herakleia am Latmos, Miras 1 (Istanbul 2011), Deutschen Archäologischen Instituts, Technische Universitat, Dissertation, Berlin, Ege Yayıncılık, İstanbul.

Deutsches Archäologisches Institut Istanbul, Retrieved from https://tuerkei.diplo.de/tr-tr/themen/kultur/-/1797670 [Accessed 27 Nov 2019].

Ertuğrul, E. (2015). Bafa Gölü ve Çevresi İçin Ekoturizm Projesi, Arkeofili, Retrieved from https://arkeofili.com/bafa-golu-ve-cevresi-icin-ekoturizm-projesi/

JICA, Japonya Uluslararası İşbirliği Ajansı, (2000). Doğu Karadeniz Bölgesel Gelişme Planı Nihai Raporu, TC Başbakanlık Devlet Planlama Teşkilatı Yayını, Ankara.

Kazancı, N., Şaroğlu, F., Suludere, Y. (2015). Jeolojik Miras ve Türkiye Jeositleri Çatı Listesi. Maden Tetkik ve Arama Dergisi, s.264.

Kocalar, A. C. (2018a). Historical Environment Conservation Issues: (Karia Period) "Herakleia-Latmos", *International Journal of Social Humanities Sciences Research (JSHSR)*, (JSHSR.com), 2018 Vol: 5 / Issue: 19 pp.654-662. Retrieved from http://dx.doi.org/10.26450/jshsr.402

Kocalar, A. C. (2018b). Archaeological-Natural-Geological-Historical-Cultural Environment (Rivers-Basins-Lakes) Conservation Issues and Solution Proposals: "Bafa Lake Natural Park", *Mimarlık, Planlama ve Tasarım Alanında Yenilikçi Yaklaşımlar*.

L.G. Kaya, Ş.A. Dönmez, N. Abbasov Ed. Gece Kitaplığı Yayınevi, ISBN 978-605-288-796-7, 15. Chapter, pp: 215-248. Retrieved from http://dx.doi.org/10.26449/sssj.549

Peschlow-Bindokat, A. (2005). *Herakleia am Latmos – Stadt und Umgebung*, İstanbul.

Peschlow-Bindokat, A. (2006). *Tarihöncesi İnsan Resimleri. Latmos Dağları'ndaki Prehistorik Kaya Resimleri,* (Çev. Işıl Işıklıkaya), Sadberk Hanım Müzesi Yayınları, ISBN: 9799756959168, 2006, İstanbul.

ProGeo Group. (1998). A first attempt at a geosites framework for European lUGS initiative to support recognition of World heritage and European geodiversity. *Geologica Balcanica* 28, 5-32.

Söyler, M. (2020). *"Determination of Mineralogical and Petrographical Properties of Tafonization Processes in Latmos-Beşparmak Mountains (Muğla)"* Ongoing Master Thesis, Department of Geological Engineering / Department of Mineralogy and Petrography, Institute of Natural and Applied Sciences, Hacettepe University, Ankara.

UNESCO, (2015). *"What is a Global Geopark?"*, United Nations Educational, Scientific and Cultural Organization**.** [Retrieved 16 Aug 2015].

Wimbledon, W.A.P. (1996). National site election, a stop on the road to a European Geosite List, *Geologica Balcanica* 26, 15-27.

Wikipedia,
https://en.wikipedia.org/wiki/Geopark#cite_note-globalgeopark-2

Yücer, A. A. (2016). "Kırsal Kalkınma için Bir Köy Bir Ürün Projeleri ve Başarı Koşulları", *XII. Ulusal Tarım Ekonomisi Kongresi,* https://www.nationmaster.com/country-info/stats/Agriculture [Accessed 26 Sept 2019].

Turkish Journal of Engineering

Turkish Journal of Engineering (TUJE)
Vol. 4, Issue 4, pp. 183-196, October 2020
ISSN 2587-1366, Turkey
DOI: 10.31127/tuje.639378
Research Article

AN EXTENDED ANALYSIS OF THE MODELS TO ESTIMATE PHOTOVOLTAIC MODULE TEMPERATURE

Talat Ozden *[1,2], Doga Tolgay [3,4], M. Samet Yakut [4] and Bulent G. Akinoglu [3,4,5]

[1] Gumushane University, Department of Energy Systems Engineering, Gumushane, Turkey
[2] METU, The Center for Solar Energy Research and Applications (GUNAM), Ankara, Turkey
ORCID ID 0000 – 0002 – 0781 – 2904
tozden@gumushane.edu.tr

[3] METU, Department of Physics, Ankara, Turkey
[4] METU, Department of Electrical and Electronics Engineering, Ankara, Turkey
ORCID ID 0000 – 0002 – 3155 - 946X
doga.tolgay@metu.edu.tr

[4] METU, Department of Electrical and Electronics Engineering, Ankara, Turkey
ORCID ID 0000 – 0002 – 3236 – 5843
samet.yakut@metu.edu.tr

[3] METU, Department of Physics, Ankara, Turkey
[4] METU, Department of Electrical and Electronics Engineering, Ankara, Turkey
[5] METU, Earth System Science Program, Ankara, Turkey
ORCID ID 0000 – 0003 – 1987 – 6937
bulo@metu.edu.tr

* Corresponding Author

Received: 29/10/2019 Accepted: 07/01/2020

ABSTRACT

To estimate the performance of the photovoltaic power systems is the key issue in their techno-economic feasibility analysis. Performances, on the other hand, strongly depends on the module temperatures of the photovoltaic systems. In this study, we evaluated the performance of ten different module temperature estimation models using the measured outdoor data of five different modules. The modules are installed at the rooftop of a building located at Central Anatolia where the climate is cold and semi-arid. The results showed that the models having smaller number of parameters perform better than the others. We concluded that such analysis should be carried out at different ambient conditions so that the best performing models for the site can be obtained. Another outcome of the study is that the seasonal evaluation of the performance of the models should be carried out.

Keywords: *Photovoltaic Module, Module Temperature, Module Temperature Variation, Module Temperature Estimation*

1. INTRODUCTION

The interest in renewable energy resources is growing due to the environmental damages of fossil fuels. So nowadays, many power plants that use renewable energy resources such as hydro, wind and solar, etc. have been installed worldwide in the last decades. Especially, solar power plants installments are rapidly growing all over the world. Reports published by International Renewable Energy Agency (IRENA, 2019) and International Energy Agency (IEA, 2019) in 2019 show that total installed photovoltaic (PV) capacity reaches nearly 500 GWp. Also, the same report (IRENA, 2019) shows that the PV capacity in Turkey reaches 5 GWp during just the last three years. According to another report, including some scenarios (SolarPowerEurope 2018), this installation trend will continue at the same rate till 2022. For example, installation PV capacity in the world will be 1.2 TWp as regards to high scenarios or will be 813 GWp as regards to low scenarios.

While the installation of solar power plants increasing with a large rate, the R&D on the subject matter interestingly also heavily keeps going. In this respect, the performance of the solar modules particularly depends on the module temperature and thus, it becomes important to estimate the module temperature for short- and long-term feasibility analyzes. There exist in the literature many correlations connecting the module temperature to climatic parameters and datasheet specifications of the modules.

It is obvious that a considerable amount of solar energy absorbed by solar panels is converted into heat within the cell. Then, the temperature of the PV modules increases due to heat. Researchers conducted several studies to see how the temperature affects the efficiency of the modules. According to Dubey *et al*, efficiency is linearly decreasing with operating temperature (cell or module temperature) (Dubey, Sarvaiya, and Seshadri, 2013). A research conducted on this issue by Rahman *et al*. illustrated that each 1°C increase in cell temperature causes a 0.06% decrease in electrical efficiency of the PV module under solar irradiance of 1000 W/m^2 (Rahman, Hasanuzzaman, and Rahim, 2015). Another research which was conducted by Amr *et al.* shows that the temperature of the modules can be decreased using heat sink fins thermally attached to the back surface of the modules (Amr *et al*., 2019). They calculated the module temperature using a thermal modeling approach and conducted experiments to compare their results.

The efficiencies of solar cells are measured at standard test conditions where cell temperature is 25 °C and irradiance 1000 W/m^2. However, solar cells are rarely meet this standart efficiency value at outdoor conditions, because on a clear summer day the temperature of PV panels can reach up to 60 °C (Ozden, Tolgay, and Akinoglu, 2018). Therefore, to forecast the yield before solar power plant installation, it is also necessary to estimate the module temperature. There exist many temperature estimation correlations from various authors in the literature (Duffie and Beckman, 2013; Eckstein, 1990; Faiman, 2008; King, Boyson, and Kratochvil, 2004; Koehl *et al*., 2011; Kurtz *et al*., 2009; Mattei *et al*., 2006; Roberts, Zevallos, and Cassula, 2017; Santhakumari and Sagar, 2019).

Skoplaki *et al*. indicated that free convection loss is insignificant when compared to wind convection loss for wind speed 1-15 m/s. They obtained that the average deviation between measured and estimated Tc values is less than 3 °C in the range 1–15 m/s (Skoplaki, Boudouvis, and Palyvos, 2008).

Mattei *et al*. used two different temperature equations and found that after 10 m/s wind speed effect becomes less important in terms of yield per meter square (Mattei *et al*., 2006). Eckstein estimated the module temperature in his thesis by using a loss temperature coefficient (Eckstein, 1990). M. Akhsassi *et al*. developed two temperature equations, one can be used with wind speed data and the other can be used without wind data. They have used 32 monocrystalline silicon panels and calculated overall lost coefficients for the panels. Moreover, they have analyzed different types of thermal models. In their analysis, they have found that Sandia and Faiman temperature model overestimates the PV module temperature when irradiance is high and underestimates the module temperature when irradiance is low whereas Lasnier thermal model underestimates module temperature when irradiance is high and overestimates when irradiance is low (Akhsassi *et al*., 2018). Gökmen *et al*. investigated two different thermal models; one of them considers the cooling effect of wind whereas the other one does not consider. The authors estimated yearly energy values using predicted module temperature from these models and measured module temperature from a PV system, including Poly-Si modules at the windy location Aalborg, Denmark. The study presented that formula (does not consider the wind speed data) underestimates the yearly energy by 3.5% since it overestimates the module temperature (Gökmen *et al*., 2016).

Dierauf *et al*. have developed a formula differing from traditional ones. Their new thermal model estimates the temperature by considering the effects of the ambient temperature and wind (Dierauf *et al*. 2013). Another temperature formula developed by Ding *et al*. calculates the cell temperature with the help of the back surface temperature of the modules (Ding *et al*. 2014). Lo Brano *et al*. acquired a formula that is sensitive to irradiance and temperature changes by calculating K factor which is thermal correction factor (Lo Brano and Ciulla 2013). Skoplaki and Palyvos analyzed 22 different temperature models and came up with the fact that use of these models should be handled with care as they are developed for specific mounting geometry or building integration level (Skoplaki and Palyvos 2009). Schwingshackl *et al*. worked on four different temperature models of standard approach namely Skoplaki's, Koehl's, Mattei's and Kurt's models. They found out that models which include wind cooling effects can be used for better estimations (Schwingshackl *et al*. 2013).

This study gives the analysis of measured data of module temperatures for five modules tested in outdoor conditions of a cold semi-arid climate of Ankara. The modules are tested for three years. Ten models from the literature are chosen for a comparative study to reach the best-performing ones to be used in techno-economic analysis.

The next section gives the materials and methods used in work together with a description of the site, climate, data, and the models. Section three gives the results of the analysis, and the statistical errors are tabulated and discussed. The last section is concluding remarks with some future prospects.

2. MATERIALS AND METHOD

2.1. Description of Sites and Modules

Measurements are taken on the rooftop of METU, Department of Physics building in Ankara, Turkey which was located in the Central Anatolia. According to Köppen - Geiger Climate Classification, Ankara has a cold semi-arid climate (Peel, Finlayson, and McMahon, 2007; Rubel *et al*., 2017).

The technical details of test sites are presented in Table 1. They are in operation for three years between April 2016 to April 2019. The average ambient temperature in this time interval is 13.8 °C. The highest temperature is 38.5 °C in July 2017 and the lowest temperature is –8.9 °C in February 2017 during the test period. And also, annual average relative humidity (RH) and wind speed is about 60 % and about 1 m/s, respectively.

Table 1. Test site details

Parameter	GUNAM-Ankara, Turkey
Latitude (°N)	39.9
Longitude (°E)	32.8
Elevation (m)	929
Tilt & Azimuth angle (°)	32 & 0

Five different types of PV modules are investigated in this study. Modules are mounted on an aluminum construction and they are not close to each other. Two of the tested PV modules which are microcrystalline based amorphous silicon (μc-Si/a-Si) and Cupper Indium Selenide (CIS) are thin film. The other three PV modules have crystalline silicon structures which are Monocrystalline Silicon (Mono-Si), Polycrystalline Silicon (Poly-Si) and Heterojunction with Intrinsic Thin layer (HIT). They are cleaned weekly.

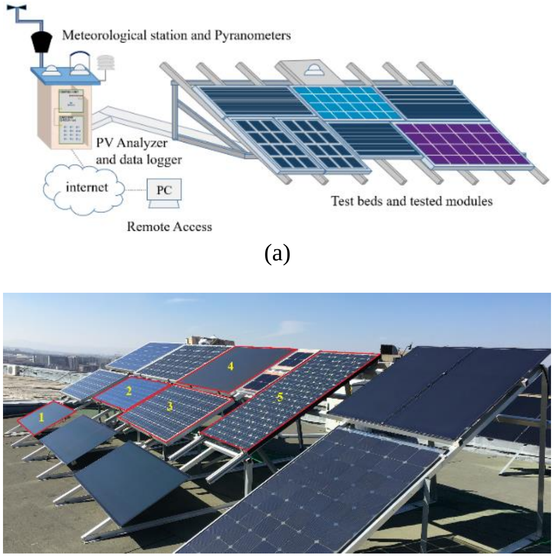

(a)

(b)

Fig. 1. Configuration of METU-GUNAM Outdoor Test Facility (a) and tested modules - 1: CIS, 2: Poly-Si, 3: Mono-Si, 4: μc-Si / a-Si, 5: HIT (b)

The elements of our testing system can be seen in Fig. 1 and the specifications of five tested modules used in the present study are tabulated in Table 2.

Table 2. Tested PV Modules Specifications

Module Types	P_{MAX} [W]	V_{OC} [V]	I_{SC} [A]	V_{MPP} [V]	I_{MPP} [A]	η [%]	β_{STC} [%/°C]	$T_{m,NOCT}$ [°C]	Area [m2]
CIS	130.0	59.50	3.28	44.90	2.90	12.3	-0.39	40	1.05
Mono-Si	160.0	43.70	5.06	35.30	4.58	12.5	--**	--**	1.28
Poly-Si	130.0	21.70	8.18	17.80	7.30	12.7	-0.45*	46	1.02
μc-Si / a-Si	128.0	59.80	3.45	45.40	2.82	9.1	-0.24	44	1.40
HIT	230.0	42.30	7.22	34.30	6.71	16.5	-0.30	45	1.39

* The parameter unit is %/K. ** There is no datasheet for this module. Therefore, some results are missing.

2.2. Receiving Data from the Test Setup

All of the modules are connected to a PV analyzer which measures the electrical performance, solar radiation, and module and ambient temperatures. The average measurement results of these parameters are taken in every 10 minutes and are saved inside a daily file to the internal memory of the analyzer. Solar irradiation is measured by using a Kipp&Zonnen high precision secondary standard pyranometer, and temperatures data are measured by using T type thermocouples. The thermocouples which are used for measurement of cell temperatures are firmly adhered to at the back of each module. These temperature sensors are attached to the middle of the modules (Fig. 2). However, as the junction box of the μc-Si / a-Si module is located at the center of the module backside, the thermocouple of this module is adhered to near its junction box (Ozden, Tolgay, and Akinoglu, 2018)

Climatic parameters are measured with a meteorological station. The station can measure ambient temperature, RH, precipitation, solar irradiance, wind speed, and direction every 10 minutes time interval. The station is fixed to 2 meters above from the floor level of the rooftop.

Fig. 2. One of the temperature sensors adhered to the backside of a module

The module temperatures reach about 70 °C under around 1000 W/m^2 of irradiance and at elevated ambient temperature except for the μc-Si / a-Si thin-film module. The corresponding values for the μc-Si / a-Si stay somewhat at 60 °C at the same conditions.

2.3. Approaches Used in PV Temperature Estimation

In the study, ten correlations presented in the literature are used to estimate the module/cell temperature from ambient temperatures and some other parameters (see Table 3). These equations are mainly tested and suggested to estimate the module/cell temperature in literature. Besides, some software packages for performance analysis of PV systems also use some of these equations (Homer Pro 3.13 help documentation, 2019; PVsyst 6 help documentation, 2019). To estimate the module temperature, Homer Pro uses Eq. 5 and PVsyst uses Eq. 1 in Table 3.

Presented equations in Table 3 contain many parameters. Some are the same while some differ. The explanation of these parameters is given in the Nomenclature section. However, values of some of these parameters (such as parameters with STC and NOCT indexing) are obtained from the datasheet of modules supplied by the manufacturer. The other parameter values are taken from the references explained in the followings.

Table 3. Several correlations to estimate the cell or module temperature.

Eq. #	Correlation	Ref
1	$T_m = G_t \times e^{(a+bV_w)} + T_a$	(King *et al.*, 2004)
2	$T_c = T_a + \frac{G_t\left(T_{m,NOCT} - T_{a,NOCT}\right)}{G_{NOCT}}$	(Ross and Smokler, 1986)
3	$T_m = T_a + \frac{G_T}{U_0 + U_1 V_w}$	(Faiman, 2008)
4	$T_c = \frac{U_{PV} T_a + G_t(\alpha\tau - \eta_{STC} - \beta_{STC}\eta_{STC}T_{STC})}{U_{PV} - \beta_{STC}\eta_{STC}G_t}$	(Sandnes and Rekstad, 2002)
5	$T_c = T_a + \frac{G_t \alpha\tau}{U_L}\left(1 - \frac{\eta_{STC}}{\alpha\tau}\right)$	(Eckstein, 1990)
6	$T_c = T_a + \frac{G_t(T_{m,NOCT} - T_{a,NOCT})}{G_{NOCT}}\left[1 - \frac{\eta_{STC}}{\alpha\tau}\right]\frac{h_{w,NOCT}}{h_w}$	(Duffie and Beckman, 2013)
7	$T_c = T_a + \frac{G_t(T_{m,NOCT} - T_{a,NOCT})}{G_{NOCT}}\left[1 - \frac{\eta_{STC}\left(1 - \beta_{STC}T_{m,STC}\right)}{\alpha\tau}\right]\frac{h_{w,NOCT}}{h_w}$	(Akhsassi *et al.*, 2018)
8	$T_c = T_a + \omega \times \left(\frac{0.32}{h_w}\right) \times G_t$	(Skoplaki *et al.*, 2008)
9	$T_m = \frac{T_a + \frac{G_t}{G_{NOCT}} \times \left(T_{m,NOCT} - T_{a,NOCT}\right) \times \frac{h_{w,NOCT}}{h_w} \times \left(1 - \frac{\eta_{STC}}{\alpha\tau} \times (1 - \beta_{STC} \times T_{STC})\right)}{1 - \left(\frac{\beta_{STC}\eta_{STC}}{\alpha\tau}\right) \times \left(\frac{G_t}{G_{NOCT}}\right) \times \left(T_{m,NOCT} - T_{a,NOCT}\right) \times \frac{h_{w,NOCT}}{h_w}}$	(Skoplaki *et al.*, 2008)
10	$T_m = \omega_1 \times T_a + \omega_2 \times G_t + \omega_3 \times V_w + c$	(Tamizhmani *et al.*, 2003)

In Eq. (1), a and b constants are taken from reference (King, Boyson, and Kratochvil, 2004). They are taken as –3.47 and –0.0594 for CIS module due to its module structure (glass/cell/glass and open rack) whereas for the other modules they are taken as –3.56 and –0.075 because of their module structure and fixing position (glass/cell/polymer sheet and open rack), respectively. In the same equation, the wind speed V_w was measured at a standard height of 10 m. However, the wind speed was not measured at a height of 10 m in our test site. Therefore, the wind speed value was converted to the appropriate height using the measurement height by the following power law (Twidell and Weir, 2015):

$$\frac{V_w}{V_{w,ref}} = \left(\frac{z}{z_{ref}}\right)^n \tag{13}$$

where z_{ref} is reference height measured from the ground,

z is 10 m and $V_{w,ref}$ is the measured wind speed at the height of the test site. n is the friction coefficient and the coefficient is a function of the topography at the test site (small town with some trees and shrubs). It is taken as 0.3 from (Bañuelos-Ruedas, Angeles-Camacho, and Rios-Marcuello, 2010). In Eq. (3), U_0 and U_1 constants are taken as 23.09 and 3.11 for the CIS module from (Koehl *et al*., 2011) and taken as 25 and 6.84 for the other modules from (Faiman, 2008), respectively. The Eq. (6, 7, 8 and 9) include the heat convection coefficient equations. The correlations to estimate module/cell temperature in the literature use many parameters of climatic conditions and its nameplate parameters (Cole and Sturrock, 1977; Duffie and Beckman, 2013; Kaplani and Kaplanis, 2014; Loveday and Taki, 1996; Nolay, 1987; Sharples and Charlesworth, 1998). Some of them are frequently chosen for more accurate estimation of module/cell temperature and are tabulated in Table 4. The coefficients of Eq. 12, 20, 16 and 16 in Table 4 are used In Eq. 6, 7, 8 and 9 (like $h_w = 5.7 + 3.8V_w$ and $h_{w,NOCT} = 5.7 + 3.8V_{w,NOCT}$), respectively.

Table 4. Various air forced heat convection coefficient equations ($\boldsymbol{h_w}$ $\boldsymbol{and}$ $\boldsymbol{h_{w,NOCT}}$)

	Heat convection coefficients	Eq. #	Ref
1	$\boldsymbol{h_w = 5.67 + 3.86V_w}$	12	(Duffie and Beckman 2013)
2	$\boldsymbol{h_w = 5.82 + 4.07V_w}$	13	(Nolay 1987)
3	$\boldsymbol{h_w = 11.4 + 5.7V_w}$ for the windward condition	14	(Cole and Sturrock 1977)
4	$\boldsymbol{h_w = 5.7}$ for the leeward conditions	15	(Cole and Sturrock 1977)
5	$\boldsymbol{h_w = 8.91 + 2.0V_w}$ for the windward condition	16	(Loveday and Taki 1996)
6	$\boldsymbol{h_w = 4.93 + 1.77V_w}$ for the leeward conditions	17	(Loveday and Taki 1996)
7	$\boldsymbol{h_w = 8.3 + 2.2V_w}$ for the windward condition (angle 0°)	18	(Sharples and Charlesworth 1998)
8	$\boldsymbol{h_w = 7.9 + 2.6V_w}$ for the windward condition (angle 45°)	19	(Sharples and Charlesworth 1998)
9	$\boldsymbol{h_w = 6.5 + 3.3V_w}$ for the windward condition (angle 90°)	20	(Sharples and Charlesworth 1998)
10	$\boldsymbol{h_w = 7.9 + 2.2V_w}$ for the windward condition (angle 135°)	21	(Sharples and Charlesworth 1998)
11	$\boldsymbol{h_w = 8.3 + 1.3V_w}$ for the windward condition (angle 180°)	22	(Sharples and Charlesworth 1998)

U_{PV} is the heat exchange coefficient corresponding to the total surface area of the module, i.e. two times the surface area corresponding to h_w since the heat is lost from the two faces of the PV (lateral surfaces are neglected) (Mattei *et al*., 2006), so if Eq. (12) is used,

$$U_{PV} = 11.34 + 7.72V_w. \tag{23}$$

If Eq. (13) is used,

$$U_{PV} = 11.64 + 8.14V_w. \tag{24}$$

If Eq. (14) and (15) is used,

$$U_{PV} = 17.10 + 5.70V_w. \tag{25}$$

The coefficients of Eq. (23), (24) and (25) are used in Eq. (4) one by one. However, as the best results are obtained by using Eq. (25) together with Eq. (4), just these results are presented in Fig. A4 and in Table 5.

In Eq. (5), U_L is calculated for every module by using Eq. (14) from (Eckstein, 1990).

$$U_L = \frac{G_{NOCT} \times \alpha\tau}{T_{m,NOCT} - T_{a,NOCT}} \tag{14}$$

In addition, in Eq. (4, 5, 6, 7 and 9) $\alpha\tau$ constant are used as 0.9 (Eckstein, 1990; Sandnes and Rekstad, 2002). Another parameter ω in Eq. (8) is taken as 1.0 from (Skoplaki, Boudouvis, and Palyvos, 2008). Though, this equation does not estimate the module temperature when the wind speed equal to zero (Skoplaki, Boudouvis, and Palyvos, 2008). The last parameters in Eq. (10) ω_1, ω_2, ω_3, and c are taken from (Schwingshackl *et al*., 2013) which is presented at a table as average values for every module types.

As the next step to determine and to show which equation has higher accuracy is conducted using two procedures. One of them is that the deviation between estimated and measured values are calculated by using Eq. (26), and these temperature differences are presented as a daily base by using graphics.

$$T_{error} = T_{measured} - T_{estimated} \tag{26}$$

The other method is the use of statistical errors between estimated and measured values evaluated by using mean absolute error (MAE) and root mean squared error (RMSE) methodologies (Eq. (27) and (28)):

$$MAE = \frac{1}{N}\sum_{i=1}^{N}\left|T_{error,i}\right| \tag{27}$$

$$RMSE = \sqrt{\frac{1}{N}\sum_{i=1}^{N}\left(T_{error,i}\right)^2} \tag{28}$$

where N is the total number of data and i is a loop indexing number. The obtained results are tabulated in Table 5.

3. RESULTS AND DISCUSSION

To accurately determine the yield of PV systems is important, and this can only be achieved with the correct prediction of the module temperature. The estimation of module temperature could be made by using implicit and explicit correlations. The implicit correlations generally include thermal and physical properties of the PV cell/module, solar resource, climatic data, and heat convection coefficient because of the wind. The explicit correlation equations for the operating temperature of the PV cell/module are simply associated with the ambient temperature and the solar irradiance. In this study, to evaluate the accuracy of estimations for some of both types of correlation forms from the literature are selected and used. These equations given in Table 3 are particularly preferred from those in which the best results are obtained in the literature. The ten equations to estimate the PV cell/module temperature for the five different module types are compared using the measured data of three years for these module types. The deviations between estimated and measured data are shown in Appendix. Considering all results, the deviation temperatures can be up to +20 and −30 °C. The best results are obtained from Eq. (1) for a-Si / μc-Si, Poly-Si, and HIT modules and Eq. 8 for CIS and Mono-Si modules. These results have the smallest deviations as can be seen in Fig. A1 and A8, and Table 5. On the other hand, the equations giving the highest deviations for the same modules are from Eq. (4) and Eq. (10). These results are also shown in Fig. A4 and A10, and Table 5.

Table 5. Values of the statistical coefficients for various models[1]

# of T_m estimation Eq.		a-Si / μc-Si	CIS	Mono-Si	Poly-Si	HIT
1	MAE	2.7001	2.4712	2.6520	3.0282	2.8054
	RMSE	3.2746	3.1084	3.2597	3.6006	3.3831
2	MAE	3.6931	2.7175	--*	3.9268	3.6153
	RMSE	4.8522	3.4281	--*	4.7377	4.3805
3	MAE	3.9724	3.8277	3.0817	3.7438	3.6682
	RMSE	5.2178	4.9844	3.8253	4.4985	4.4605
4	MAE	4.9210	3.3601	--*	4.3650	3.9545
	RMSE	6.8621	4.4737	--*	5.4310	4.9395
5	MAE	3.1253	3.0747	--*	3.2659	2.9382
	RMSE	3.9926	4.0215	--*	3.9058	3.5223
6	MAE	3.5149	3.2200	--*	3.8415	3.4405
	RMSE	4.8276	4.2467	--*	4.8189	4.3101
7	MAE	3.2977	3.1766	--*	3.3938	3.1979
	RMSE	4.3417	4.1793	--*	4.0938	3.9130
8	MAE	3.5126	2.2913	2.4232	2.9674	2.9275
	RMSE	4.5885	3.0352	3.1016	3.6376	3.5810
9	MAE	3.2429	2.8345	--*	3.4883	2.8625
	RMSE	4.0496	3.6073	--*	4.1526	3.4589
10	MAE	4.8815	4.3371	4.2181	5.8809	--**
	RMSE	5.4806	5.0573	4.9287	6.5913	--**

* There is no datasheet for this module. Therefore, some results are missing.
** There are no coefficients of Eq. (10) for the HIT module. Therefore, the results are missing.
🟥 The best-performing results. 🟫 The lowest-performing results.

The correlation Eq. (10) presented by NREL in 2003 have high estimation deviation especially during night time. This is probably due to the fact that the coefficients of the correlation are site and climate depended.

As mentioned before, the equations giving the best results are Eq. (1) and (8). Both equations are similar in their structure, one of them has a heat convection coefficient whereas the other equation does not have this coefficient, but instead it has wind speed data which is related to the convection coefficient.

The Eq. (2), (6), (7) and (9) all have similar terms containing STC/NOCT values taken from the datasheets. However, they contain differing additional terms. They all have higher deviations than Eq. (1) and (8) which may be an indication on the weak correlation of the outdoor performances of the modules on their standard parameters given in the datasheet.

The performance of the remaining equations (3) and (4) do not perform well as the others. Finally, Eq. (5) interestingly gives the best results after Eq. (1) for the a-Si / μc-Si and the HIT modules and better than Eq. (8) for the other modules, but the differences are not quite significant. Thus, Eq. (5) could be accepted to be the best to use in the prediction of the yield of a PV power plant.

Fig. 3a, b, and c give three typical days of clear, partially cloudy and overcast sky for comparison of the best- (either of Eq. (1) or (8)) and lowest-performing (either of Eq. (4) or (10)) estimation models at different irradiation conditions. For the clear day in July for both of the models the estimation results highly fluctuate for the irradiance values between 400 and 1100 W/m^2. The fluctuations for the best-performing model are lower for the HIT and the a-Si / μc-Si and for the lowest-performing model for the other modules. Possible reasons may be the sensitivity of the structure of the models to the variations of the parameters of different type modules. The lowest-performing model overestimates while the best-performing model underestimates in general and this information may be used for further modification of the models.

The best- and lowest-performing models both seem better performing for the partially cloudy day of May (Fig. 3b) except the a-Si / μc-Si module. Hence, in the irradiance ranges of 400-600 W/m^2 the models perform better, so in modest (lower solar irradiance) climatic conditions the estimations are better than in clear sky conditions, and this will further be demonstrated in the following for the overcast sky day.

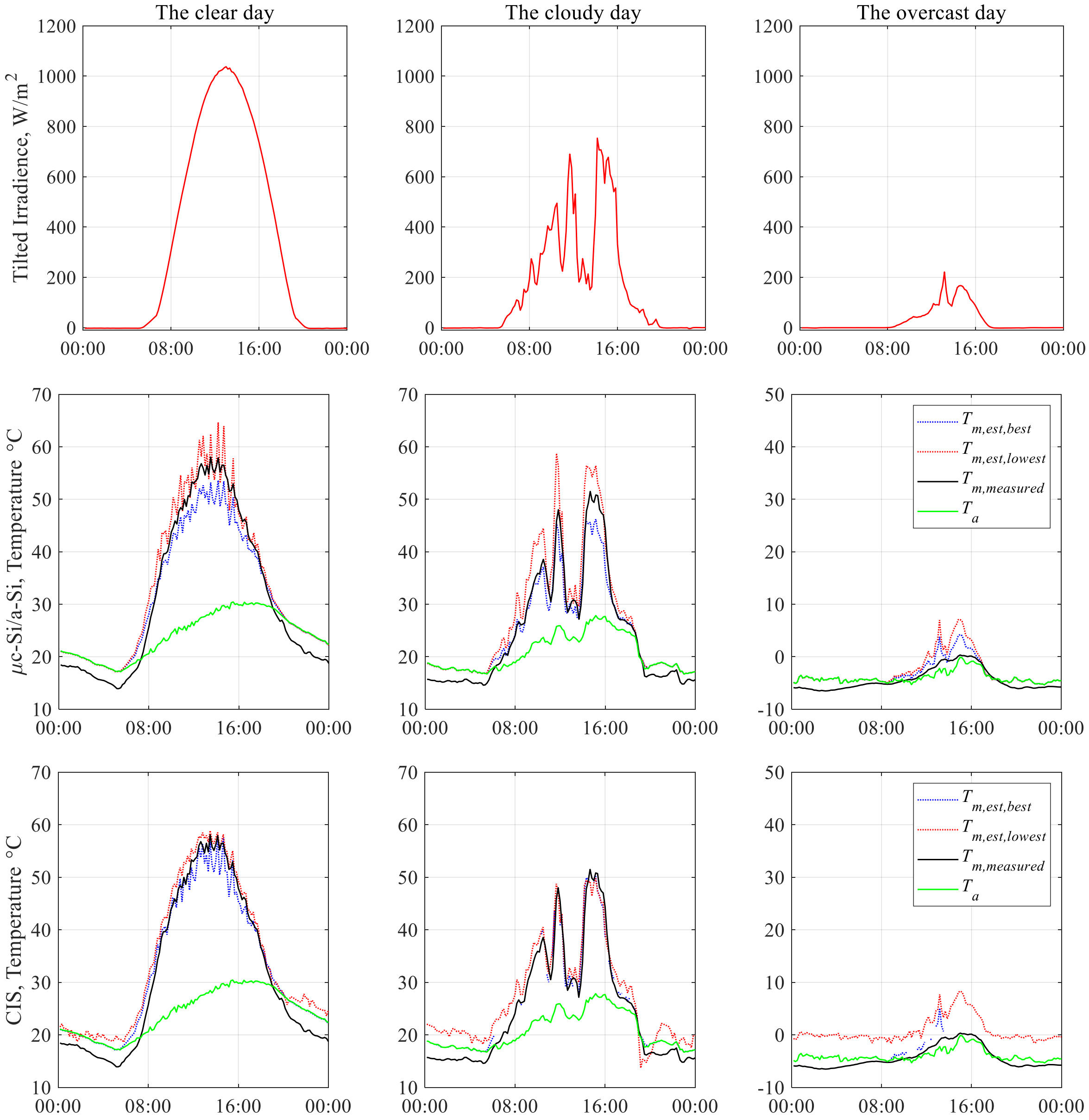

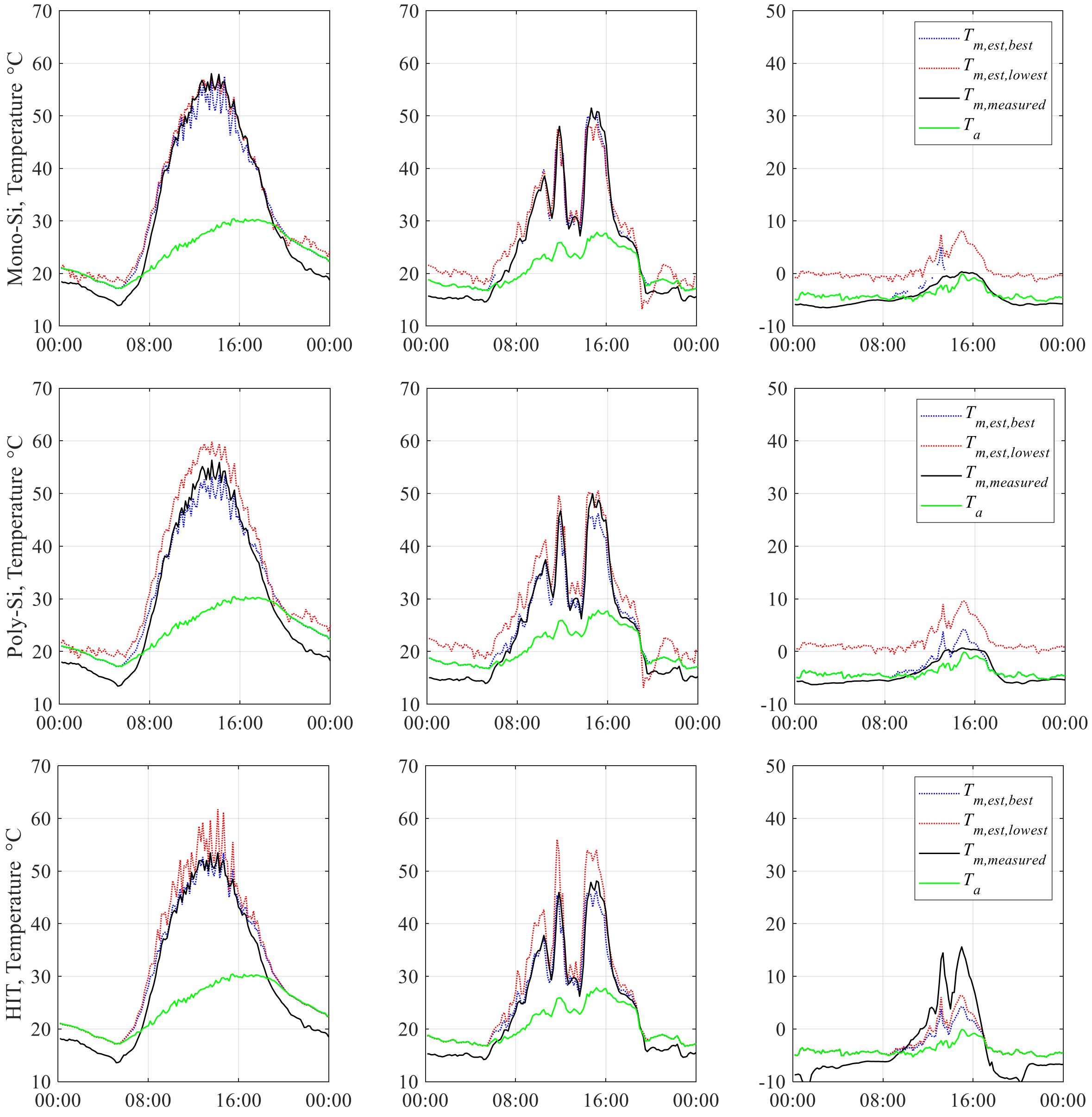

(a) (b) (c)

Fig. 3. Comparison measured module temperatures with estimated module temperatures corresponding to best- and lowest-performing results of all module types from Table 5.

The overcast sky of the day in January (Fig. 3c) the irradiance values do not exceed 200 W/m^2, and the ambient temperature is always below 0 °C. The module temperatures are also very low which can be attributed to the very low or no module yields. That is, the module temperature simply follows the ambient temperature closely and the difference is due to thermal response of the module structures under equilibrium conditions. The best-performing model for the CIS and the Mono-Si (Eq. (8)) does not make predictions for hours with zero wind speed, so the predictions are missing for some of the hours of this specific day.

4. CONCLUSIONS

Prediction of the module temperature is very important in the techno-economic analysis of the PV power plants to estimate the yields. There are many models appeared in the literature for the module temperature predictions. In the present study three years measured module temperatures of the five modules tested in outdoor conditions are analyzed. We have chosen ten models from the literature which are commonly used and constructed for all module types and compared their performances.

The models having a smaller number of parameters (Eq. (1) and (8)) perform better than the others for different modules, and this may be attributed to the various climatic conditions that the data were collected to construct the models. That is, larger the number of parameters/coefficients larger the variations of these parameters at different conditions. Eq. (5), which also has smaller number of parameters/coefficients, seems the best in general than the others, for all the module types. On the other hand, we can state that the prediction performance of the other models also seems acceptable.

This work is performed using the outdoor performance data of the modules under cold and semi-arid climate of Central Anatolia. Such analyses should be carried out for different climates to decide on the best performing model for different climatic conditions. Another further research topic is to carry out the analysis to consider the seasonal variations in the performances of the models to reach better yield estimation calculations.

ACKNOWLEDGMENTS

The authors acknowledge the support given by the Ministry of Development for the construction of the outdoor testing facility.

NOMENCLATURE

$\boldsymbol{a}$	Empirically-determined coefficient establishing the upper limit for module temperature at low wind speeds and high solar irradiance $(\boldsymbol{dimensionless})$	$\boldsymbol{\tau}$	Transmittance coefficient $(\boldsymbol{dimensionless})$
$\boldsymbol{\alpha}$	Absorptance coefficient $(\boldsymbol{dimensionless})$	$\boldsymbol{T_a}$	Ambient temperature (°$\boldsymbol{C}$)
$\boldsymbol{b}$	Empirically-determined coefficient establishing the rate at which module temperature drops as wind speed increases $(\boldsymbol{s/m})$	$\boldsymbol{T_{a,NOCT}}$	Ambient temperature at NOCT (°$\boldsymbol{C}$)
$\boldsymbol{\beta_{STC}}$	Temperature coefficient of $\boldsymbol{P_{mpp}}$ $(\boldsymbol{1/°C})$	$\boldsymbol{T_c}$	Cell temperature (°$\boldsymbol{C}$)
$\boldsymbol{\eta_{STC}}$	Efficiency at STC $(\boldsymbol{dimensionless})$	$\boldsymbol{T_m}$	Module temperature (°$\boldsymbol{C}$)
$\boldsymbol{G_{NOCT}}$	Irradiance at NOCT $(\boldsymbol{W/m^2})$	$\boldsymbol{T_{m,NOCT}}$	Module temperature at NOCT (°$\boldsymbol{C}$)
$\boldsymbol{G_t}$	Solar radiation flux on module plane $(\boldsymbol{W/m^2})$	$\boldsymbol{T_{m,STC}}$	Module temperature at STC (°$\boldsymbol{C}$)
$\boldsymbol{h_w}$	Air forced heat convection coefficient, $(\boldsymbol{KWm^{-2}})$	$\boldsymbol{U_0, U_1}$	A coefficient describing the effect of the radiation on the module temperature $(\boldsymbol{W/m^2°C})$, A coefficient describing the cooling by the wind $(\boldsymbol{Ws/m^3°C})$
$\boldsymbol{h_{w,NOCT}}$	Air forced heat convection coefficient at NOCT, $(\boldsymbol{KWm^{-2}})$	$\boldsymbol{U_L}$	Overall thermal loss coefficient $(\boldsymbol{Wm^{-2}/°C})$
$\boldsymbol{\omega}$	Mounting coefficient $(\boldsymbol{dimensionless})$	$\boldsymbol{U_{PV}}$	Heat exchange coefficient for total PV surface area $(\boldsymbol{K/Wm^{-2}})$
$\boldsymbol{\omega_1}$, $\boldsymbol{\omega_2}$, $\boldsymbol{\omega_3}$, c	Correlation constants, $(\boldsymbol{dimensionless}$, $\boldsymbol{°C/Wm^{-2}}$, $\boldsymbol{°C/ms^{-1}}$, $\boldsymbol{°C})$	$\boldsymbol{V_W}$	Wind speed $(\boldsymbol{m/s})$

APPENDIX

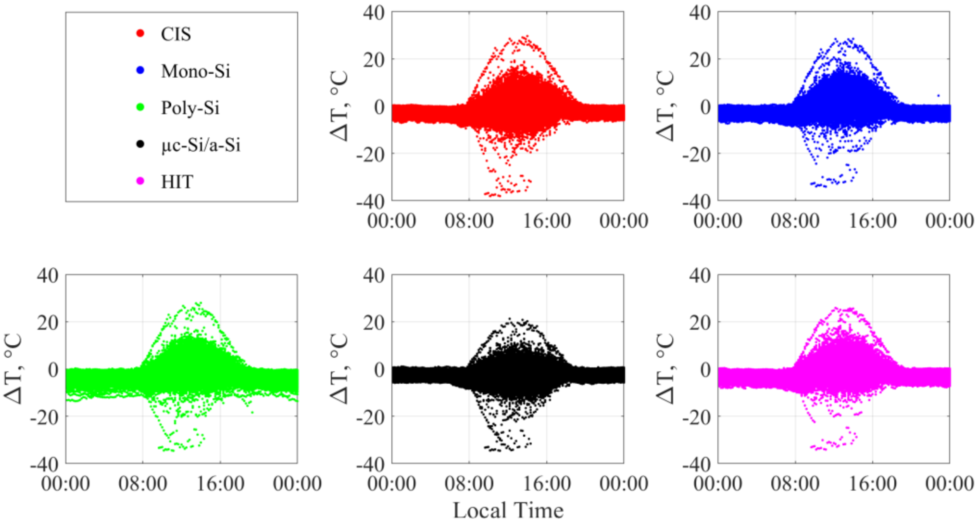

Fig. A1. Difference of module temperatures measured and estimated with Eq. (1).

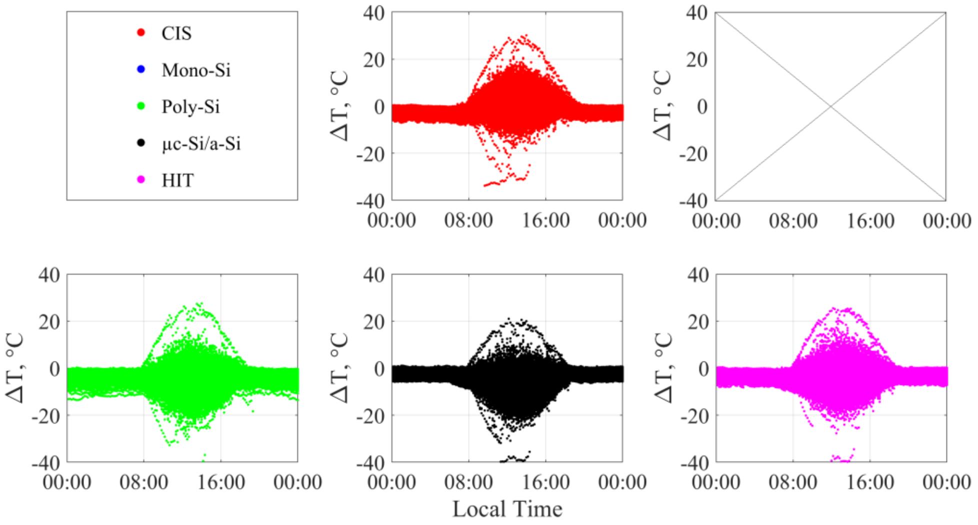

Fig. A2. Difference of module temperatures measured and estimated with Eq. (2).

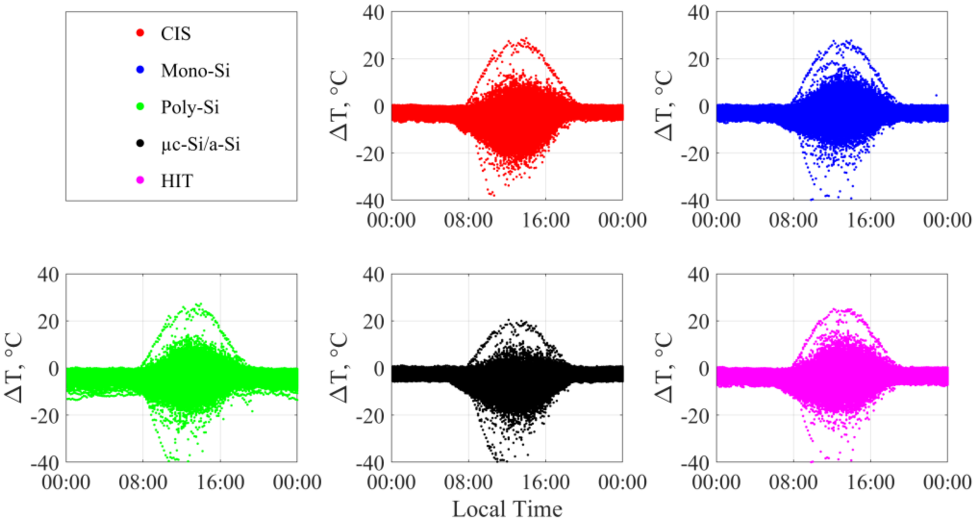

Fig. A3. Difference of module temperatures measured and estimated with Eq. (3).

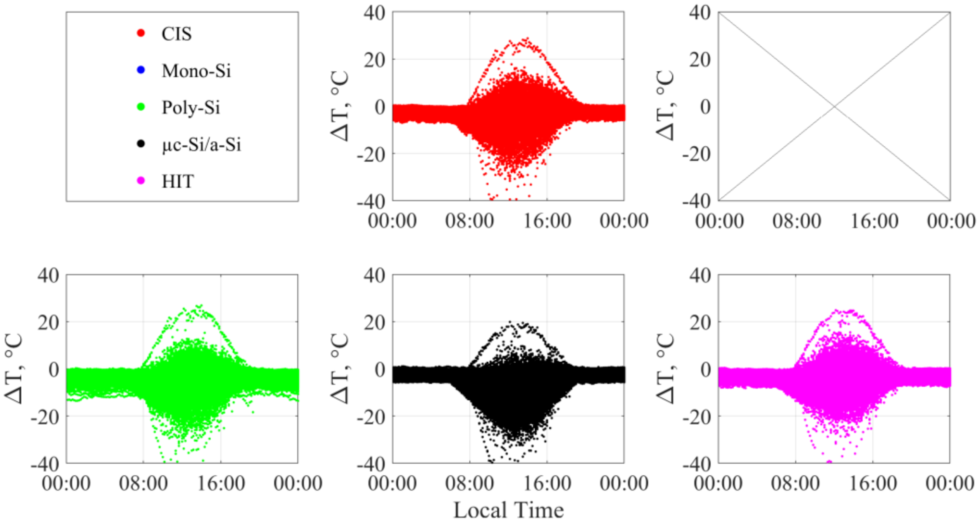

Fig. A4. Difference of module temperatures measured and estimated with Eq. (4).

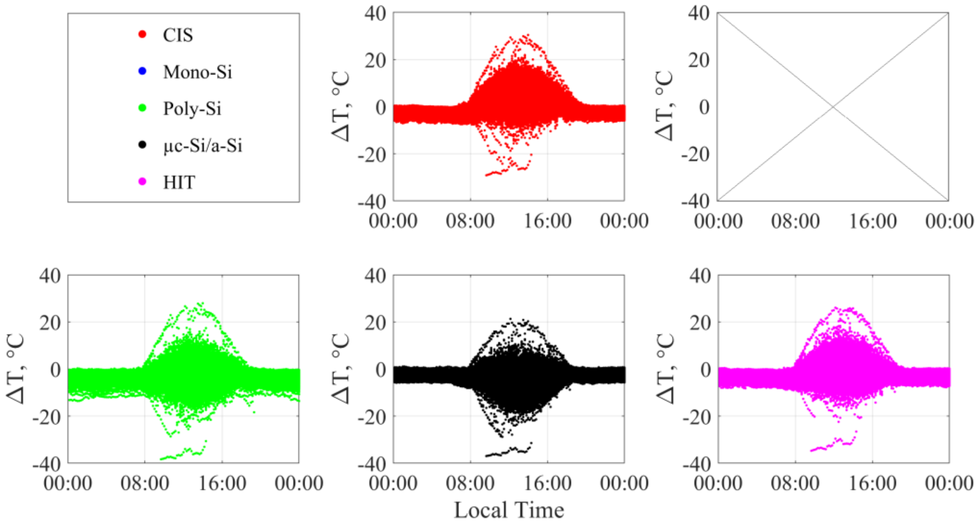

Fig. A5. Difference of module temperatures measured and estimated with Eq. (5).

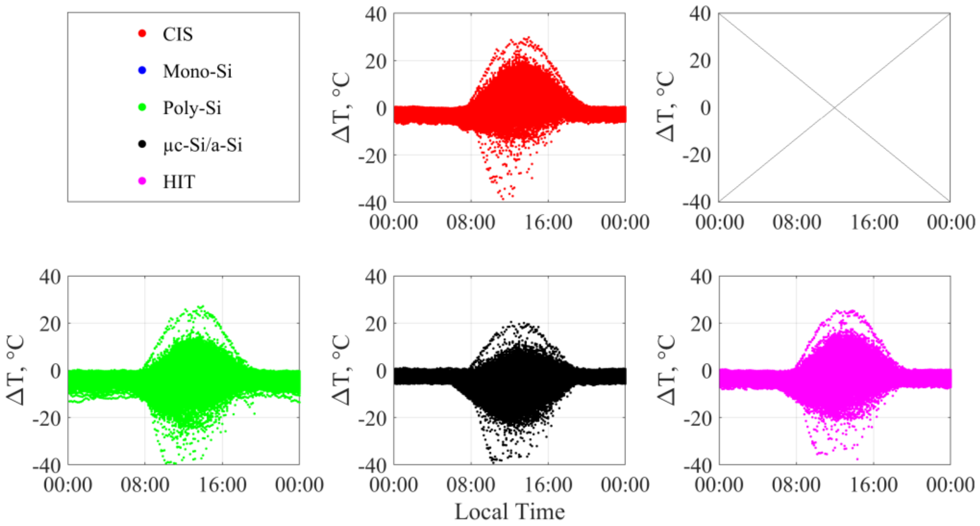

Fig. A6. Difference of module temperatures measured and estimated with Eq. (6).

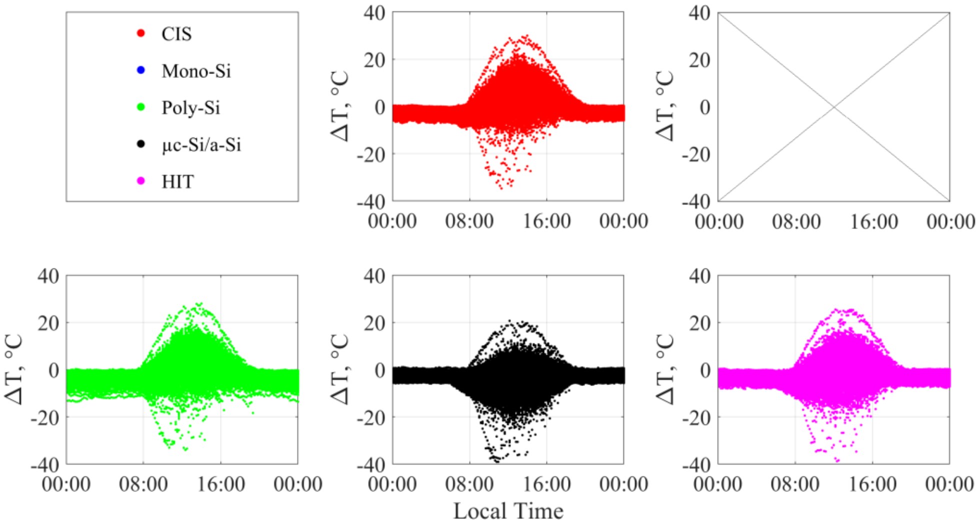

Fig. A7. Difference of module temperatures measured and estimated with Eq. (7).

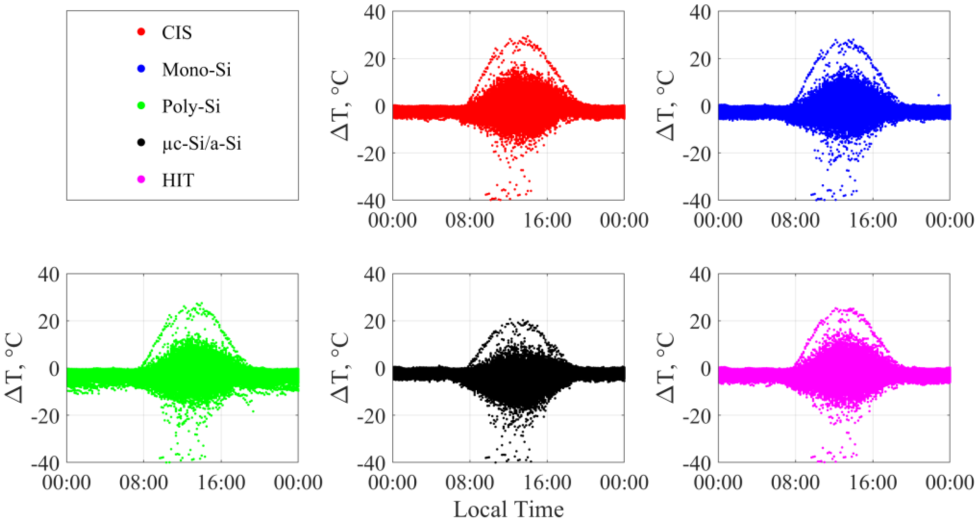

Fig. A8. Difference of module temperatures measured and estimated with Eq. (8).

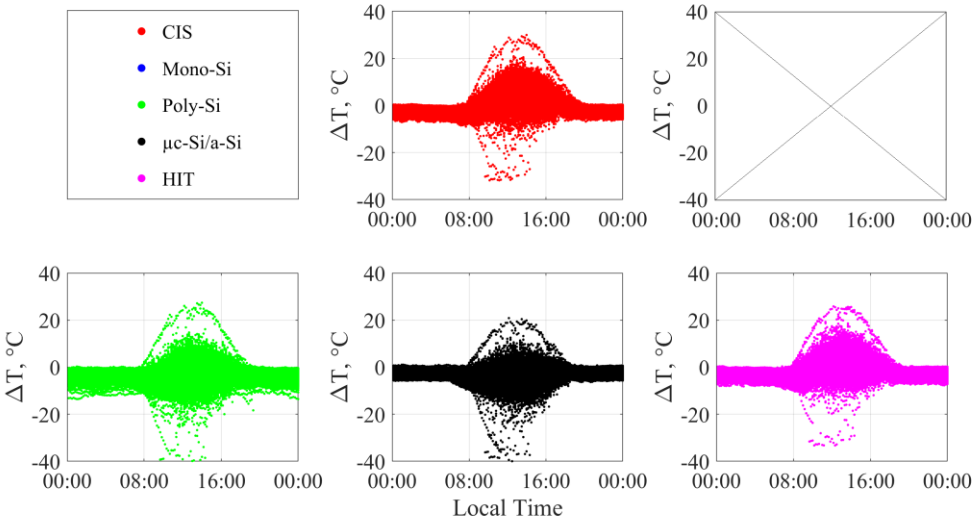

Fig. A9. Difference of module temperatures measured and estimated with Eq. (9).

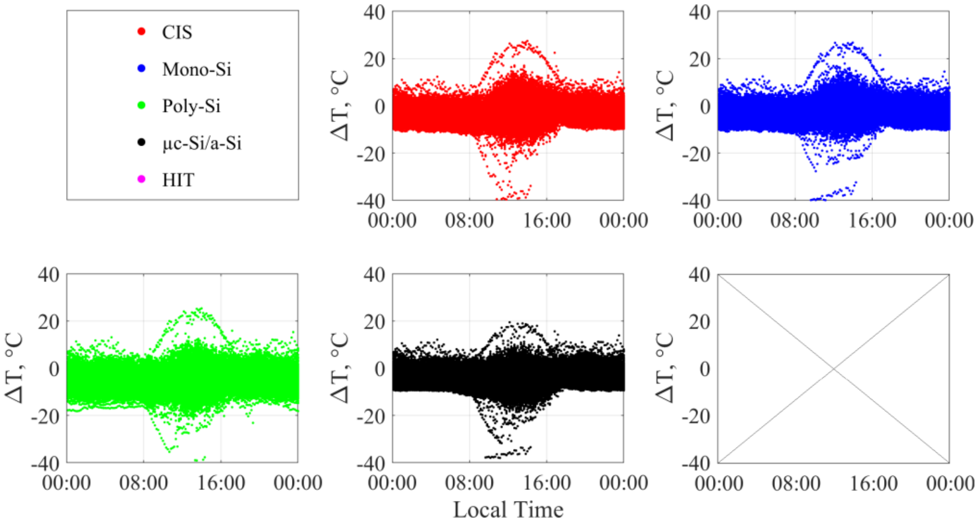

Fig. A10. Difference of module temperatures measured and estimated with Eq. (10).

REFERENCES

Akhsassi, M. *et al*. (2018). “Experimental Investigation and Modeling of the Thermal Behavior of a Solar PV Module.” *Solar Energy Materials and Solar Cells,* Vol.180, pp. 271–79.

Amr, Ayman Abdel raheim, A. A.M. Hassan, Mazen Abdel-Salam, and Abou Hashema M. El-Sayed. (2019). “Enhancement of Photovoltaic System Performance via Passive Cooling: Theory versus Experiment.” *Renewable Energy,* Vol.140, pp. 88–103.

Bañuelos-Ruedas, F., C. Angeles-Camacho, and S. Rios-Marcuello. (2010). “Analysis and Validation of the Methodology Used in the Extrapolation of Wind Speed Data at Different Heights.” *Renewable and Sustainable Energy Reviews,* Vol.14, No.8, pp. 2383–2391.

Lo Brano, Valerio, and Giuseppina Ciulla. (2013). “An Efficient Analytical Approach for Obtaining a Five Parameters Model of Photovoltaic Modules Using Only Reference Data.” *Applied Energy,* No.111, pp. 894–903.

Cole, R J, and N S Sturrock. (1977). “The Convective Heat Exchange at the External Surface of Buildings.” *Building and Environment,* Vol.12, No.4, pp. 207–14.

Dierauf, Timothy, Aaron Growitz, Sarah Kurtz, and Clifford Hansen. (2013). “Weather-Corrected Performance Ratio Technical Report NREL/TP-5200-57991.” *Technical Report, No. NREL/TP-5200-57991* NREL/TP-52, pp. 1–16.

Ding, Kun, Jingwei Zhang, Xingao Bian, and Junwei Xu. (2014). “A Simplified Model for Photovoltaic Modules Based on Improved Translation Equations.” *Solar Energy,* Vol. 101, pp. 40–52.

Dubey, Swapnil, Jatin Narotam Sarvaiya, and Bharath Seshadri. (2013). “Temperature Dependent Photovoltaic (PV) Efficiency and Its Effect on PV Production in the World – A Review.” *Energy Procedia,* Vol. 33, pp. 311–21.

Duffie, John A., and William A. Beckman. (2013). *Solar Engineering of Thermal Processes*, Wiley 4. Edition, New Jersey, USA.

Eckstein, Jürgen Helmut. (1990). “Detailed Modelling of Photovoltaic System Components.” Master Thesis, University of Wisconsin-Madison.

Faiman, David. (2008). “Assessing the Outdoor Operating Temperature of Photovoltaic Modules.” *Progress in Photovoltaics: Research And Applications,* Vol.16, pp. 307–15.

Gökmen, Nuri *et al*. (2016). “Investigation of Wind Speed Cooling Effect on PV Panels in Windy Locations.” *Renewable Energy,* Vol. 90, pp. 283–90.

Homer Pro 3.13 Help Documentation, https://www.homerenergy.com/products/pro/docs/latest/how_homer_calculates_the_pv_cell_temperature.html [Accessed 20 Oct 2019].

IEA. (2019). Report: *PVPS 2019 Snapshot of Global PV Markets, Task 1: Strategic PV Analysis & Outreach*.

IRENA. (2019). Report: 1 International Renewable Energy Agency *Renewable Energy Statistics 2019*.

Kaplani, E, and S Kaplanis. (2014). “Thermal Modelling and Experimental Assessment of the Dependence of PV Module Temperature on Wind Velocity and Direction, Module Orientation and Inclination.” *Solar Energy,* Vol. 107, pp. 443–60.

King, David L, William E Boyson, and Jay A Kratochvil. (2004). Report: *Photovoltaic Array Performance Model,* No: SAND2004-3, Springfield.

Koehl, Michael, Markus Heck, Stefan Wiesmeier, and Jochen Wirth. (2011). “Modeling of the Nominal Operating Cell Temperature Based on Outdoor Weathering.” *Solar Energy Materials and Solar Cells,* Vol. 95, No. 7, pp. 1638–46.

Kurtz, Sarah *et al*. (2009). “Evaluation of High-Temperature Exposure of Rack-Mounted Photovoltaic Modules.” *Conference Record of the IEEE Photovoltaic Specialists Conference*, Philadelphia, PA, USA, pp. 002399–002404.

Loveday, D L, and A H Taki. (1996). “Convective Heat Transfer Coefficients at a Plane Surface on a Full-Scale Building Facade.” *International Journal of Heat and Mass Transfer,* Vol. 39, No. 8, pp.1729–42.

Mattei, M. *et al*. (2006). “Calculation of the Polycrystalline PV Module Temperature Using a Simple Method of Energy Balance.” *Renewable Energy,* Vol. 31, No.4, pp. 553–67.

Nolay, Pierre. (1987). “Developpement d’une Methode Generale d’analyse Des Systemes Photovoltaiques.”, PhD Thesis, ENMP, Paris, http://www.theses.fr/1987ENMP0052.

Ozden, Talat, Doga Tolgay, and Bulent G. Akinoglu. (2018). “Daily and Monthly Module Temperature Variation for 9 Different Modules.” *PVCon 2018 - International Conference on Photovoltaic Science and Technologies,* Ankara, Turkey, Doi: 10.1109/PVCon.2018.8523878.

Peel, M. C., B. L. Finlayson, and T. A. McMahon. (2007). “Updated World Map of the Köppen-Geiger Climate Classification.” *Hydrology and Earth System Sciences,* Vol. 11, No. 5, pp. 1633–44.

PVsyst 6 Help Doc. https://www.pvsyst.com/help/ [15 Oct 2019].

Rahman, M. M., M. Hasanuzzaman, and N. A. Rahim. (2015). “Effects of Various Parameters on PV-Module Power and Efficiency.” *Energy Conversion and*

Management, Vol. 103, pp. 348–58.

Roberts, Justo José, Andrés A. Mendiburu Zevallos, and Agnelo Marotta Cassula. (2017). “Assessment of Photovoltaic Performance Models for System Simulation.” *Renewable and Sustainable Energy Reviews,* Vol. 72, pp. 1104–23.

Ross, R.G., and M.I. Smokler. (1986). Repot: *Electricity from Photovoltaic Solar Cells: Flat-Plate Solar Array Project Final Report*. California.

Rubel, Franz, Katharina Brugger, Klaus Haslinger, and Ingeborg Auer. (2017). “The Climate of the European Alps: Shift of Very High Resolution Köppen-Geiger Climate Zones 1800-2100.” *Meteorologische Zeitschrift,* Vol. 26, No: 2, pp. 115–25.

Sandnes, BjØrnar, and John Rekstad. (2002). “A Photovoltaic/Thermal (PV/T) Collector with a Polymer Absorber Plate. Experimental Study and Analytical Model.” *Solar Energy,* Vol. 72, No. 1, pp. 63–73.

Santhakumari, Manju, and Netramani Sagar. (2019). “A Review of the Environmental Factors Degrading the Performance of Silicon Wafer-Based Photovoltaic Modules: Failure Detection Methods and Essential Mitigation Techniques.” *Renewable and Sustainable Energy Reviews,* Vol. 110, pp. 83–100.

Schwingshackl, C. *et al*. (2013). “Wind Effect on PV Module Temperature: Analysis of Different Techniques for an Accurate Estimation.” *Energy Procedia,* Vol. 40, pp. 77–86.

Sharples, S, and P S Charlesworth. (1998). “Full-Scale Measurements of Wind-Induced Convective Heat Transfer from a Roof-Mounted Flat Plate Solar Collector.” *Solar Energy,* Vol. 62, No. 2, pp. 69–77.

Skoplaki, E., A. G. Boudouvis, and J. A. Palyvos. (2008). “A Simple Correlation for the Operating Temperature of Photovoltaic Modules of Arbitrary Mounting.” *Solar Energy Materials and Solar Cells,* Vol. 92, No. 11, pp. 1393–1402.

Skoplaki, E., and J. A. Palyvos. (2009). “Operating Temperature of Photovoltaic Modules: A Survey of Pertinent Correlations.” *Renewable Energy*, Vol. 34, No. 1, pp. 23–29.

SolarPowerEurope. (2018). Report: *Global Market Outlook.* EPIA - European Photovoltaic Industry Association.

Tamizhmani, Govindasamy *et al.* (2003). “Photovoltaic Module Thermal / Wind Performance : Long -Term Monitoring and Model Development For Energy Rating.” *NCPV and Solar Program Review Meeting,* Denver, Colorado, pp. 936–39.

Twidell, John, and Tony Weir. (2015). *Renewable Energy Resources*. Taylor & Francis 3rd Editio. London.

Turkish Journal of Engineering

Turkish Journal of Engineering (TUJE)
Vol. 4, Issue 4, pp. 197-202, October 2020
ISSN 2587-1366, Turkey
DOI: 10.31127/tuje.644025
Research Article

LOW VELOCITY IMPACT BEHAVIORS OF BASALT/EPOXY REINFORCED COMPOSITE LAMINATES WITH DIFFERENT FIBER ORIENTATIONS

Özkan Özbek *[1], Ömer Yavuz Bozkurt [2] and Ahmet Erkliğ [3]

[1] Kilis 7 Aralık University, Faculty of Engineering and Architecture, Mechanical Engineering Department, Kilis, Turkey
ORCID ID 0000 – 0003 – 1532 – 4262
ozkanozbek@kilis.edu.tr

[2] Gaziantep University, Faculty of Engineering, Mechanical Engineering Department, Gaziantep, Turkey
ORCID ID 0000 – 0003 – 0685 – 8748
oybozkurt@gantep.edu.tr

[3] Gaziantep University, Faculty of Engineering, Mechanical Engineering Department, Gaziantep, Turkey
ORCID ID 0000 – 0003 – 3906 – 3415
erklig@gantep.edu.tr

* Corresponding Author
Received: 07/11/2019 Accepted: 18/01/2020

ABSTRACT

The current study aims to explore the effects of fiber orientation angle on the low velocity impact behaviors of the basalt fiber reinforced composite laminates. Samples with four different orientation angles (0º/90º, 15º/-75º, 30º/-60º and 45º/-45º) fabricated by vacuum assisted resin transfer molding have being tested on the Charpy impact test machine. Furthermore, failure modes of notched/unnotched samples subjected to impact loadings in the flatwise and edgewise directions have been examined to detailly understand fracture behavior. The results showed that the fiber orientation angle has substantial effects on the energy absorption capability and impact toughness of the samples. The increment in fiber orientation angle was led to increases in impact energy and toughness, and the reduction in impact damage. The best values as 3.07 J and 34.82 kJ/m^2 for impact energy and impact toughness, respectively, are obtained from the notched samples in edgewise impact loading that having (45º/-45º) fiber orientation angle. Almost all of the samples exhibited failure modes as matrix fragmentation, delamination, fiber cracking and fiber pull-out, respectively. The most destructive results were observed as laminate fracture on the samples having (0º/90º) fiber orientation angle.

Keywords: *Basalt Fiber, Charpy, Fiber Orientation Angle, Energy Absorption, Impact Toughness*

1. INTRODUCTION

With the awareness of industrialization that is growing faster than ever on a global scale, engineers and scientists are strictly working in many industrial fields to facilitate life and meet the increasing consumption demands of humans. As a result of these efforts, materials science has been making great progress by persistently dealing with the development or derivation of new materials in terms of affordability, productivity and design flexibility compared to the conventional engineering materials. In this context, polymer based composite materials by exhibiting higher specific strength and durability, longer service life and fatigue behavior compared to the classical metallic materials (Zhong & Joshi, 2015) have been derived. The ease of production, tailorability, resistance to corrosion, better damping behavior and excellent fatigue resistance are also some of the other advantages of composite materials.

Polymeric composites are composed of a reinforcement phase, generally in the form of fiber or particle, and a matrix phase. Due to their superior mechanical and dynamic performance, fiber reinforced polymeric composites have found application areas in a wide variety of industry fields including domestic, sports, transportation, military and aerospace industries. Carbon fiber with its high specific strength and specific stiffness, and the glass fiber with its high chemical resistance, impact toughness and low cost, have become the most widely used fiber types in the polymeric composites. Despite all their good properties, the search for new promising fiber types, in terms of organic, inorganic, synthetic or natural, that do not possess the weaknesses of carbon and glass fibers are also continued.

In today's world, the use of natural materials in engineering applications has an increasing trend to meet the stringent environmental regulations enforced by public policies. In that sense despite its wide use in other fields, the use of basalt as fiber reinforcement in polymeric composites are relatively new compared to glass and carbon fiber (Jamshaid *et al.*, 2017). Basalt, obtained from molten volcanic rocks, is an eco-friendly, natural, harmless and recyclable material. Furthermore, with its considerable properties such as good mechanical strength, non-flammable, high temperature resistance, biological stability, and high resistance to chemicals, have been attracted the attention of the researchers. In the literature, there are many studies that investigated the physical, mechanical and dynamic properties of basalt fiber reinforced polymeric composites (Amuthakkannan *et al.*, 2013; Zhang *et al.*, 2012;, Botev *et al.,* 1999, Czigany *et al.*, 2008; Colombo *et al.*, 2012, Demirci *et al.*, 2014; Bozkurt *et al.*, 2016; Bozkurt *et al.*, 2018; Sim & Park, 2005). Elmahdy *et al*. (2019) examined the effect of strain rate on the tensile characteristics of woven basalt fiber reinforced composite laminates using a split Hopkinson tension bar. They stated that poison's ratio, stiffness, tensile strength and tensile strain of the samples increased with higher strain rate for both warp and fill directions. Amuthakkannan *et al.* (2013) studied the tensile, flexural and impact properties of short basalt fiber reinforced polymer composites and showed that the length of basalt fiber has significant effect on tensile, flexural and impact properties together with the fiber weight fraction. Zhang *et al*. (2012) examined the variation in tensile, flexural, impact and fracture behaviors of basalt fiber reinforced poly(butylene succinate) composites with respect to basalt fiber content. An increase in tensile, flexural and thermal properties with an increase in basalt fiber loading up to 15vol% were reported. Botev *et al*. (1999) assessed viscoelastic properties of untreated short basalt fiber reinforced polypropylene composites. Deterioration in tensile and impact properties of PP matrix were shown with the inclusion of untreated short basalt fiber reinforcements. However, after the addition of poly(propylene-g-maleic anhydride) significant increases in those properties were revealed. Zhao *et al*. (2019) researched the effect of temperature on the static and tension-tension fatigue properties of basalt fiber reinforced polymers. The life time, stiffness degradation, displacement behaviors of samples exposed to five different temperature environment as -20, 0, 20, 40 and 60 °C were investigated. Czigany *et al*. (2008) explored the crack propagation response of basalt fiber reinforced polypropylene composite. The results outlined that basalt fiber reinforcement provides increase in fracture toughness of polypropylene (PP) matrix. Colombo *et al.* (2012) investigated the mechanical properties and fatigue behavior of basalt fiber reinforced composites. Improvements in tensile and compressive strengths were presented as a result of basalt fiber reinforcement. Demirci *et al*., (2014) researched the fracture toughness characteristics of the basalt and glass fiber reinforced having arc shaped samples. Charpy impact experiments were conducted to examine the effects of the different notch depth ratios on the energy characteristics of the samples. Increasing in the considered ratios resulted with the decreasing in impact energy and fracture toughness values. Also, basalt fiber reinforced samples showed the better features than glass ones. Less *et al*. (2019) carried out the effects of fiber length and compatibilizing agents on mechanical and thermomechanical behaviors of basalt fiber reinforced polyamide composites. It was found that the stiffness of long fiber basalt composites are much higher. Bozkurt *et al*. (2016) examined the effects of the different fiber orientation angle on the vibration and damping behaviors of the basalt fiber reinforced composites. They stated that the higher fiber orientation angle resulted in decrease of natural frequency and increase of damping ratios. Subagia *et al*. (2014) conducted a study about the effects of hybridization of basalt and carbon fibers on the flexural characteristics. They pointed out the hybridization process gave the new materials with less cost compared to carbon fiber reinforced samples and comparable flexural strength and improved ductility.

The aim of this work is to investigate the effects of the fiber orientation angle on the energy absorption characteristics of the basalt fiber reinforced composite laminates. The samples with four different orientation angles ((0º/90º), (15º/-75º), (30º/-60º) and (45º/-45º)) were prepared using the stack of eight basalt fabric layers and subjected to low velocity impact tests. The fracture surface of samples were examined to explore the effect of fiber orientation on fracture mechanism.

2. MATERIALS AND METHOD

2.1. Sample Preparation

The bidirectional basalt fiber fabrics procured from

Tila Kompozit, Turkey, were used for reinforcement component. For matrix system, epoxy resin (MOMENTIVE MGS L285) and hardener (MOMENTIVE MGS H285) which were supplied from Dost Kimya, Turkey, were mixed with a stoichiometric ratio of 100:40 in weight basis, respectively. The physical properties of raw materials were given in Table 1.

Table 1. The physical properties of raw materials

Material	Density	Thickness
Basalt fabric	200 g/m^2	0.17 mm
Epoxy	1.18 g/m^3	-
Hardener	0.94 g/m^3	-

Basalt fiber reinforced composite laminate was fabricated by vacuum assisted resin transfer molding technique (VARTM) seen in Figure 1. The fabric preforms having dimensions of 250 mm x 300 mm were stacked over the mold plate. Then, the fabric stackings were covered by a peel ply to easily remove composite laminates from the mold after the fabrication. A resin distribution medium was placed over the peel ply to ensure a uniform resin system injection to fabric stacks. The resin system was injected into mold structure with the help of vacuum. Following the soak of fabrics, the mold structure was held under 700 mm-Hg vacuum at 40ºC temperature for 8 hours to complete curing process. By the completion of curing, the laminate was left to cool at room temperature for the next 24 hours. The thickness of the laminate, shown in Figure 2, was measured as 1.6 mm. The test coupons were removed from the composite laminates using the CNC router in accordance with ISO 179/92 test standard.

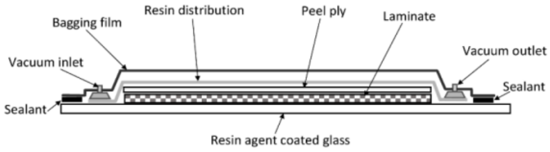

Fig. 1. Vacuum assisted resin transfer molding (VARTM) (Bozkurt *et al.*, 2018)

Fig. 2. Basalt/epoxy fiber reinforced composite laminate

2.2. Low Velocity Impact Tests

Charpy impact tests were performed to determine the effects of fiber orientation angle on the impact energy and toughness characteristics of the basalt fiber reinforced composite laminates. ISO 179/92 standard was used for reference guide for the sample preparation and testing procedure. A Kögel 3/70 Charpy impact tester with 15.0 J impact energy capacity, shown in Figure 3(a), were employed for the experiments. The samples having 55 mm x 10 mm in length and width were prepared as notched and unnotched configurations subjected to edgewise and flatwise impact loading as seen in Figure 3(b) and 3(c), respectively. At least five samples were tested to ensure experimental reliability.

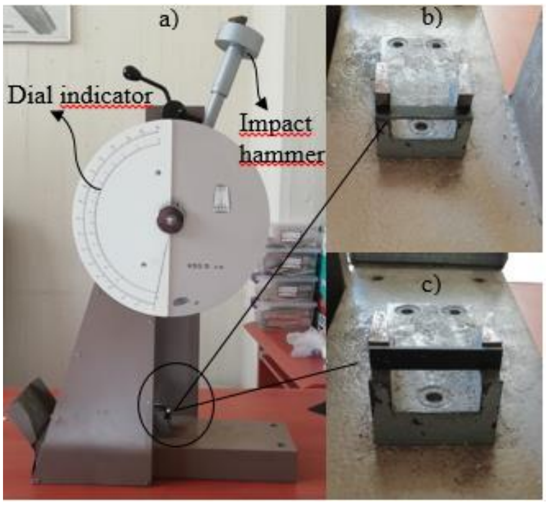

Fig. 3. a) Köger 3/70 Charpy impact tester, b) edgewise impact, c) flatwise impact

Impact energy, E, was directly measured from the dial on the machine using potential energy lost after breaking the sample as shown in Eq. (1).

$$E = E_a - E_b \tag{1}$$

where E_a and E_b represent the pendulum energy before and after impact event, respectively. Impact toughness, a_{cu} which is the absorbed energy per unit area, was calculated from Eq. (2):

$$a_{cu} = E/(bh) \tag{2}$$

where b and h are the thickness and width of the samples. Figure 4 also presents an illustration of Charpy impact test machine.

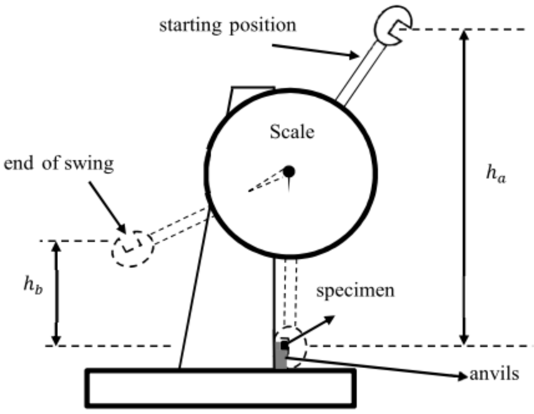

Fig. 4. The schematic illustration of the Charpy impact test

3. RESULTS AND DISCUSSIONS

Charpy impact test is a practical and an economic method to comparatively determine the failure characteristics of composite laminates (Bozkurt *et al*., 2018). In this section, the results of the Charpy impact tests in terms of the energy absorption capability, impact toughness and impact damages were summarized to detailly analyze the influence of the fiber orientation on low velocity impact response. The impact damages were also examined by taking photos with a manual camera to monitor fracture characteristics of basalt fiber reinforced composite laminates.

Impact energy and impact toughness values of the samples subjected to the impact loadings in the flatwise and edgewise directions were presented in Figure 5 and Figure 6, respectively. The edgewise impacted samples had the better response than flatwise impacted ones due to exhibition of more resistance behavior in edgewise direction. This appears to be compatible with the findings of Dhar's study (Dhar *et al*., 2018) who reported that higher fracture energy is necessary for the crack initiation phenomenon in edgewise direction of composite laminates. Furthermore, laminate impact position had the larger width in edgewise orientation as reported in literature (Dhar *et al*., 2019).

It was proved that fiber orientation angle had the significant effects on laminates, experimentally. The results showed that an increase in fiber orientation angle resulted with an increase in both absorbed energy and the impact toughness of the material. This can be explained by the easier pull out failure mode (Flasar, 2018) happening in smaller orientations. Additionally, this situation may be explained by the findings of a literature study (Sharma *et al*., 2019) indicating the first cracking energy was higher for composite laminates with (45º/-45º) fiber orientation angle accumulating lower impact damage. For the notched samples, the maximum absorbed energy and impact toughness as 1.73 J and 3.09 kJ/m^2 was obtained from the (45º/-45º) fiber orientation angle. When compared to (0º/90º) fiber orientation, 22.7% and 23.1% increase were achieved in impact energy and toughness values, respectively.

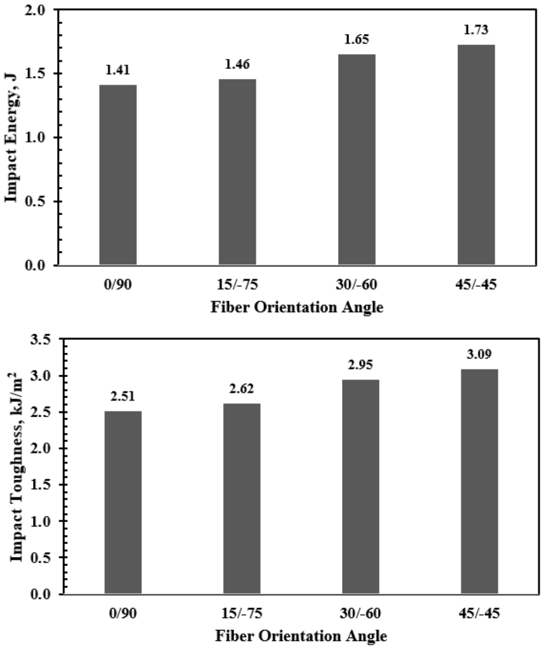

Fig. 5. Absorbed energy and impact toughness of the unnotched samples subjected to flatwise impact loading

With the increase in fiber orientation angle, the samples subjected to edgewise impact loadings showed an increasing trend, in impact energy and toughness, like the flatwise impacted samples. Compared to (0º/90º) fiber orientation, the (45º/-45º) fiber orientation angle exhibited 2.03 times higher values in both impact energy and toughness. Maximum absorbed impact energy and impact toughness values were found as 3.07 J and 34.82 kJ/m^2.

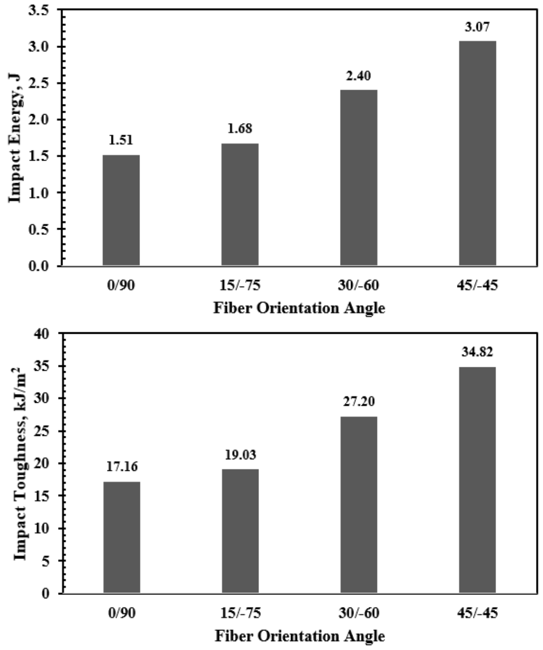

Fig. 6. Absorbed energy and impact toughness of the notched samples subjected to edgewise impact loading

The failure modes and damage types of the flatwise and edgewise impacted samples after Charpy impact tests were given in Figure 7(a) and Figure 7(b), respectively. It was obvious that higher fiber orientations showed the less damage. This is explained by the higher resistance to first crack initiation formation in damaged areas of the samples. Also, edgewise impacted samples showed more destruction compared to flatwise impacted ones since required higher fracture energy.

It was observed that the failure modes were started with matrix cracking and followed by delamination, fiber breakage and fiber pull out as the fiber orientation angle decreased in unnotched samples. However, failure mode as fiber breakage was triggered by matrix cracking and delamination caused from matrix-fiber decomposition, especially in (15º/-75º) and (30º/-60º) fiber orientations of edgewise-notched samples. The sample of (0º/90º) fiber orientation showed matrix fragmentation followed by fiber breakage, causing irregular fiber placement on the damage surface. An irregular matrix cracking was shown for the sample of (0º/90º) fiber orientation.

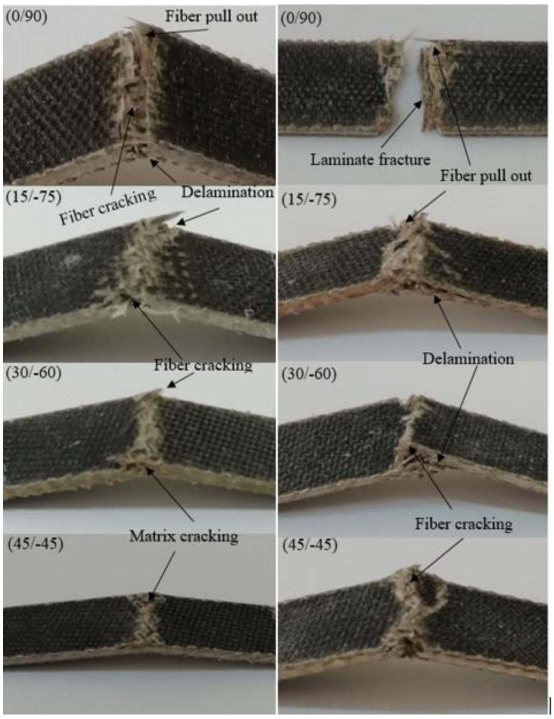

(a) (b)

Fig. 7. Damage types for; (a) unnotched samples subjected to flatwise impact, (b) notched samples subjected to edgewise impact

4. CONCLUSIONS

In this work, the effect of fiber orientation angle on the low velocity impact behavior of the basalt fiber reinforced composite laminates were experimentally investigated. The composite samples having four different orientation angles (0º/90º, 15º/-75º, 30º/-60º and 45º/-45º) were prepared using VARTM technique and subjected to Charpy impact tests to determine the impact energy and toughness. The unnotched and notched samples were subjected to flatwise and edgewise impact loadings, respectively. An increase in fiber orientation angle resulted with the increase in energy absorption and impact toughness for all samples. Maximum increases in impact energy and impact toughness were obtained from (45º/-45º) fiber orientation as 22.7% and 23.1% for notched samples. Also, unnotched samples with (45º/-45º) fiber orientation exhibited 2.03 times of energy absorption and toughness values of the samples having (0º/90º) fiber orientation. It was shown that the failure modes were started with matrix cracking and followed by delamination, fiber breakage and fiber pull out as the fiber orientation angle decreased. As seen in the results, the effect of fiber orientation on energy absorption characteristics was very significant. It can be a reference guide for in the usage of related applications.

REFERENCES

Amuthakkannan, P., Manikandan, V., Jappes, J. W., & Uthayakumar, M. (2013). “Effect of fibre length and fibre content on mechanical properties of short basalt fibre reinforced polymer matrix composites.” *Materials Physics and Mechanics*, 16(2), 107-117.

Botev, M., Betchev, H., Bikiaris, D., & Panayiotou, C. (1999). “Mechanical properties and viscoelastic behavior of basalt fiber ‐ reinforced polypropylene.” *Journal of Applied Polymer Science*, 74(3), 523-531.

Bozkurt, Ö. Y., Bulut, M., & Özbek, Ö. (2016). “Effect of fibre orientations on damping and vibration characteristics of basalt epoxy composite laminates.” *In Proceedings of the World Congress on Civil, Structural, and Environmental Engineering (CSEE’16)*, Prague (pp. 30-31).

Bozkurt, Ö. Y., Erkliğ, A., & Bulut, M. (2018). “Hybridization effects on charpy impact behavior of basalt/aramid fiber reinforced hybrid composite laminates.” *Polymer Composites*, 39(2), 467-475.

Colombo, C., Vergani, L. A. U. R. A., & Burman, M. (2012). “Static and fatigue characterisation of new basalt fibre reinforced composites.” *Composite structures*, 94(3), 1165-1174.

Czigány, T., Vad, J., & Pölöskei, K. (2005). “Basalt fiber as a reinforcement of polymer composites.” *Periodica Polytechnica Mechanical Engineering*, 49(1), 3-14.

Demirci, M. T., Tarakçıoğlu, N., Avcı, A., & Erkendirci, Ö. F. (2014). “Fracture toughness of filament wound BFR and GFR arc shaped specimens with Charpy impact test method.” *Composites Part B: Engineering*, 66, 7-14.

Dhar Malingam, S., Subramaniam, K., Lin Feng, N., Fadzullah, S. H. S. M., & Subramonian, S. (2019). “Mechanical properties of plain woven kenaf/glass fiber reinforced polypropylene hybrid composites.” *Materials Testing*, 61(11), 1095-1100.

Dhar Malingam, S., Jumaat, F. A., Ng, L. F., Subramaniam, K., & Ab Ghani, A. F. (2018). Tensile and impact properties of cost ‐ effective hybrid fiber metal laminate sandwich structures. Advances in polymer technology, 37(7), 2385-2393.

Elmahdy, A., & Verleysen, P. (2019). “Tensile behavior of woven basalt fiber reinforced composites at high strain rates.” *Polymer Testing*, 76, 207-221.

Flášar, O. (2018). “Experimental Investigation of CFRP Impact Toughness and Failure Modes.” *Advances in Military Technology*, 13(1).

Jamshaid H. (2017). “Basalt fiber and its applications.” *J Textile Eng Fashion Technol.* 1(6):254-255.

Lee, T. W., Lee, S., Park, S. M., & Lee, D. (2019). “Mechanical, thermomechanical, and local anisotropy analyses of long basalt fiber reinforced polyamide 6 composites.” *Composite Structures*, 222, 110917.

Sharma, A. P., Khan, S. H., & Velmurugan, R. (2019). “Effect of through thickness separation of fiber orientation on low velocity impact response of thin composite laminates.” *Heliyon*, 5(10), e02706.

Sim, J., & Park, C. (2005). “Characteristics of basalt fiber as a strengthening material for concrete structures.” *Composites Part B: Engineering*, 36(6-7), 504-512.

Subagia, I. A., Kim, Y., Tijing, L. D., Kim, C. S., & Shon, H. K. (2014). “Effect of stacking sequence on the flexural properties of hybrid composites reinforced with carbon and basalt fibers.” *Composites Part B: Engineering*, 58, 251-258.

Zhang, Y., Yu, C., Chu, P. K., Lv, F., Zhang, C., Ji, J., ... & Wang, H. (2012). “Mechanical and thermal properties of basalt fiber reinforced poly (butylene succinate) composites.” *Materials Chemistry and Physics*, 133(2-3), 845-849.

Zhao, X., Wang, X., Wu, Z., Keller, T., & Vassilopoulos, A. P. (2019). “Temperature effect on fatigue behavior of basalt fiber‐reinforced polymer composites.” *Polymer Composites*, 40(6), 2273-2283.

Zhong, Y., & Joshi, S. C. (2015). “Impact behavior and damage characteristics of hygrothermally conditioned carbon epoxy composite laminates.” *Materials & Design* (1980-2015), 65, 254-264.

Turkish Journal of Engineering

Turkish Journal of Engineering (TUJE)
Vol. 4, Issue 4, pp. 203-208, October 2020
ISSN 2587-1366, Turkey
DOI: 10.31127/tuje.646603
Research Article

BULGUR INDUSTRY WASTEWATER TREATMENT BY MICROBIAL FUEL CELL – EXPLORATORY STUDY

Mohammed Saleh *[1], Mutlu Yalvaç [2], Luey Halef [3], Muhammed Şahin Hekim [4] and Hüdaverdi Arslan [5]

[1] Mersin University, Graduate School of Natural and Applied Sciences, Environmental Engineering Department, Mersin, Turkey
ORCID ID 0000 – 0002 – 3145 – 4457
muh.saleh89@gmail.com

[2] Mersin University, Engineering Faculty, Environmental Engineering Department, Mersin, Turkey
ORCID ID 0000 – 0002 – 1281 – 5712
myalvac@mersin.edu.tr

[3] Mersin University, Graduate School of Natural and Applied Sciences, Environmental Engineering Department, Mersin, Turkey
ORCID ID 0000 – 0001 – 8784 – 123X
loaaealkhalaf@gmail.com

[4] Mersin University, Graduate School of Natural and Applied Sciences, Environmental Engineering Department, Mersin, Turkey
ORCID ID 0000 – 0001 – 9770 – 0721
voosha0@gmail.com

[5] Mersin University, Engineering Faculty, Environmental Engineering Department, Mersin, Turkey
ORCID ID 0000 – 0002 – 3053 – 6944
harslan@mersin.edu.tr

---

* Corresponding Author
Received: 13/11/2019 Accepted: 23/01/2020

ABSTRACT
The bulgur industry has importance in the food sector in Turkey. The wastewater generated from this industry can be considered bio waste. The microbial fuel cells (MFC) are a relatively new technique aiming to treat the wastewater and producing direct energy. This study aims to explore the degradation efficiency of the organic matters expressed as chemical oxygen demand (COD) founded in bulgur industry wastewater by microbial fuel cell techniques. Furthermore, it aims to study the potential formation of electricity from this type of wastewater. In this study, the MFC – double chamber system was performed. 1.5 L bulgur industry wastewater containing 3% of biomass was used. The COD and the voltage were measured. The COD generated from the bulgur industry wastewater was 28800 mg/L. After using the MFC system, the COD was decreased to reach 2560 mg/L with a removal efficiency of 91%. 1st order kinetic model had the best fit for COD removal with a correlation coefficient (R^2) of 0.95. The maximum and average voltages were 0.448 V~~olt~~ and 0.180 V~~olt~~, respectively. The average voltage for every 1 m^2 was 45 volt. As a result of the exploratory study, the MFC can be used to treat the bulgur industry wastewater and generating energy. But it should be combined with other treatment methods to meet the COD standard limits.

Keywords: *Microbial Fuel Cell; Bulgur Industry Wastewater, Energy Generation; Food Wastewater.*

1. INTRODUCTION

The demand for energy has been increased sharply since the industrial revolution. The energy uses were not limited to industrial activities. It enters the whole civilized activities. One of these activities is the Treatment of wastewater.

Wastewater treatment aims to safely dispose of wastewater without producing any harm for humans or the environment (Templeton and Butler, 2011).The treatment process is an energy-intensive process (Gikas and Tsoutsos, 2015). Tchobanoglous *et al*. (2003) had estimated the energy required for the wastewater treatment by conventional methods to be 1.1-2.4 MJ/1m^3. Gikas and Tsoutsos (2015) stated the needed energy for the small wastewater treatment plants could be higher.

The depletion of nonrenewable energy and the environmental problem related to greenhouse emissions forced towards more sustainable energy (Li *et al*., 2014). Many researchers considered wastewater as an energy source that might be used to partially cover the energy needed to treat it (Gude, 2015, Burkitt *et al*., 2016).

Microbial Fuel Cell (MFC) is a technique with the capability of treating wastewater and generating energy at the same time (Cheng *et al*., 2017). The principle of this technique is using the microorganism as catalysts with an objective of oxidizing organic and inorganic matter and generating electric current (Lee *et al*., 2012). MFC typically consists of aerobic (cathodic) and anaerobic (anodic) chambers. Those chambers separated by a proton exchange membrane. The digestion of organic matters occurs in the anaerobic chambers. The substrate oxidation half-reaction produces electrons and protons. The electron transfer by external resistance while the proton moves through the proton exchange membrane (Habermann, Pommer, 1991; Due *et al*., 2007; Huggins *et al*., 2013). The MFC schematic is shown in Fig. 1.

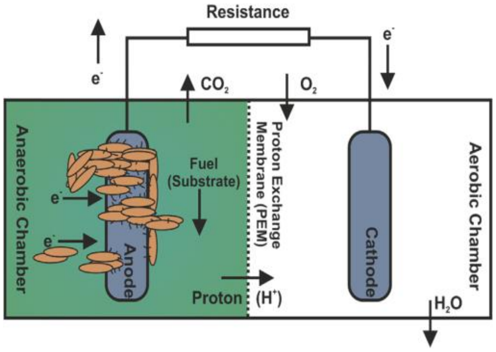

Fig. 1. Schematic plan for two-chamber microbial fuel cell (Du *et al.*, 2007)

The half-reactions for Acetate degradation by the MFC techniques are shown in Equations 1 and 2 (Mohan *et al*., 2007).

Anode reaction:

$$CH_3COO^- + 2H_2O \xrightarrow{(Anaerobic\ Microorganism)} CO_2 + 7H^+ + 8e^- \quad (1)$$

Cathode reaction:

$$O_2 + 4e^- + 4H^+ \rightarrow 2H_2O \quad (2)$$

Microbial fuel cells were employed previously to treat various types of wastewater. Domestic wastewater, Sulfide, palm oil mill effluent, textile wastewater, food waste leachate, and Starch are some of those wastewaters (Köroğlu *et al*., 2014; Lee *et al*., 2012; Hisham *et al*., 2013; Mise and Saware, 2016)

The wastes from the food industry are mostly bio wastes. Starch-containing wastewater always consists of high concentrations of starch and protein, which is an energy source for MFC applications (He *et al*., 2017). The bulgur industry has importance in the food sector in Turkey. The Bulgur production reached 1.25 million/ year, and the annual consumption is about 13 kg/capita (Dünya Gıda Dergisi, 2018).

This study aims to investigate the degradation efficiency of the organic matters expressed as chemical oxygen demand (COD) from bulgur industry wastewater by microbial fuel cell techniques. Also, it aims to study the potential formation of electricity from this type of wastewater.

2. MATERIAL AND METHOD

2.1. Material

The bulgur wastewater was collected from a bulgur factory near Mersin city. The biomass was agglomerated from the outlet of the digester tank in the Karaduvar treatment plant. All of the chemicals used in the study were bought from Sigma-Aldrich. The agitation process was provided by LH-Fermentation equipment. The needed air was provided by the SOBO-SB222 air pump.

2.2. Biomass Percentage Optimization

Different percentages (2, 3, 4, 5 and 10%) of biomass and wastewater were filled into a 15 ml tubes. The tubes were closed with stoppers and placed into the water jar upside down. The jars were inserted into an incubator at 35^{o}C for several days. The volume of the generated methane gas was calculated for each tube by finding the differences between the first and the final level of the liquid. Fig. 2 shows the Biomass optimization process.

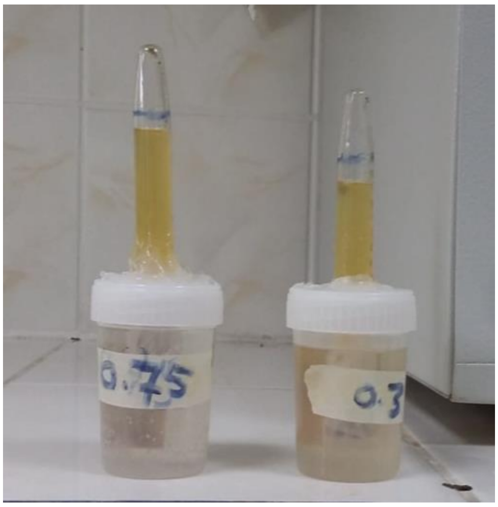

Fig. 2. Biomass optimization process

2.3. MFC Setup

In this study, a double-chambered microbial fuel cell was setup. The anaerobic and aerobic chambers were connected by a salt bridge. The preparation method is shown in the following steps:

2.3.1. Chambers Preparation

In the aerobic chamber, a plastic jar was filled by 5 liters distilled water. Air was injected into the jar to maintain enough aeration. For the anaerobic chamber, 1.5 liters of biomass and bulgur industry wastewater injected into a 2-liter cam jar. The mixture exposed to agitation by a mechanical mixer. Aluminum electrodes with dimensions of (8x5) cm were inserted into the cambers. The electrodes were suspended in the system by alligator clips. The electric wires were connected with external variable resistance.

2.3.2. Salt Bridge Preparation

Due to the high cost of the proton exchange membrane, a salt bridge was used and prepared as follows.

1M of potassium chloride (KCl) was prepared, mixed and heated to the boiling point. At the boiling point, agar (30g) was added gradually to the solution. The mixing process was continued until dissolving all the quantity of the agar. The agar was poured into 2 cm glass tubes with a length of 22cm. The glass tubes were stored in a refrigerator for further use. The system is shown in Fig. 3.

Fig. 3. MFC double system and output voltage measurement

2.4. Chemical Oxygen Demand Measurements and Kinetics Modeling

The chemical oxygen demand for the bulgur industry wastewater was determined by closed reflux method (5220 C) (AWWA, WEF, APHA, 1998). The change in the COD was calculated by Equation 3.

$$COD\ remocal\ \% = \frac{COD\ i - COD\ f}{COD\ i} \times 100\% \qquad (3)$$

The COD data versus time were fitted to the zero order, first order, second order and third order kinetic reaction using the equations 4, 5, 6, and 7 respectively.

$$C_A = C_O - K_O t \qquad (4)$$

$$C_A = C_O e^{-k_1 t} \qquad (5)$$

$$\frac{1}{C_A} = \frac{1}{C_O} + K_2 t \qquad (6)$$

Where, C_A and C_O are the COD at the time t and the initial COD ($mg.L^{-1}$), t is the time, K is the reaction rate coefficient (day^{-1}).

The voltage was measured and recorded at least 2 times per day by GESI voltmeter as shown in Fig. 3.

3. RESULT AND DISCUSSION

3.1. Biomass Optimization

The biomass / wastewater percentage was optimized by comparing the generated biogas from the different percentages. The maximum volume of the biogas was generated when the biomass/wastewater was 3%. This results is within the range of (2-6%) which is proposed by with the range proposed by Tchobanoglous *et al*. (2003). Judeh (2017) obtained an optimum result at biomass/wastewater of 2.5%. Other studies found the optimum yield for the glucose-fed MFCs at range of (7 - 22%) (Rabaey *et al*., 2003). Erenler & Ülke (2018) used a biomass/wastewater percentage of 23. Table 1 shows the methane results.

Table 1. The generated biogas at different biomass percentages

Biomass Percentage (%)	biogas volume (mL)
2	2.5
3	2.6
4	1.7
5	1.3
10	1.7

3.2. COD Removal Efficiency

Many researchers had studied various types of food processing wastewater. In this study, the bulgur industry wastewater was treated by MFC method. Firstly, the chemical oxygen demand for the wastewater generated from the Bulgur industry was measured. It found to be 28800 mg/L. At the end of the experiment, the COD decreased to 2560 mg/L. Liu *et al*. (2014) used the MFC system to reduce the COD concentration of the starch processing wastewater from 1700 mg/L to 50 mg/L after a duration of 30 days. The efficiency of this technique reached 91%. The startup period extended to 15 days. At the 15th day the efficiency reached 40.5%. For the 10 days later the efficiency increased sharply to reach 83.3 %. After that, the maximum efficiency was reached and stilled constant. The measured COD and the removal efficiency curves are shown in Fig. 4.

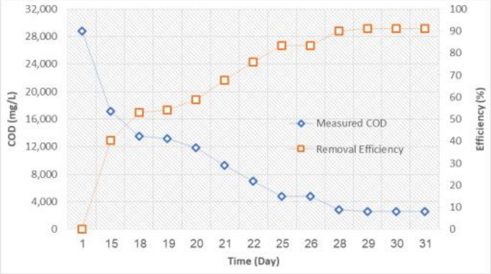

Fig. 4. The measured COD and the removal efficiency curves

The achieved COD removal efficiency in this study can be compared with other researches. Rodrigo *et al*. (2007) obtained A COD removal efficiency of 92% for urban wastewater. The COD removal of the Beet-sugar wastewater was in the range of (50%-70%) (Zhao et. al, 2013). MFC was successfully utilized to remove COD from dairy industry wastewater with %90 removal efficiency (Wang et. al, 2013).

3.3. COD Removal Kinetics

The equations from 4-7 were linearized. The K values were calculated and plotted versus the time. The correlation coefficients (R^2) for each model were noticed. Based on the coefficients for each model, the first order model is the most suitable one for the constructed MFC. Judeh (2017) investigate the degradation of the COD from municipal wastewater by MFC system and founded to be adequate to the first order. According to Ghaniyari-benis *et al*. (2010), the first order was good enough to describe the degradation of the organic matter using chambered hybrid anaerobic reactor. The zero, first, and second order models are shown in Figs. 5-7.

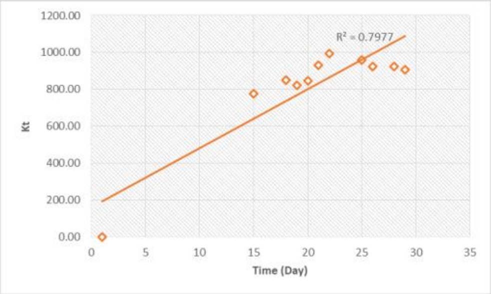

Fig. 5. Linearized Kt for zero order model vs time

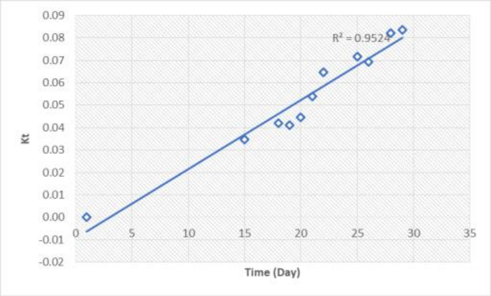

Fig. 6. Linearized Kt for first order model vs time

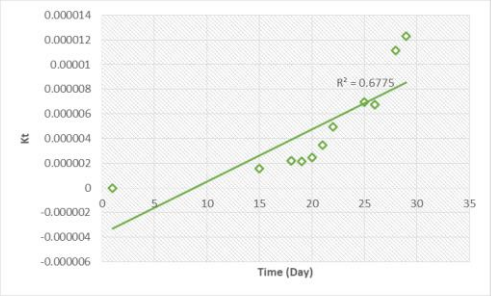

Fig. 7. Linearized Kt for second order model vs time

3.4. The Generated Voltage

The generated voltages were measured and the results are shown in Fig. 8.

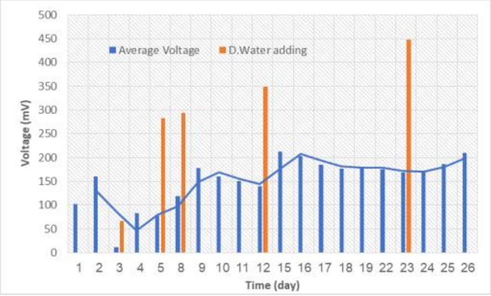

Fig. 8. The generated voltage over times

The maximum obtained voltage was 0.448 volt. The effect of changing of adding distilled water for the aerobic chamber. The voltage increased sharply when the new water added. The mean voltage was 0.180 volt. The average voltage per square meter was calculated by dividing the average voltage by the anode surface area. It reached 45 Volt/m^2. By comparing the voltage by other food wastewaters, the voltage generated in this study is larger than obtained from olive milling (0.38Volt) wastewater and the whey wastewater (0.41Volt) but not than molasses (0.54Volt) (Erenler &Ülke, 2018). The obtained voltage was affected by many variables. To acquire the optimum yield, so the system should be well optimized to have better results. After the optimization process, the obtained voltage can be used to partially cover the treatment energy.

4. CONCLUSION

In this study, the performance of treating bulgur industry wastewater by the MFC technique was assessed. The biomass / wastewater percentage was optimized by comparing the generated biogas from the different percentages. The maximum volume of the biogas was generated when the biomass/wastewater was 3%. The COD concentration was decreased from 28800 mg/L to 2560 mg/L with a removal efficiency of 91%. 1st order kinetic model had the best fit for COD removal with a correlation coefficient (R^2) of 0.95. The maximum and average voltages were 0.448 Volt and 0.180 Volt, respectively. The average voltage for every 1 m^2 was 45 volt. Even though the removal efficiency is high (91%), the MFC had not decreased the COD to the limits of the standard. The wastewater should be extra treated to reduce COD concentration. As a result of the exploratory study, the MFC can be used to treat the bulgur industry wastewater and generating energy. But it should be combined with other treatment methods to meet the standards.

Another note should be considered; this study is an exploratory study, so the system should be well optimized to have better results.

REFERENCES

Burkitt, R., Whiffen, T.R., Yu, E.H. (2016) “Iron phthalocyanine and MnOx composite catalysts for microbial fuel cell applications.” *Applied Catalysis B: Environmental*. Vol. 181, pp. 279–288.

Cheng, Y., Wang, L., Faustorilla, V., Megharaj, M., Naidu, R., Chen, Z. (2017). “Integrated electrochemical treatment systems for facilitating the bioremediation of oil spill contaminated soil.” *Chemosphere*. Vol. 175, pp. 294-299.

Closed Reflux, Titrimetric Method 5220 C (1998). *Standard Methods for the Examination of Water and Wastewater*. AWWA, WEF, APHA.

Du Z, Li H, Gu T. (2007) “A state of the art review on microbial fuel cells: a promising technology for wastewater treatment and bioenergy.” *Biotechnol Adv.* Vol. 25, pp. 464–82.

Dünya Gıda Dergisi. (2018). http://www.dunyagida.com.tr/haber/turkiye-dunyanin-en-buyuk-bulgur-ureticisi/8004. [Accessed 04 November 2019].

Erenler, A.Ş., & Ülke, E. N. (2018) “Mikrobiyal Yakıt Hücre Teknolojisini Kullanarak Gıda Endüstrisi Atıklarından Elektrik Enerjisi Üretimi.” *Batman University Journal of Life Sciences,* Vol. 8, Issue 2/2.

Ghaniyari-benis, S.; Martín, A.; Borja, R. (2010) “Kinetic modeling and performance prediction of a hybrid anaerobic baffled reactor treating synthetic wastewater at mesophilic temperature.” *Process Biochemistry,* Vol.45, p.1616-1623.

Gikas, P. and Tsoutsos, T. (2015), “Near Zero Energy Wastewater Treatment Plants for the Greek Islands”, *Desalination and Water Treatment*, Vol. 53, Iss. 12, pp. 3328-3324.

Gude, V.G. (2015). “Energy and water autarky of wastewater treatment and power generation systems.” *Renewable and sustainable energy review,* Vol. 45, pp. 52-68.

Habermann W, Pommer E. (1991) “Biological fuel cells with sulphide storage capacity.” *Appl Microbiol Biotechnol*; Vol. 35, pp.128–33.

He, L., Du, P., Chen, Y., Lu, H., Cheng, X., Chang, B., and Wang, Z. (2017). “Advances in microbial fuel cells for wastewater treatment.” *Renewable and Sustainable Energy Reviews*. Vol. 71, pp. 388–403. https://doi.org/10.1016/j.rser.2016.12.069.

Hisham, N.S., Zain, S.M., Joush, S., Anuar, N., Suja, F., Ismail, A., and Basri, N.E. (2013). “Microbial fuel cell using different types of wastewater for electricity generation and simultaneously removed pollutant.” *International of engineering science and technology*. Vol. 8(3), pp. 316-325.

Huggins, H., Fallgren, P.H., Jin, S., Ren, Z.J. (2013) “Energy and performance comparison of Microbial fuel cell.” *Journal of microbial and biochemical technology*. S6. DOI: 10.4172/1948-5948.S6-002.

Judeh, O. (2017). Feasibility of generating renewable energy from wastewater treatment process using microbial fuel cell: the West Bank as case study. MSc Thesis, An-Najah National University, Nablus, Palestine.

Köroğlu, E. O., Özkaya, B. and Çetinkaya, A.Y. (2014). “Microbial fuel cells for energy recovery from waste.” *Internationa journal of energy science*. Vol. 4(1). Pp.28-30.

Lee, C.Y., Ho, K.L., Lee, D.J., Su, A. and Chang, J.S. (2012) “Electricity harvest from wastewater using microbial.” *International journal of hydrogen energy*. Vol. 37(20). pp. 15787-15791.

Li, W.W., Yu, H.G. and He, Z. (2014). “Towards sustainable wastewater treatment by using microbial fuel cells-centered technologies.” *Energy Environ. Sci.*, Vol. 7, 911.

Liu ST, Song HL, Wei S, Yang F, Li XN. (2014) “Bio-cathode materials evaluation and configuration optimization for power output of vertical subsurface flow constructed wetland - Microbial fuel cell systems.” *Bioresour Technol.* Vol.166, pp.575–83.

Mise, S.R. and Saware, S. (2016). “Elecricity generation using textile wastewater by single chambered microbial fuel cell.” *International research journal of engineering and technology.* Vol. 3, pp. 710-716.

Mohan, S. V., Saravanan, R., Raghavulu, S. V., Mohanakrishna, G., and Sarma, P. (2007) “ Bioelectricity production from wastewater treatment on dual chambered microbial fuel cell (MFC) using selectively enriched mixed microflora: effect of catholyte. ” *Bioresource*

Technology. Vol. 99(3), pp. 596-603.

Rabaey, K., Lissens, G., Siciliano, S.D. *et al*. (2003) "A microbial fuel cell capable of converting glucose to electricity at high rate and efficiency." *Biotechnology Letters*. Vol. 25, pp. 1531–1535. https://doi.org/10.1023/A:1025484009367

Rodrigo, M.A., Cañizares, P., Lobato, J., Paz, R., Sáez, C., Linares, J.J. (2007) "Production of electricity from the treatment of urban waste water using a microbial fuel cell." *J Power Sources*. Vol.169, pp. 198–204.

Tchobanoglous, G.; Franklin, L. B.; Stensel, H. D. (2003). *Wastewater Engineering Treatment and Reuse*. McGraw-Hall, New York, USA.

Templeton, M.; Butler, D. (2011). *An Introduction to Wastewater Treatment*. Ventus Publishing ApS, London, UK.

Wang, Y.K., Sheng, G.P., Shi, B.J., Li, W.W., Yu, H.Q. (2013) "A novel electrochemical membrane bioreactor as a potential net energy producer for sustainable wastewater treatment." *Sci Rep-UK*, Vol. 3.

Zhao, Y.Q., Collum, S., Phelan, M., Goodbody, T., Doherty, L., Hua, Y.S. (2013) "Preliminary investigation of constructed wetland incorporating microbial fuel cell: batch and continuous flow trials." *Chem Eng J*, Vol. 229, pp. 364–70.

Turkish Journal of Engineering

Turkish Journal of Engineering (TUJE)
Vol. 4, Issue 4, pp. 209-217, October 2020
ISSN 2587-1366, Turkey
DOI: 10.31127/tuje.648882
Research Article

EFFECTIVE ADSORPTION OF TETRACYCLINE WITH Co_3O_4/Fe_3O_4 BIMETALLIC NANOPARTICLES

Muhammed Musa [1], Hatice Hasan [1], Hülya Malkoç [1], Memduha Ergüt *[1], Deniz Uzunoğlu [1] and Ayla Özer [1]

[1] Mersin University, Engineering Faculty, Department of Chemical Engineering, Mersin, Turkey
ORCID ID 0000 – 0002 – 8646 – 8354
mihemedmousa@gmail.com

[1] Mersin University, Engineering Faculty, Department of Chemical Engineering, Mersin, Turkey
ORCID ID 0000 – 0002 – 4643 – 1282
haticehasan97@hotmail.com

[1] Mersin University, Engineering Faculty, Department of Chemical Engineering, Mersin, Turkey
ORCID ID 0000 – 0003 – 0572 – 6727
hulyajt@gmail.com

[1] Mersin University, Engineering Faculty, Department of Chemical Engineering, Mersin, Turkey
ORCID ID 0000 – 0001 – 7297 – 1533
memduha.ergut@gmail.com

[1] Mersin University, Engineering Faculty, Department of Chemical Engineering, Mersin, Turkey
ORCID ID 0000 – 0001 – 9706 – 303X
duzunoglu@mersin.edu.tr

[1] Mersin University, Engineering Faculty, Department of Chemical Engineering, Mersin, Turkey
ORCID ID 0000 – 0002 – 7824 – 238X
ayozer@mersin.edu.tr

---

* Corresponding Author
Received: 20/11/2019 Accepted: 31/01/2020

ABSTRACT

In the present study cobalt oxide/iron oxide bimetallic nanoparticles (Co_3O_4/Fe_3O_4 NPs) were synthesized by chemical co-precipitation method. The synthesized Co_3O_4/Fe_3O_4 NPs were characterized by SEM and XRD analysis. The synthesized nanoparticles were used as an adsorbent for the removal of a kind of antibiotic as Tetracycline (TC) from aqueous solutions. According to characterization results, small plate-like structures and agglomerated irregular spherical nanosized particles (101.85 ± 15.04 nm) were formed. The XRD data confirmed the structure of synthesized adsorbent was Co_3O_4/Fe_3O_4. The optimum tetracycline adsorption conditions were determined as the initial pH of solution 9.0, temperature 55°C, and adsorbent concentration 3.0 g/L. A linear increase was observed in equilibrium uptakes of TC with the increasing the initial antibiotic concentrations. The experimental equilibrium data was modelled with Langmuir and Freundlich isotherm models. The experimental equilibrium data was the best agreement to the Langmuir isotherm model. The maximum monolayer coverage capacity of Co_3O_4/Fe_3O_4 NPs for TC adsorption was found to be 149.26 mg/g at 55°C optimum temperature. The experimental kinetic adsorption data were defined as the best agreement with the pseudo-second-order kinetic model. Weber Morris mass transfer modelling results showed that both the film (boundary layer) and intra-particle diffusion were effective in the adsorption process. The thermodynamic studies suggested that the adsorption process was endothermic, spontaneous and the positive ΔS value indicated increased disorder at the solid-solution interface during the adsorption. Moreover, the synthesized adsorbent showed high adsorption efficiencies at the end of seven sequence usages.

Keywords: *Adsorption, Bimetallic Nanoparticles, Cobalt Oxide, Iron Oxide, Tetracycline Removal*

1. INTRODUCTION

Antibiotics a kind of significant pharmaceutical ingredient, have been used for many decades as both human and veterinary medicines (Cao *et al.,* 2018).

Tetracycline (TC, $C_{22}H_{24}N_2O_8$) is the second most widely used antibiotics family in the world. TCs are often used in human therapy and livestock industry due to their broad-spectrum antimicrobial activity against a variety of pathogens (Erşan *et al.,* 2013; Bao *et al.,* 2013).

However, nowadays, the presence of antibiotics in the environment and their potential threat to human health and aquatic ecology has led to great concerns. Because antibiotics taken by humans and animals are not completely absorbed in the body. It has been suggested that about 90% of an administrated dose of antibiotic may be excreted through urine and feces (Turku *et al.,* 2007). In addition, the removal of these drug residues reaching sewage treatment plants cannot be fully achieved due to their resistance to biological degradation. Therefore, antibiotic residues can easily mix with surface and ground waters. They also pose a risk for ecological and aquatic environments due to their toxic effects and long half-life (Zhao *et al.,* 2011; Güler, 2016).

It has been reported that the antibiotics concentrations in untreated domestic wastewater range between 100 ng/L and 6 μg/L, while the concentrations in pharmaceutical and hospital wastewater can reach up to 100–500 mg/L (Cao *et al.,* 2018).

Therefore, the treatment of wastewater containing antibiotic residues with high organic load is one of the important environmental problems. So, it is necessary to develop inexpensive and efficient treatment methods for this purpose.

The oxidation methods, membrane filtration, reverse osmosis, ultrafiltration, Fenton process, and adsorption are applied as alternative treatment methods for the removal of antibiotics from wastewaters. Adsorption is commonly believed the easiest and cheapest one among these techniques.

Graphene oxide (Gao *et al.,* 2012), carbon nanotubes (Ji *et al.,* 2010), silica (Turku *et al.,* 2007), kaolinite (Li *et al.,* 2010), goethite (Zhao *et al.,* 2011), clay mineral illite (Chang *et al.,* 2012), montmorillonite (Parolo *et al.,* 2008); biosorbents such as maize stalks (Balarak *et al.,* 2016), *Pachydictyon coriaceum* and *Sargassumhemiphyllum* (Li *et al.,* 2015); activated carbon (Martins *et al.,* 2015), chitosan (Kang *et al.,* 2010); composite materials such as Fe_3O_4@SiO_2-Chitosan/graphene oxide nanocomposite (Huang *et al.,* 2017), Heteropolyacid–chitosan/TiO_2 composites (Yu *et al.,* 2014); nanomaterials such as Co-doped UiO-66 nanoparticle (Cao *et al.,* 2018) and Fe/Ni bimetallic nanoparticles (Dong *et al.,* 2018), and cobalt ferrite nanoparticles (Zhao *et al.,* 2014) were used as adsorbents for the removal of TC.

The aim of this work synthesis and characterization of bimetallic Co_3O_4/Fe_3O_4 NPs and investigate the adsorption of TC on Co_3O_4/Fe_3O_4 NPs. In this study, the experimental parameters that affect the adsorption of TC on Co_3O_4/Fe_3O_4 NPs such as initial pH of the solution, adsorbent concentration, initial TC concentration, and temperature were optimized to obtain maximum TC removal yield and also, the reusability of adsorbent was tested. The thermodynamic, equilibrium, kinetic, and mass transfer modeling studies were also carried out to evaluate the adsorption process.

2. MATERIALS AND METHODS

2.1. Materials

All of the chemicals were of analytical grade and they were used without further purification. For the synthesis of Co_3O_4/Fe_3O_4 bimetallic nanoparticles, $Fe(NO_3)_2.9H_2O$ and $Co(NO_3)_2.6H_2O$ were supplied from Across. Tetracycline hydrochloride ($C_{22}H_{24}N_2O_8.HCl$) was purchased from Sigma Aldrich. The chemical structure of TC antibiotics was presented in Fig. 1.

A stock solution of 250 mg/L of Tetracycline (TC) was first prepared and then the desired antibiotic concentrations were prepared by appropriate dilutions from the stock solution. The initial pHs of the solutions was adjusted with 0.1 N hydrochloric acid and/or 0.1 N sodium hydroxide.

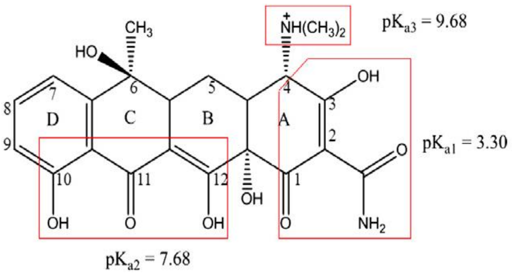

Fig.1. The structure of tetracycline, the framed regions represents the structural moieties associated with the three acidic dissociation constants (pKa).

2.2. Synthesis and Characterization of Co_3O_4/Fe_3O_4 NPs

The synthesis of Co_3O_4/Fe_3O_4 bimetallic nanoparticles (Co_3O_4/Fe_3O_4 NPs) was carried out by the chemical co-precipitation method. In the experiments, 25 mL of 0.1 M $Fe(NO_3)_2.9H_2O$ and 25 mL of 0.2 M $Co(NO_3)_2.6H_2O$ solution were mixed at room temperature for 15 min. Then 1.0 M sodium hydroxide solution was slowly added to the prepared solution. This mixture constantly stirred until the pH of 11.0 was reached. The changing of the color of the salt solution to intense black indicated the formation of Co_3O_4/Fe_3O_4 NPs. The obtained final mixture was kept under vigorous stirring for 3 h at 90°C. The formed nanoparticles were separated by centrifugation and then collected nanoparticles were washed several times with deionized water and dried in an oven at 105°C overnight.

The morphology of the Co_3O_4/Fe_3O_4 NPs was analyzed by Scanning Electron Microscope (SEM) analysis with Zeiss/Supra 55 SEM and the crystal structure was determined by X-ray Powder Diffraction (XRD) analysis, using nickel-filtered Cu Kα radiation in a Philips XPert MPD apparatus operated at 40 kV and 30 mA, in the 2θ range of 10°–90°.

2.3. Adsorption Studies

The batch adsorption experiments were carried out in 250 mL Erlenmeyer flasks containing 100 mL of TC antibiotic solution. 0.1 g of adsorbent, except for adsorbent concentration experiments, was contacted with 100 mL of TC solution at known initial antibiotic concentration and initial pH of solutions. Then the flasks were agitated at a constant temperature and shaking rate. Samples were taken before mixing the Co_3O_4/Fe_3O_4 NPs and TC solution and at pre-determined time intervals for the unadsorbed antibiotic concentration in the solution. Samples were centrifuged and the supernatant liquid was analyzed by UV-vis spectrophotometer at the wavelength of 360 nm.

The adsorbed amount of TC [q_e; (mg/g)] and the percentage of adsorption [Adsorption (%)] at equilibrium were calculated with Eqs. (1) and (2) as presented follows:

$$q_e\ (\text{mg/g}) = \frac{C_0 - C_e}{m} \cdot V \qquad (1)$$

$$\text{Adsorption (\%)} = \left[\frac{(C_0 - C_e)}{C_0}\right] \cdot 100 \qquad (2)$$

Where C_o (mg/L) and C_e (mg/L) are the initial and equilibrium concentrations of TC solution, respectively; and m(g) is the mass of adsorbent, and V(L) is the volume of the liquid phase.

3. RESULTS AND DISCUSSIONS

3.1. The Characterization of Co_3O_4/Fe_3O_4 NPs

The morphology of Co_3O_4/Fe_3O_4 NPs before and after adsorption was determined by SEM analysis and SEM images obtained at different magnifications were presented in Fig. 2. (a – d). SEM images of the synthesized Co_3O_4/Fe_3O_4 NPs (Fig. 2 (a, b)) showed that highly clustered surfaces, and agglomerated irregular spherical particles were formed. The SEM images obtained after the adsorption process showed that the morphology of Co_3O_4/Fe_3O_4 NPs changed a bit slightly; the clustered surfaces were disappeared, and the nanosized, spherical, and agglomerated particles became more apparent.

The mean particle size of the synthesized Co_3O_4/Fe_3O_4 NPs was calculated by using the modified form of the Williamson–Hall method, as presented following Eq. (3):

$$\beta\cos(\theta) = k\lambda/D + 4\varepsilon\sin(\theta) \qquad (3)$$

Where 'λ' is the wavelength of X-Ray (0.1541 nm), 'β' is FWHM (full width at half maximum), 'θ' is the diffraction angle, Ɛ is the strain, k is shape factor (0.9) and 'D' is mean particle diameter size.

The strain and particle size are calculated from the slope and y-intercept (kλ/D) of Williamson–Hall plot, i.e. the plot of between 4sin(θ) and βcos(θ). The slope of the graph gives strain and the intercept on the βcos(θ) axis gives the mean particle size corresponding to zero strain (Mote *et al.*, 2012). The mean particle size of Co_3O_4/Fe_3O_4 NPs was calculated to be 57.75 nm by using the Williamson–Hall method.

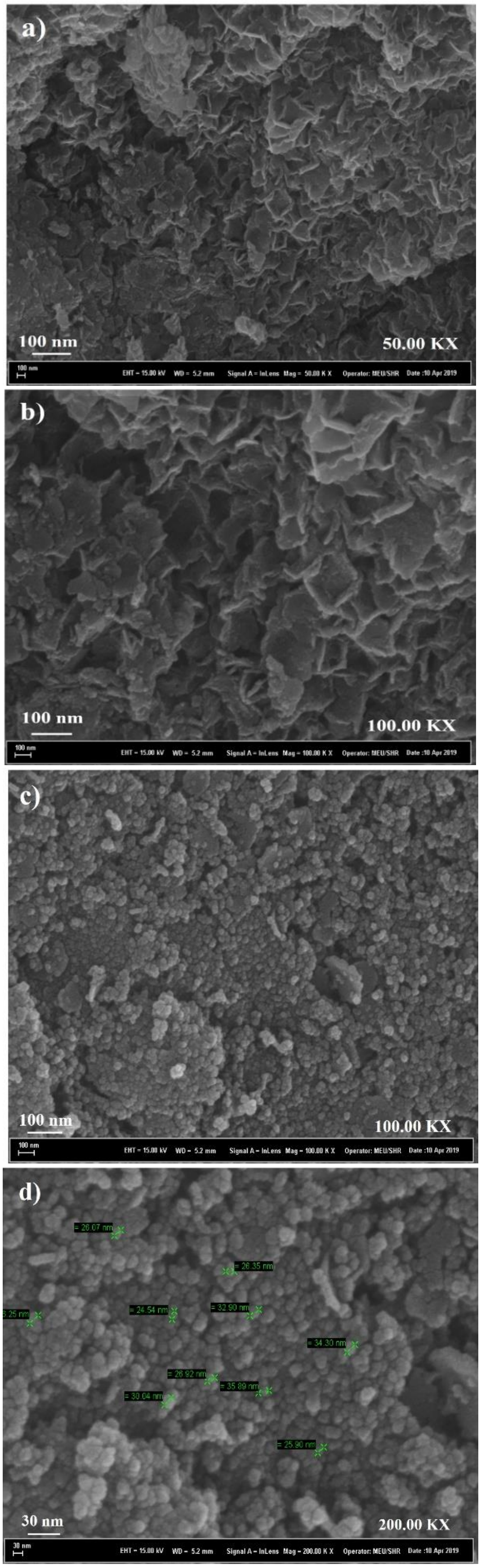

Fig.2. SEM images obtained at different magnifications before a) 50 KX, b)1000 KX; after c) 100 KX, d) 200 KX.

The mean particle size of the spherical particles was determined as 101.85 ± 15.04 nm by using the Image J program utilizing randomly selected particles from SEM images after the adsorption process.

The larger mean particle size of the Co_3O_4/Fe_3O_4 NPs was obtained from the SEM images than that obtained from XRD data. The reason for this result may be due to the fact that the SEM images indicate the size of polycrystalline particles which show the tendency to agglomerate due to their high surface energy.

The XRD pattern of synthesized Co_3O_4/Fe_3O_4 NPs was presented in Fig. 3.

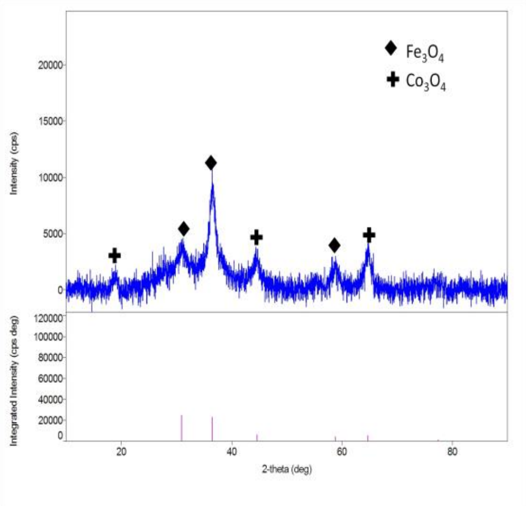

Fig.3. XRD diagram of synthesized Co_3O_4/Fe_3O_4 NPs

The peaks at 2θ = 30.91°, 36.46°, and 58.83° correspond to Fe_3O_4 and the peaks at 2θ = 19.02°, and 44.59°, and 64.46° showed the Co_3O_4 phase (Manigandan *et al.,* 2013).

3.2. Effects of Environmental Conditions on the Adsorption

3.2.1. Effect of initial pH

The initial pH is one of the most important parameters affecting the adsorption of TC on the active adsorbent surface. The interaction between the TC molecules and the adsorbent is mainly dependent on the TC species and variation of the surface loading of the adsorbent.

The isoelectric point (pH_{IEP}) of Co_3O_4/Fe_3O_4 NPs was determined by solid addition method at different pH (3.0 - 12) values (Uzunoğlu *et al.,* 2016). The variation of the isoelectric point with pH was presented in Fig. 4.

TC molecules are very sensitive to the initial pH of the solution due to their protonation status. As shown in Fig. 4, the isoelectric point at which the surface electrical charge of Co_3O_4/Fe_3O_4 NPs changes from negative to positive value was found to be pH 8.47.

Accordingly, the surface of Co_3O_4/Fe_3O_4 NPs was charged negatively below pH 8.47 and positively charged above this pH value. However; the structure of TC contains many polar and ionizable groups, including amino, carboxyl, phenol, alcohol, and ketone. The TC molecules can be present in three forms, cationic (pH<3.3), zwitterionic (3.3<pH<7.7) and anionic (pH>7.7) in aqueous solutions at different pH values (Roca Jalil *et al.,* 2018). In this case, there is an electrostatic interaction depending on the initial pH values in the adsorption of TC on Co_3O_4/Fe_3O_4 NPs surface. The effect of initial pH on the adsorption of TC to Co_3O_4/Fe_3O_4 NPs was given in Fig. 5.

As shown in Figure 5, the highest adsorption capacity was obtained at the initial pH: 9.0. At pH: 9.0, the TC molecules are in anionic form, while the adsorbent surface is positively charged. Therefore, the amount of TC adsorbed is the highest due to the increased electrostatic attraction between the TC molecules and the adsorbent surface at pH: 9.0.

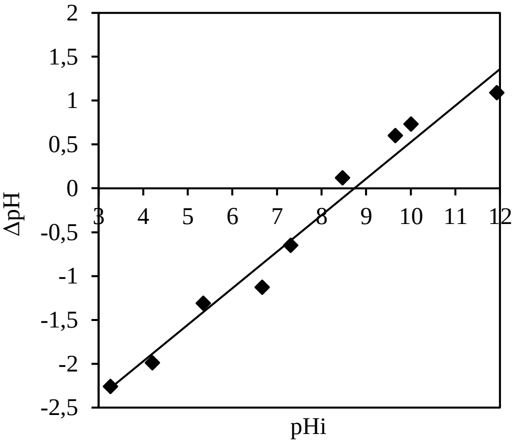

Fig.4. The isoelectric point of Co_3O_4/Fe_3O_4 NPs

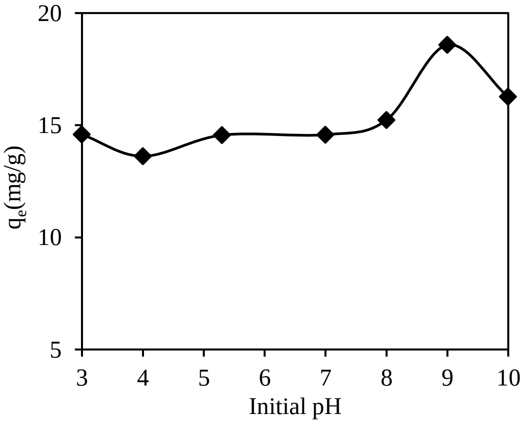

Fig.5. Effect of initial pH on the adsorption of TC (C_o=50 mg/L; X_o=1.0 g/L; T=25 °C; t= 420 min)

3.2.2. Effect of initial TC concentration

The effect of initial antibiotic concentration on adsorption was depicted in Fig. 6. As can be seen from Fig. 6, the adsorption capacities increased linearly ($q_e=0.3047*C_o$, $R^2=0.999$) in the studied TC concentrations as a result of the increase in the driving force (ΔC) to get over mass transfer resistances of the pollutant between the aqueous and solid phases.

3.2.3. Effect of adsorbent concentration

The adsorbent concentration effect on the equilibrium uptake was presented in Fig.7. According to Fig. 7, a decrease was observed in adsorption capacity by increasing the adsorbent concentration from 0.5 g/L to 3.0 g/L. However, the adsorption percentages increased by increasing the adsorbent concentration values. Therefore, although the highest adsorption capacity for tetracycline antibiotic was obtained at 0.5 g/L of adsorbent concentration, the optimum adsorbent concentration was determined as 3.0 g/L, since the highest removal yield was obtained at this adsorbent concentration value.

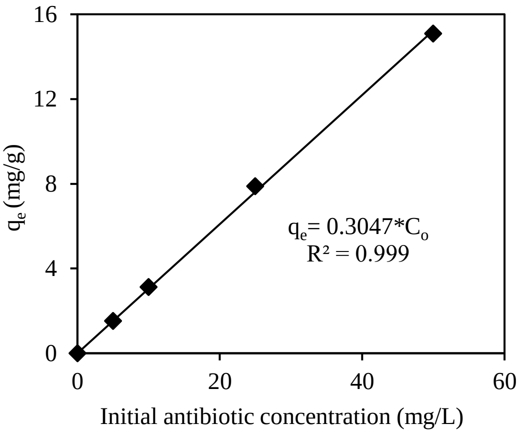

Fig.6. Effect of initial antibiotic concentration on the adsorption of TC (pH=9.0; Xo=3.0 g/L; T=50 °C; t=420 min)

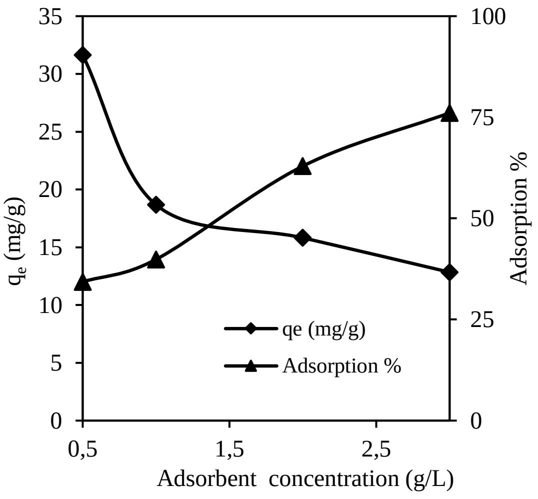

Fig.7. Effect of adsorbent concentration on the adsorption of TC (Co=50 mg/L, pH=9.0; T=25 °C; t=420 min)

3.2.4. Effect of temperature

The effect of temperature was presented in Fig. 8. According to Fig. 8, the increase in temperature has a positive effect on the adsorption of TC. The obtained adsorption capacities were increased with the increase in temperature from 25°C to 65°C. This result indicated that the studied adsorption process was endothermic nature.

Also, it was observed that when the temperature was increased from 55°C to 65°C, a slight change was obtained on adsorption capacity. So, the adsorption capacities approximately became constantly after 55°C. Therefore, the optimum temperature value for TC adsorption was determined to be 55°C.

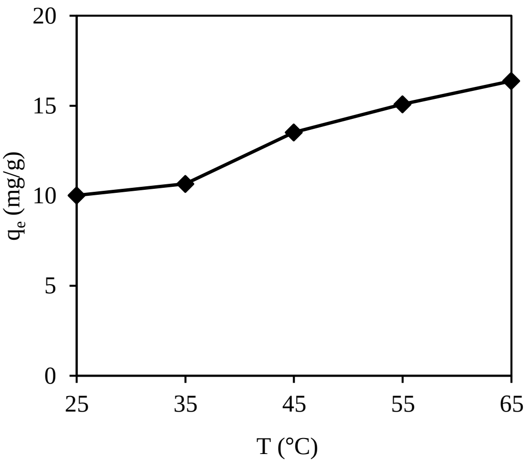

Fig. 8. Effect of temperature on the adsorption of TC (Co= 50 mg/L, pH=9.0; Xo=3.0 g/L; t=420 min)

3.3. Thermodynamic Parameters

The temperature effect was also confirmed with thermodynamic studies by calculating the entropy change (ΔS), enthalpy change (ΔH), and Gibbs energy change (ΔG). ΔH and ΔS were calculated from the slope and intercept of the linear plot of ln K_c versus 1/T according to Van't Hoff equation (Eq. 4), while ΔG was calculated according to Eq. 5.

$$\ln K_c = \left(\frac{\Delta S}{R}\right) - \left(\frac{\Delta H}{R}\right) \cdot \frac{1}{T} \qquad (4)$$

$$\Delta G = -RT \ln Kc = \Delta H - T\Delta S \qquad (5)$$

In this study, the linear form of Van't Hoff equation for the adsorption of TC onto Co_3O_4/Fe_3O_4 NPs was found as $\ln K_c = -8502.2 \times \frac{1}{T} + 28.569$ with the regression coefficient 0.993 (data not shown) and the thermodynamic parameters were calculated and presented in Table 1. According to Table 1, the calculated ΔG values had negative indicating that adsorption was spontaneous. The positive value of ΔS suggested that randomness of the adsorbed TC species at the solid-solution interface during adsorption and the studied adsorption systems were endothermic (ΔH>0).

Table 1. Thermodynamic parameters of adsorption

Thermodynamic parameters				
T (K)	*Kc*	*ΔH (kJ/mol)*	*ΔS (kJ/mol.K)*	*ΔG (kJ/mol)*
298	1.1132	70.68	0. 237	-0.265
318	5.6439			-4.575
328	12.824			-6.957
338	34.555			-9.955

3.4. The reusability of adsorbent

The operation cost is one of the important issues that need to be carefully considered. Therefore, operation cost can be significantly reduced owing to adsorbent reusability in practical applications. The reusability of the adsorbent was evaluated through seven recycled tests. The results regarding the TC adsorption efficiency for seven cycles of the adsorbent were given in Fig. 9. Between each cycle of use, the adsorbent was separated from the solution with Whatman #1 filter paper, washed several times with deionized water and then applied for the next experiment without any modifications. After each recycling test, the adsorption percentage of TC was determined. As seen in Fig. 9, the adsorption % of TC declined slightly from 99.43% in the first cycle to 88.42% after seven cycles of adsorption for 10 mg/L of TC solution. This result showed that the adsorbent can be recycled and reused for at least seven successive cycles without any significant loss of its efficiency.

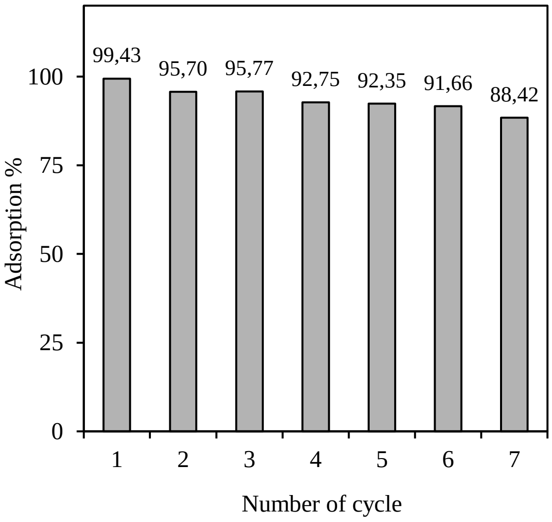

Fig. 9. Reusability of adsorbent within experimental runs for seven successive cycles (Co=10 mg/L, pH=9.0; Xo=3.0 g/L; t=420 min)

3.5. Equilibrium, Kinetic, and Mass Transfer Modelling

3.5.1. Equilibrium modeling

The well-known linearized forms of the Langmuir and Freundlich isotherm models were used to describe the adsorption equilibrium. The linearized forms of Langmuir and Freundlich isotherm models were given in Eqs. (6) and (7):

Langmuir: $$\frac{1}{q_e} = \frac{1}{Q^{\circ} b} \cdot \frac{1}{C_e} + \frac{1}{Q^{\circ}} \quad (6)$$

Freundlich: $$\ln q_e = \ln K_F + \left(\frac{1}{n}\right) \ln C_e \quad (7)$$

Langmuir isotherm model based on the assumption of maximum adsorption corresponds to a saturated monolayer of adsorbed molecules on the adsorbent surface with constant energy. Freundlich isotherm model suggests non-ideal sorption that involves heterogeneous surface energy systems (Malik, 2004).

The isotherm constants with regression coefficients (R^2) were presented in Table 2. Also, the experimental and predicted isotherms for adsorption at 55°C was given in Fig. 10.

According to Table 2 and Fig. 10, the Langmuir isotherm model was better fitted to experimental equilibrium data. This result showed that the adsorption occurred at specific homogeneous sites within the adsorbent forming monolayer coverage of TC at the surface of Co_3O_4/Fe_3O_4 NPs. The maximum monolayer coverage capacity of Co_3O_4/Fe_3O_4 NPs was determined as 149.26 mg/g at 55°C which is the optimum temperature. Moreover, as seen in Table 2, the maximum monolayer coverage capacity values of the adsorbent for TC increased by increasing temperature may be due to the endothermic nature of the studied adsorption process. The comparison of Q^o values of various types of adsorbents for TC adsorption was presented in Table 3.

Accordingly, it was seen that the adsorption capacity of Co_3O_4/Fe_3O_4 NPs was comparable with other adsorbents reported in earlier studies.

Table 2. The constants of the adsorption isotherm models with regression coefficients (pH=9.0; Xo=3.0 g/L; t=420 min)

T (°C)	**Langmuir isotherm model**			**Freundlich isotherm model**		
	Q^o (mg/g)	b (L/mg)	R^2	K_F (mg/g)/(L/mg)1/n)	1/n	R^2
25	21.053	0.03536	0.999	1.0114	0.6988	0.995
35	55.249	0.01745	0.998	1.0443	0.8627	0.991
45	135.135	0.01380	0.997	1.9397	0.8699	0.979
55	149.254	0.01020	0.999	1.4745	1.0089	0.994

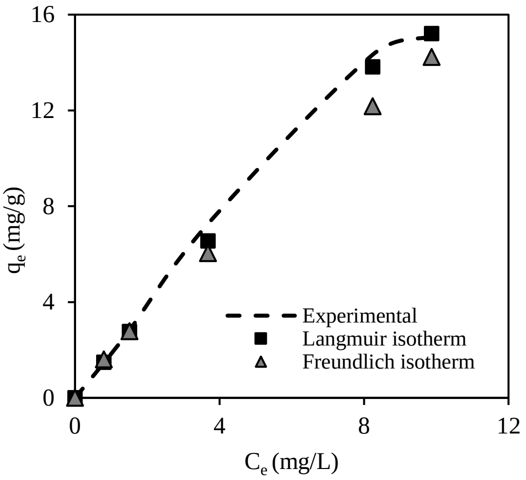

Fig.10. The comparison of the experimental and predicted isotherms

Table 3. The maximum monolayer adsorption capacity values (Q°) of various types of adsorbents in the literature

Adsorbent	Q° (mg/g)	Reference
Fe_3O_4@SiO_2-Chitosan/GO	151.4	(Huang *et al.,* 2017)
NH_2-MIL 101(Cr)	14	(Tian *et al.,* 2016)
Zn-AC	51.65	(Takdaştan *et al.,* 2016)
Cu_2O-TiO_2-Pal	113.6	(Shi *et al.,* 2016)
$GBCM_{350}$ activated carbon	58.2	(Álvarez-Torrellas *et al.,* 2016)
Co_3O_4/Fe_3O_4 NPs	149.25	This study

3.5.2. Kinetic modeling

The adsorption kinetics was elucidated by correlating the adsorption kinetic data using the linear forms of the Lagergen's pseudo-first-order and the pseudo-second-order kinetic models. The linearized forms of pseudo-first-order and the pseudo-second-order kinetic models were given in Eqs. (8) and (9), respectively (Mall *et al.,* 2007):

Pseudo first order: $\log (q_e - q_t) = \log (q_e) - \frac{k_1 t}{2.303}$ (8)

Pseudo second order : $\frac{t}{q_t} = (\frac{1}{q_e^2 k_2}) + \frac{t}{q_e}$ (9)

For the adsorption of TC onto Co_3O_4/Fe_3O_4 NPs, the parameters of the pseudo-first-order and pseudo-second-order kinetic models with regression coefficients were presented in Table 4. From Table 4, higher values of R^2 and the consistency between experimental and calculated uptake values showed a better agreement of the pseudo-second-order kinetics.

3.5.3. Effect of mass transfer

Weber-Morris model was used to determine the boundary layer and intra-particle diffusion mechanism between TC and adsorbent. Weber-Morris intraparticle diffusion model is expressed by the following Eq.(10) ;

$q_t = K_i . t^{0.5} + I$ (10)

In Weber-Morris equation; I is the intercept related to the boundary layer effect and K_i is the intraparticle diffusion rate constant which can be evaluated from the slope of the linear plots of qt versus $t^{0.5}$. According to this model, if the only intraparticle diffusion is the rate-controlling step in the adsorption process, the plot of uptake (q_e) versus the $t^{0.5}$ should be linear and these lines pass through the origin. On the other side, the Weber-Morris plot can be linear and also has an intercept value if the adsorption system follows both intraparticle and film diffusion (Wu *et al.,* 2009). The model parameters and regression coefficients were summarized in Table 4. Based on the results, it was observed a multilinear plot (figure not shown) indicated that both intraparticle and film diffusion were effective on the adsorption. Moreover, according to Table 4; it was seen that the internal (Ki) and external diffusion constants (I) gradually increased with increasing initial contaminant concentration.

Table 4. Kinetic and intra-particle mass transfer model parameters (pH=9.0, Xo=3g/L, t=420 min)

Co (mg/L)	qe, exp (mg/g)	Pseudo-first-order			Pseudo-second-order			Weber-Morris Model		
		k_1 (min^{-1})	*qe,cal_1 (mg/g)*	R^2	*k_2 (g/mg.min)*	*qe,cal_2 (mg/g)*	R^2	*Ki ($mg/g.min^{0.5}$)*	*I*	R^2
5	2.503	0.003685	2.3637	0.936	0.002233	2.749	0.970	0.0332	0.8925	0.995
10	3.163	0.004376	2.2014	0.960	0.004520	3.300	0.995	0.1009	0.9907	0.982
25	7.879	0.008521	7.3198	0.954	0.002852	8.453	0.991	0.3489	1.1454	0.990
50	15.086	0.005758	13.3967	0.919	0.00071	17.065	0.972	0.563	1.9738	0.998

4. CONCLUSION

In this study, Co_3O_4/Fe_3O_4 NPs were synthesized by the co-precipitation method for the removal of TC which is a kind of antibiotic from the aqueous solutions. The characterization studies of Co_3O_4/Fe_3O_4 NPs were carried out by SEM and XRD analysis. According to XRD results, the peaks were obtained correspond to Fe_3O_4 and Co_3O_4.

The adsorption was highly dependent on initial pH, adsorbent concentration, initial TC concentration, and temperature. The kinetics of TC adsorption on Co_3O_4/Fe_3O_4 NPs follows the pseudo-second-order model. The equilibrium data fitted well in the Langmuir model of adsorption, showing monolayer coverage of TC molecules at the outer surface of Co_3O_4/Fe_3O_4 NPs. The maximum monolayer coverage capacity of Co_3O_4/Fe_3O_4 NPs for TC adsorption determined to be 149.26 mg/g. Both intraparticle and film diffusion effects were determined on the adsorption process. Moreover, the adsorbent showed reusability at least seven sequence usages without loss of adsorbent property. The TC adsorption onto Co_3O_4/Fe_3O_4 NPs was found to be feasible and spontaneous from thermodynamic studies.

Consequently, these results provided the synthesis of an efficient adsorbent for the effective removal of antibiotic contaminants like tetracyclene in wastewater.

NOMENCLATURE

b : A constant related to the affinity of the binding sites (L/mg)
C_e : Unadsorbed Cr(VI) metal ion concentration at equilibrium (mg/L)
C_o : Initial Cr(VI) metal ion concentration (mg/L)
K_F : Freundlich constant indicating adsorption capacity ((mg/g)/(L/mg)$^{1/n}$)
K_i : Intraparticle diffusion rate constant (mg/g.min$^{0.5}$)
k_1 : Pseudo first order kinetic rate constant (1/min)
k_2 :Pseudo second order kinetic rate constant (g/mg.min)
q_e :Adsorbed amount per unit mass of adsorbent (mg/g)
q_{e,cal_1} :Calculated adsorbed amount per unit mass of adsorbent from pseudo first order kinetic model (mg/g)
q_{e,cal_2} :Calculated adsorbed amount per unit mass of adsorbent from pseudo second order kinetic model (mg/g)
$q_{e,exp}$:Experimental adsorbed amount per unit mass of adsorbent (mg/g)
q_t :Adsorbed amount per unit mass of adsorbent at any time (mg/g)
Q_o :Maximum monolayer coverage capacity of adsorbent (mg/g)
$1/n$: Freundlich constant indicating adsorption intensity

REFERENCES

Álvarez-Torrellas, S., Ribeiro, R. S., Gomes, H. T., Ovejero, G., & García, J. (2016). "Removal of antibiotic compounds by adsorption using glycerol-based carbon materials". *Chemical Engineering Journal*, Vol. 296, pp. 277-288.

Balarak, D., Mostafapour, F. K., & Azarpira, H. (2016). "Adsorption isotherm studies of tetracycline antibiotics from aqueous solutions by maize stalks as a cheap biosorbent." *International Journal of Pharmacy and Technology*, Vol. 8, No. 3, pp. 16664-16675.

Bao, X., Qiang, Z., Ling, W., & Chang, J. H. (2013). "Sonohydrothermal synthesis of MFe_2O_4 magnetic nanoparticles for adsorptive removal of tetracyclines from water." *Separation and Purification Technology*, Vol.117, pp.104-110.

Cao, J., Yang, Z. H., Xiong, W. P., Zhou, Y. Y., Peng, Y. R., Li, X., ... & Zhang, Y. R. (2018). "One-step synthesis of Co-doped UiO-66 nanoparticle with enhanced removal efficiency of tetracycline: Simultaneous adsorption and photocatalysis." *Chemical Engineering Journal*, Vol. 353, pp.126-137.

Chang, P. H., Li, Z., Jean, J. S., Jiang, W. T., Wang, C. J., & Lin, K. H. (2012). "Adsorption of tetracycline on 2: 1 layered non-swelling clay mineral illite." *Applied Clay Science*, Vol. 67, pp. 158-163.

Dong, H., Jiang, Z., Zhang, C., Deng, J., Hou, K., Cheng, Y., ... & Zeng, G. (2018). "Removal of tetracycline by Fe/Ni bimetallic nanoparticles in aqueous solution." *Journal of colloid and interface science*, Vol. 513, pp. 117-125.

Erşan, M., Bağda, E., & Bağda, E. (2013). "Investigation of kinetic and thermodynamic characteristics of removal of tetracycline with sponge like, tannin based cryogels." *Colloids and surfaces B: Biointerfaces*, Vol. 104, pp. 75-82.

Gao, Y., Li, Y., Zhang, L., Huang, H., Hu, J., Shah, S. M., & Su, X. (2012). "Adsorption and removal of tetracycline antibiotics from aqueous solution by graphene oxide." *Journal of colloid and interface science*, Vol. 368, No.1, pp.540-546.

Güler, Ü. A. (2016). "Aljinat-TiO_2-Alg Kompozitinin Sentezi ve Sulu Çözeltilerden Tetrasiklin Gideriminde Kullanılabilirliği ve Karakterizasyonu." *Karaelmas Science and Engineering Journal*, Vol. 6, No.1, pp. 130-135.

Huang, B., Liu, Y., Li, B., Liu, S., Zeng, G., Zeng, Z., ... & Yang, C. (2017). "Effect of Cu (II) ions on the enhancement of tetracycline adsorption by Fe_3O_4@SiO_2-Chitosan/graphen oxide nanocomposite." *Carbohydrate polymers*, Vol. 157, pp. 576-585.

Ji, L., Chen, W., Bi, J., Zheng, S., Xu, Z., Zhu, D., & Alvarez, P. J. (2010). "Adsorption of tetracycline on single-walled and multi-walled carbon nanotubes as affected by aqueous solution chemistry." *Environmental toxicology and chemistry*, Vol. 29, No. 12, pp. 2713-2719.

Kang, J., Liu, H., Zheng, Y. M., Qu, J., & Chen, J. P. (2010). "Systematic study of synergistic and antagonistic effects on adsorption of tetracycline and copper onto a chitosan." *Journal of Colloid and Interface Science,* Vol. 344, No.1, pp.117-125.

Li, W. C., & Wong, M. H. (2015). "A comparative study on tetracycline sorption by Pachydictyon coriaceum and Sargassumhemiphyllum." *International journal of environmental science and technology,* Vol. 12, No. 8, pp. 2731-2740.

Li, Z., Schulz, L., Ackley, C., & Fenske, N. (2010). "Adsorption of tetracycline on kaolinite with pH-dependent surface charges." *Journal of colloid and interface science,* Vol. *351,* No.1, pp. 254-260.

Malik, P. K. (2004). "Dye removal from wastewater using activated carbon developed from sawdust: adsorption equilibrium and kinetics." *Journal of Hazardous Materials,* Vol. 113, No.1-3, pp. 81-88.

Mall, I. D., Srivastava, V. C., & Agarwal, N. K. (2007). "Adsorptive removal of Auramine-O: Kinetic and equilibrium study." *Journal of Hazardous materials,* Vol. 143, No.(1-2), pp. 386-395.

Manigandan, R., Giribabu, K., Suresh, R., Vijayalakshmi, L., Stephen, A., & Narayanan, V. (2013). "Cobalt oxide nanoparticles: characterization and its electrocatalytic activity towards nitrobenzene." *Chemical Science Transactions,* Vol. 2, No.1, pp. 47-S50.

Martins, A. C., Pezoti, O., Cazetta, A. L., Bedin, K. C., Yamazaki, D. A., Bandoch, G. F.,& Almeida, V. C. (2015). "Removal of tetracycline by NaOH-activated carbon produced from macadamia nut shells: kinetic and equilibrium studies." *Chemical Engineering Journal,* Vol. 260, pp. 291-299.

Mote, V. D., Purushotham, Y., & Dole, B. N. (2012). "Williamson-Hall analysis in estimation of lattice strain in nanometer-sized ZnO particles." *Journal of Theoretical and Applied Physics,* Vol.*6, No.*1, pp.6.

Parolo, M. E., Savini, M. C., Valles, J. M., Baschini, M. T., & Avena, M. J. (2008). "Tetracycline adsorption on montmorillonite: pH and ionic strength effects." *Applied Clay Science,* Vol. *40,* No. 1-4, pp.179-186.

Roca Jalil, M., Toschi, F., Baschini, M., & Sapag, K. (2018). "Silica Pillared Montmorillonites as Possible Adsorbents of Antibiotics from Water Media." *Applied Sciences,* Vol. 8, No. 8, pp.1403.

Shi, Y., Yang, Z., Wang, B., An, H., Chen, Z., & Cui, H. (2016). "Adsorption and photocatalytic degradation of tetracycline hydrochloride using a palygorskite-supported Cu_2O–TiO_2 composite." *Applied Clay Science,* Vol. 119, pp. 311-320.

Takdastan, A., Mahvi, A. H., Lima, E. C., Shirmardi, M., Babaei, A. A., Goudarzi, G., ... & Vosoughi, M. (2016). "Preparation, characterization, and application of activated carbon from low-cost material for the adsorption of tetracycline antibiotic from aqueous solutions." *Water Science and Technology,* Vol. *74,* No.10, pp. 2349-2363.

Tian, N., Jia, Q., Su, H., Zhi, Y., Ma, A., Wu, J., & Shan, S. (2016). "The synthesis of mesostructured NH 2-MIL-101 (Cr) and kinetic and thermodynamic study in tetracycline aqueous solutions." *Journal of Porous Materials,* Vol. *23,* No. 5, pp. 1269-1278.

Turku, I., Sainio, T., & Paatero, E. (2007). "Thermodynamics of tetracycline adsorption on silica." *Environmental Chemistry Letters,* Vol. *5,* No. 4, pp. 225-228.

Uzunoğlu, D., & Özer, A. (2016). "Adsorption of Acid Blue 121 dye on fish (Dicentrarchus labrax) scales, the extracted from fish scales and commercial hydroxyapatite: equilibrium, kinetic, thermodynamic, and characterization studies." *Desalination and Water Treatment,* Vol. 57, No. 30, pp.14109-14131.

Wu, F. C., Tseng, R. L., & Juang, R. S. (2009). "Initial behavior of intraparticle diffusion model used in the description of adsorption kinetics." *Chemical Engineering Journal,* Vol. 153, No. (1-3), pp.1-8.

Yu, X., Lu, Z., Wu, D., Yu, P., He, M., Chen, T., ... & Feng, Y. (2014). "Heteropolyacid–chitosan/TiO_2 composites for the degradation of tetracycline hydrochloride solution." *Reaction Kinetics, Mechanisms and Catalysis,* Vol.111, No. 1, pp. 347-360.

Zhao, X., Wang, W., Zhang, Y., Wu, S., Li, F., & Liu, J. P. (2014). "Synthesis and characterization of gadolinium doped cobalt ferrite nanoparticles with enhanced adsorption capability for Congo Red." *Chemical Engineering Journal,* Vol. 250, pp.164-174.

Zhao, Y., Geng, J., Wang, X., Gu, X., & Gao, S. (2011). "Adsorption of tetracycline onto goethite in the presence of metal cations and humic substances." *Journal of colloid and interface science,* Vol. 361 No. 1, pp. 247-251.

Turkish Journal of Engineering

Turkish Journal of Engineering (TUJE)
Vol. 4, Issue 4, pp. 218-225, October 2020
ISSN 2587-1366, Turkey
DOI: 10.31127/tuje.665156
Research Article

BUCKLING ANALYSIS OF LAMINATED COMPOSITE PLATES UNDER THE EFFECT OF UNIAXIAL AND BIAXIAL LOADS

Ali Dogan *[1]

[1] Iskenderun Technical University, Faculty of Engineering and Nature Science, Department of Civil Engineering, Iskenderun, Hatay, Turkey
ORCID ID 0000 – 0002 – 2825 – 8068
ali.dogan@iste.edu.tr

---

* Corresponding Author
Received: 27/12/2019 Accepted: 16/02/2020

ABSTRACT

This paper investigates the buckling analysis of simply supported symmetrically thin and thick composite plates. Using the Hamilton’s principle, the governing equation for thin and thick composite plates is derived. The equation of motion for thin and thick laminated rectangular plates subjected to in-plane loads is obtained with the help of Hamilton’s principle. The loading conditions of rectangular plate are uniaxial and biaxial compression. Considering the Navier solution technique, closed form solutions are attained and buckling loads are found by solving the eigenvalue problems. In this study, the effect of edge ratios and anisotropy on the buckling analysis of rectangular plate was investigated. The computer programs have been written separately with the help of Mathematica (MATHEMATICA 2017) program for the solution of the buckling analysis of laminated composite plates. Results of the numerical studies for the buckling of laminated composite plates (LCP) are demonstrated and benchmarked with former studies in the literature and ANSYS finite element methods.

Keywords*: Buckling Analysis, Laminated Composite Plate, Shear Deformation Theory, Finite Element Method (ANSYS).*

1. INTRODUCTION

Recently, due to the many paramount properties advanced composite materials such as laminated plates are found an application area in the engineering projects. Tremendous researches have been performed on the LCP to clarify the advantages of using these types of materials. One of the focused topics in research subject is the buckling analysis of the composite plates.

Reissner theory (1945) is one of the theories which include the shear deformation effect and many researchers have studied on the buckling analysis of LCP by using Reissner theory. Noor (1975) examined the stability and vibration analysis of the composite plates. Qatu used energy function to develop governing equations of LCP. Phan and Reddy (1985) are analyzed of laminated composite plates using a higher-order shear deformation theory. Reddy and Khdeir (1989) investigated buckling and vibration analysis of LCP. Some studies have been performed on characteristics of plates by Qatu (1991-2004) using different plate theories. Dogan et al. (2010) have analyzed the effects of anisotropy and curvature on vibration characteristics of laminated shallow shells using shear deformation theory. Dogan (2012) investigated the effect of dimension on mode-shapes of composite shells. Akavci (2007) presented buckling and free vibration analysis of symmetric and antisymmetric laminated composite plates on an elastic foundation. Akavci et al. (2007) examined buckling and free vibration behavior of LCP on elastic foundation by using first order shear deformation theory (FSDT). Functionally graded plates thermal buckling analysis have been investigated by Akavci (2014) using the theory of hyperbolic shear deformation. Phan and Reddy (1985) analyzed laminated composite plates by using a higher-order shear deformation theory. Setodehand Karami (2004) studied on buckling analysis of laminated composite plates of elastic foundation. Sophy (2013) studied buckling and free vibration of exponentially graded sandwich plates resting on elastic foundations under various boundary conditions. Dogan (2019) investigated buckling analysis of symmetric laminated composite thick plates. Sayyad and Ghuga (2014) presented a study about buckling and free vibration analysis of orthotropic plates by using exponential shear deformation theory.

In this research, buckling analysis of symmetric LCP are investigated using various of number of layers, plate edge ratio and anisotropy ratio. This study might be a pioneer work in terms of laminated composite plates and experimental studies.

2. EQUATIONS

A lamina is produced with the isotropic homogenous fibers and matrix materials (Fig. 1). Any point on a fiber, and/or on matrix and/or on matrix-fiber interface has crucial effect on the stiffness of the lamina. Due to the big variation on the properties of lamina from point to point, macro-mechanical properties of lamina are determined based on the statistical approach.

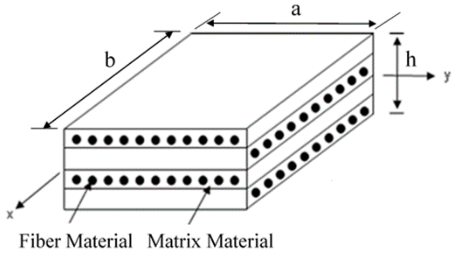

Fig. 1. Fiber and matrix materials in laminated composite plate

According to FSDT, the transverse normal does not cease perpendicular to the mid-surface after deformation. It will be assumed that the deformation of the plates is completely determined by the displacement of its middle surface. Using the given equation below (Eq.1) nth layer lamina plate stress-strain relationship can be defined in lamina coordinates (Qatu 2004).

$$\begin{bmatrix}\sigma_x\\ \sigma_y\\ \sigma_z\\ \tau_{yz}\\ \tau_{xz}\\ \tau_{xy}\end{bmatrix}=\begin{bmatrix}\overline{Q}_{11} & \overline{Q}_{12} & \overline{Q}_{13} & 0 & 0 & \overline{Q}_{16}\\ \overline{Q}_{12} & \overline{Q}_{22} & \overline{Q}_{23} & 0 & 0 & \overline{Q}_{26}\\ \overline{Q}_{16} & \overline{Q}_{26} & \overline{Q}_{33} & 0 & 0 & \overline{Q}_{36}\\ 0 & 0 & 0 & \overline{Q}_{44} & \overline{Q}_{45} & 0\\ 0 & 0 & 0 & \overline{Q}_{45} & \overline{Q}_{55} & 0\\ \overline{Q}_{16} & \overline{Q}_{26} & \overline{Q}_{36} & 0 & 0 & \overline{Q}_{66}\end{bmatrix}\begin{bmatrix}\varepsilon_x\\ \varepsilon_y\\ \varepsilon_z\\ \gamma_{yz}\\ \gamma_{xz}\\ \gamma_{xy}\end{bmatrix} \quad (1)$$

The displacement based on plate theory can be written as

$$\begin{aligned}&\mathrm{u(x,y,z,t)=u_0(x,y,t)+z}\,\varphi_x\,\mathrm{(x,y,t)}\\ &\mathrm{v(x,y,z,t)=v_0(x,y,t)+z}\,\varphi_y\,\mathrm{(x,y,t)}\\ &\mathrm{w(x,y,z,t)=w_0(x,y,t)}\end{aligned} \quad (2)$$

where u, v, w, φ_x and φ_y are displacements and rotations in x, y, z direction, orderly. u_o, v_o and w_o are mid-plane displacements.

Equation of motion for plate structures can be derived by Hamilton's principle

$$\delta\int_{t_1}^{t_2}(T+W-U)dt=0 \quad (3)$$

where T is the kinetic energy of the structure

$$T=\frac{\rho}{2}\int\left\{\left(\frac{\partial u}{\partial t}\right)^2+\left(\frac{\partial v}{\partial t}\right)^2+\left(\frac{\partial w}{\partial t}\right)^2\right\}dxdydz \quad (4)$$

W is the work of the external forces

$$W=\int_x\int_y(q_x u+q_y v+q_z w+m_x\psi_x+m_y\,\psi_y)dxdy \quad (5)$$

in which, q_x , q_y ,q_z ,m_x, m_y are the external forces and moments per unit length, respectively. U is the strain energy and defined as,

$$U=\frac{1}{2}\int\big(\sigma_x\varepsilon_x+\sigma_y\varepsilon_y+\sigma_z\varepsilon_z+\tau_{xy}\gamma_{xy}+\tau_{xz}\gamma_{xz}+\tau_{yz}\gamma_{yz}\big)dxdydz \quad (6)$$

Solving equation 3 gives set of equations called equations of motion for plate structures. This gives equation 7 in simplified form as,

$$\begin{aligned}
&\frac{\partial}{\partial x}N_x+\frac{\partial}{\partial y}N_{yx}+q_x=I_1\ddot{u}^2+I_2\ddot{\psi}_x^2\\
&\frac{\partial}{\partial y}N_y+\frac{\partial}{\partial x}N_{xy}+q_y=I_1\ddot{v}^2+I_2\ddot{\psi}_y^2 \qquad (7)\\
&\frac{\partial}{\partial x}Q_x+\frac{\partial}{\partial y}Q_y+q_z+k_0w+k_1\Delta^2w=I_1\ddot{w}^2\\
&\frac{\partial}{\partial x}M_x+\frac{\partial}{\partial y}M_{yx}-Q_x+m_x=I_2\ddot{u}^2+I_3\ddot{\psi}_x^2\\
&\frac{\partial}{\partial y}M_y+\frac{\partial}{\partial x}M_{xy}-Q_y+m_y=I_2\ddot{v}^2+I_3\ddot{\psi}_y^2
\end{aligned}$$

Equation 7 is defined as equation of motion for thick plates. Where I_1, I_2 and I_3 are mass moment inertia. Based on the FSDT plate, moment resultants are M_x, M_y and M_{xy}, in plane force resultants are N_x, N_y, N_{xy} and transverse shearing force resultants are Q_x and Q_y. The force and moment resultants are defined as

$$\begin{bmatrix} N_x\\ N_y\\ N_{xy}\\ M_x\\ M_y\\ M_{xy}\end{bmatrix}=\begin{bmatrix} A_{11} & A_{12} & A_{16} & B_{11} & B_{12} & B_{16}\\ A_{12} & A_{22} & A_{26} & B_{12} & B_{22} & B_{26}\\ A_{16} & A_{26} & A_{66} & B_{16} & B_{26} & B_{66}\\ B_{11} & B_{12} & B_{16} & D_{11} & D_{12} & D_{16}\\ B_{12} & B_{22} & B_{26} & D_{12} & D_{22} & D_{26}\\ B_{16} & B_{26} & B_{66} & D_{16} & D_{26} & D_{66}\end{bmatrix}\begin{bmatrix} \varepsilon_{0x}\\ \varepsilon_{0y}\\ \gamma_{0xy}\\ \kappa_x\\ \kappa_y\\ \tau\end{bmatrix} \qquad (8)$$

$$\begin{bmatrix} Q_x\\ Q_y\end{bmatrix}=\begin{bmatrix} A_{55} & A_{45}\\ A_{45} & A_{44}\end{bmatrix}\begin{bmatrix} \gamma_{0xz}\\ \gamma_{0yz}\end{bmatrix}$$

$$\begin{aligned}
&\{A_{ij},B_{ij},D_{ij}\}=\int_{-h/2}^{h/2}\{1,z,z^2\}\overline{Q}_{ij}\,dz \qquad i,j=1,2,6\\
&\{A_{ij}\}=K_S\int_{-h/2}^{h/2}\overline{Q}_{ij}\,dz \qquad i,j=4,5 \qquad (9)\\
&[I_1,I_2,I_3]=\int_{-h/2}^{h/2}\rho(1,z,z^2)\,dz
\end{aligned}$$

Where the parameter K_s is the shear correction factor. Here, K_s is taken as 5/6.

The Navier type solution might be implemented to thick and thin plates. This type solution assumes that the displacement section of the plates can be denoted as sine and cosine trigonometric functions. A plate with shear diaphragm boundaries on all edges is assumed. For simply supported thick plates, boundary conditions can be arranged as follows:

$$\begin{aligned}
&N_x=w_0=v_0=M_x=\psi_y=0 \qquad x=0,a\\
&N_y=w_0=u_0=M_y=\psi_x=0 \qquad y=0,b
\end{aligned} \qquad (10)$$

The displacement functions of the satisfied the boundary conditions are applied;

$$\begin{aligned}
&u_0(x,y,t)=\sum_{m=0}^{\infty}\sum_{n=0}^{\infty}U_{mn}\mathrm{Cos}(x_mx)\mathrm{Sin}(y_ny)\mathrm{Sin}(\omega_{mn}t)\\
&v_0(x,y,t)=\sum_{m=0}^{\infty}\sum_{n=0}^{\infty}V_{mn}\mathrm{Sin}(x_mx)\mathrm{Cos}(y_ny)\mathrm{Sin}(\omega_{mn}t)\\
&w_0(x,y,t)=\sum_{m=0}^{\infty}\sum_{n=0}^{\infty}W_{mn}\mathrm{Sin}(x_mx)\mathrm{Sin}(y_ny)\mathrm{Sin}(\omega_{mn}t) \qquad (11)\\
&\psi_x(x,y,t)=\sum_{m=0}^{\infty}\sum_{n=0}^{\infty}\psi_{xmn}\mathrm{Cos}(x_mx)\mathrm{Sin}(y_ny)\mathrm{Sin}(\omega_{mn}t)\\
&\psi_y(x,y,t)=\sum_{m=0}^{\infty}\sum_{n=0}^{\infty}\psi_{ymn}\mathrm{Sin}(x_mx)\mathrm{Cos}(y_ny)\mathrm{Sin}(\omega_{mn}t)
\end{aligned}$$

where $x_m=m\pi/a$, $y_n=n\pi/b$. and ω_{mn} is the naturel frequency. The loads are defined as,

$$q(x,y,t)=\sum_{m=1}^{\infty}\sum_{n=1}^{\infty}Q_{mn}(t)\,\mathrm{Sin}(x_mx)\mathrm{Cos}(y_ny) \qquad (12)$$

where

$$Q_{mn}(t)=\frac{4}{ab}\int_0^a\int_0^b q(x,y,t)\mathrm{Sin}(x_mx)\mathrm{Cos}(y_ny)\,dx\,dy \qquad (13)$$

Substituting the above equations into the equation of motion in matrix form,

$$[N]=\begin{bmatrix} 0 & 0 & 0 & 0 & 0\\ 0 & 0 & 0 & 0 & 0\\ 0 & 0 & \alpha^2\overline{N_x}+\beta^2\overline{N_y} & 0 & 0\\ 0 & 0 & 0 & 0 & 0\\ 0 & 0 & 0 & 0 & 0\end{bmatrix} \qquad (14)$$

$$[K]=\begin{bmatrix} K_{11} & K_{12} & K_{13} & K_{14} & K_{15}\\ K_{21} & K_{22} & K_{23} & K_{24} & K_{25}\\ K_{31} & K_{32} & K_{33} & K_{34} & K_{35}\\ K_{41} & K_{42} & K_{43} & K_{44} & K_{45}\\ K_{51} & K_{52} & K_{53} & K_{54} & K_{55}\end{bmatrix} \qquad (15)$$

$$[\Delta]=\begin{bmatrix} U_{mn}\\ V_{mn}\\ W_{mn}\\ \psi_{xmn}\\ \psi_{ymn}\end{bmatrix} \qquad (16)$$

Equation 12 can be arranged in a closed form as follows:

$$([K_{mn}]-\omega[N])\Delta=0 \qquad (17)$$

where [K_{mn}], stiffness matrices, [N] is buckling load.

3. NUMERICAL SOLUTIONS AND DISCUSSIONS

In current research, buckling analyses of symmetric LCP are investigated. Navier solution procedure for buckling analysis of LCP is obtained. The computer programs have been prepared using Mathematica program separately for the solution of the buckling analysis of LCP. The results were compared with the semi-analytical method and the ANSYS finite element software and previous studies in the literature. The effects of the E_1/E_2, and a/b ratio are also investigated.

In numerical calculations, the material and geometrical properties are defined as: a = 1m (a/b = 1, 2; a/h = 10, $\rho = 2000$ kg/m^3, $E_1 = 40\times10^3$ MPa (E_1/E_2 =3, 10, 20, 30, 40), G_{12}/E_2 = G13/E2 = 0.6, G_{23}/E_2 = 0.5, υ = 0.25. In the analysis, following parameter is studied for non-dimensional buckling load as;

$$\lambda=\overline{N}_x\frac{a^2}{E_2h^3} \qquad (18)$$

It can be seen from Tables 1 that the non-dimensional buckling load factors increase when the ratio of E_1/E_2 change from 3 to 40 (Fig. 3). The non-dimensional buckling load factors decrease when the ratio of a/b change from 1 to 2 for Table 2 and Fig 4-5. Also, the non-dimensional buckling load factors obtained for present study seem to be compatible with other study. Buckling analysis results showed that when the number of layer increases, the non-dimensional buckling load factors obtained by present study increase as well (Fig. 6-7).

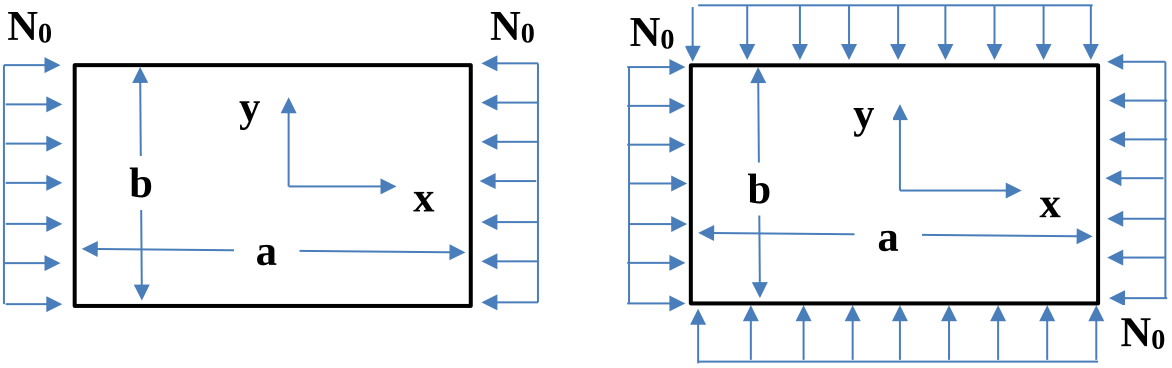

(a) Uniaxial compression along x-axis

(b) Biaxial compression

Fig. 2. The loading conditions of plate

Table 1. Unaxial non-dimensional buckling load factors of (0/90/90/0) laminate for different orthotropy ratios (a/b=1 and a/h=10)

	E_1/E_2				
Method	**3**	**10**	**20**	**30**	**40**
CLPT [Phan etc.]	5.7538	11.4920	19.7120	27.9360	36.1600
HSDT[Phan etc.]	5.1143	9.7740	15.2980	19.9570	23.3400
3DElasticity[Noor]	5.2944	9.7621	15.0191	19.3040	22.8807
ANSYS (FEM)	7.2290	11.2470	16.2720	19.4090	23.8800
Akavci	5.4192	10.0671	16.6358	19.3040	24.1601
Present Study	5.4550	10.0056	15.3828	19.7824	23.4746

Table 2. Unaxial and biaxial non-dimensional buckling load factors of (0/90/0) rectangular plate (b/h= 10 and E_1/E_2=40)

	Unaxial				**Biaxial**			
a/b	**Setodeh**	**Akavci**	**Ansys [Fem]**	**Present Study**	**Setodeh**	**Akavci**	**Ansys [Fem]**	**Present Study**
1	22.234	22.115	22.514	22.334	9.942	9.953	9.955	10.208
2	16.424	16.308	18.122	16.450	3.269	3.261	3.328	3.290

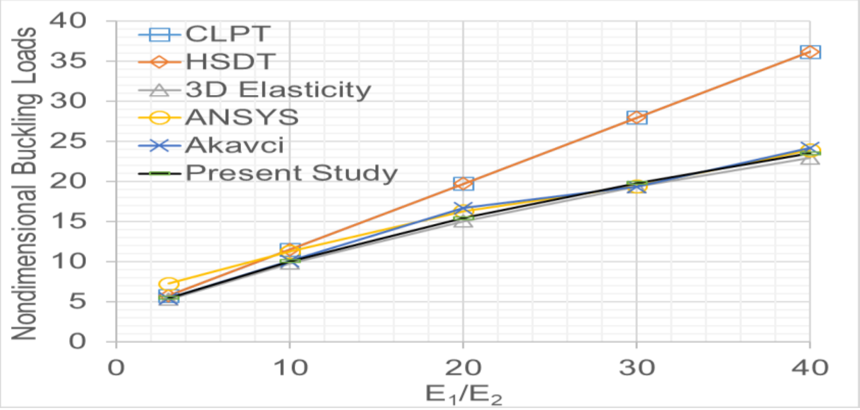

Fig. 3. Effect of orthotropy ratio on the uniaxal buckling load factor of a square symmetrically [0/90/90/0] laminated plate.

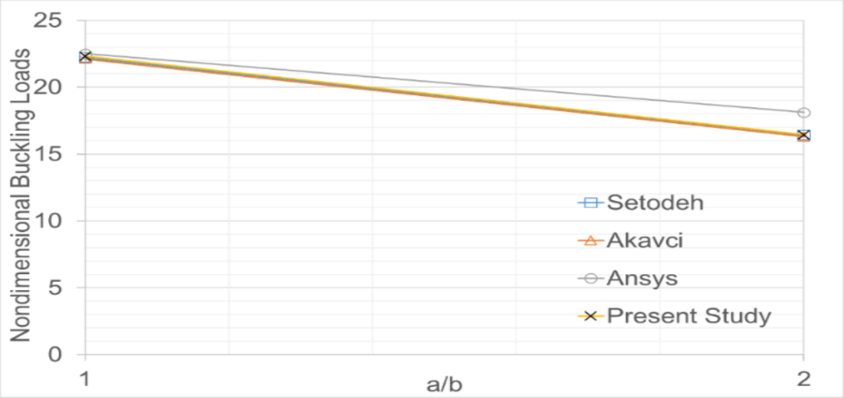

Fig. 4. Effect of edge ratio on the uniaxal buckling load factor of [0/90/0] laminated plate.

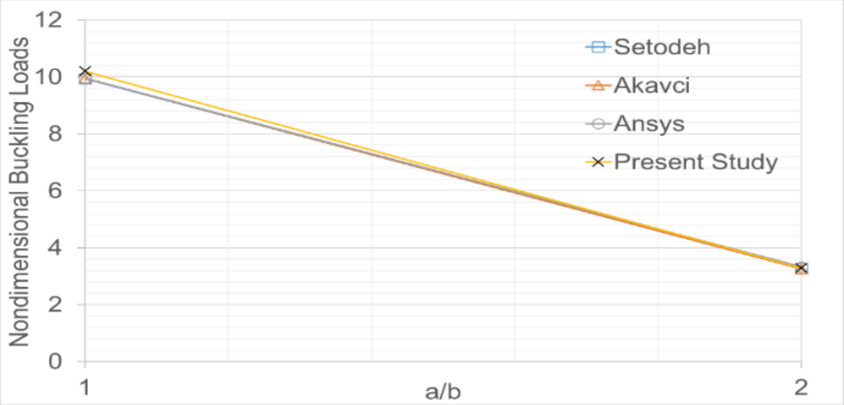

Fig. 5. Effect of edge ratio on the biaxal buckling load factor of [0/90/0] laminated plate.

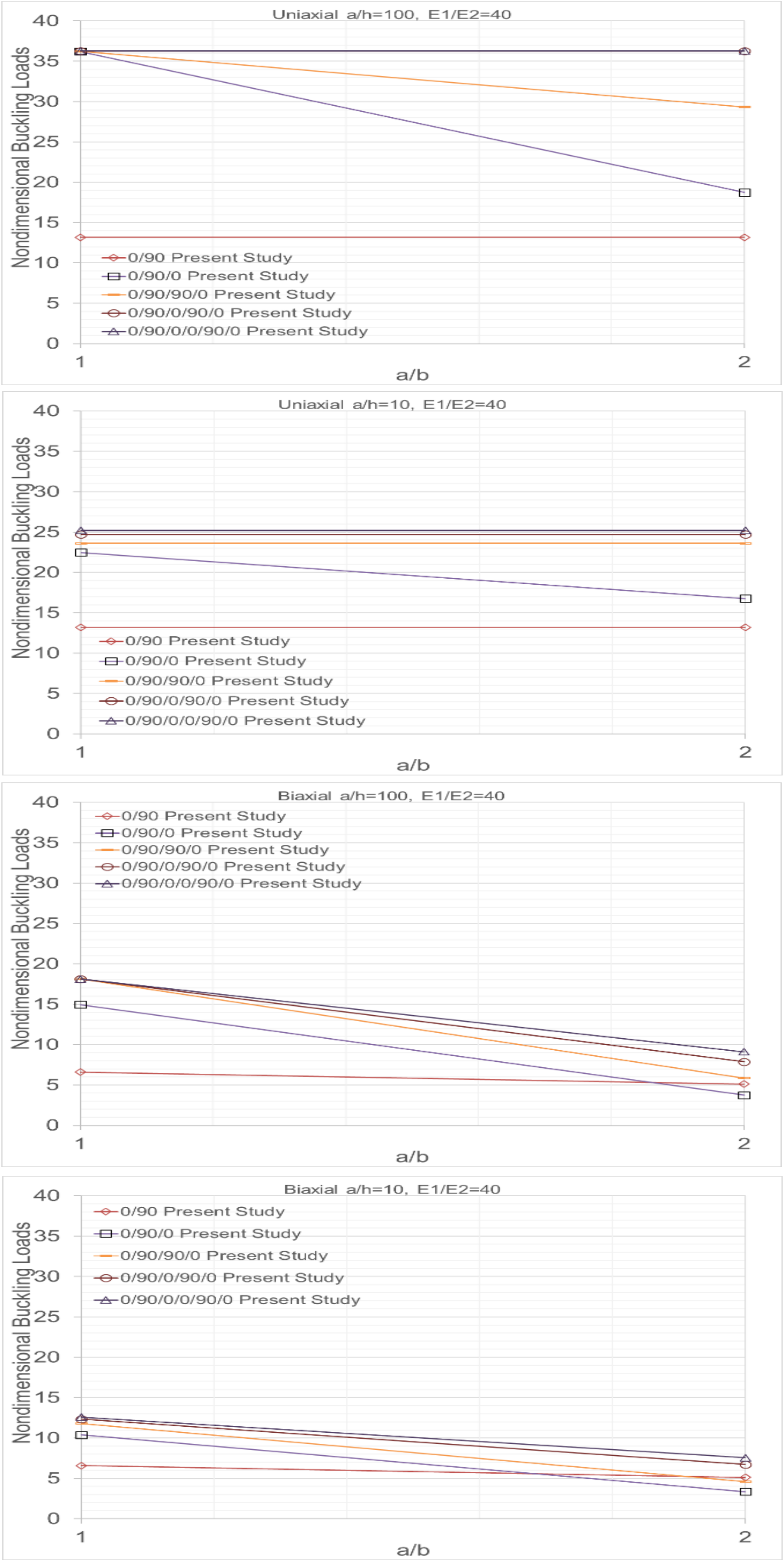

Fig. 6. Effect of edge ratio on the uniaxial and biaxal buckling load factor of various laminated sequence.

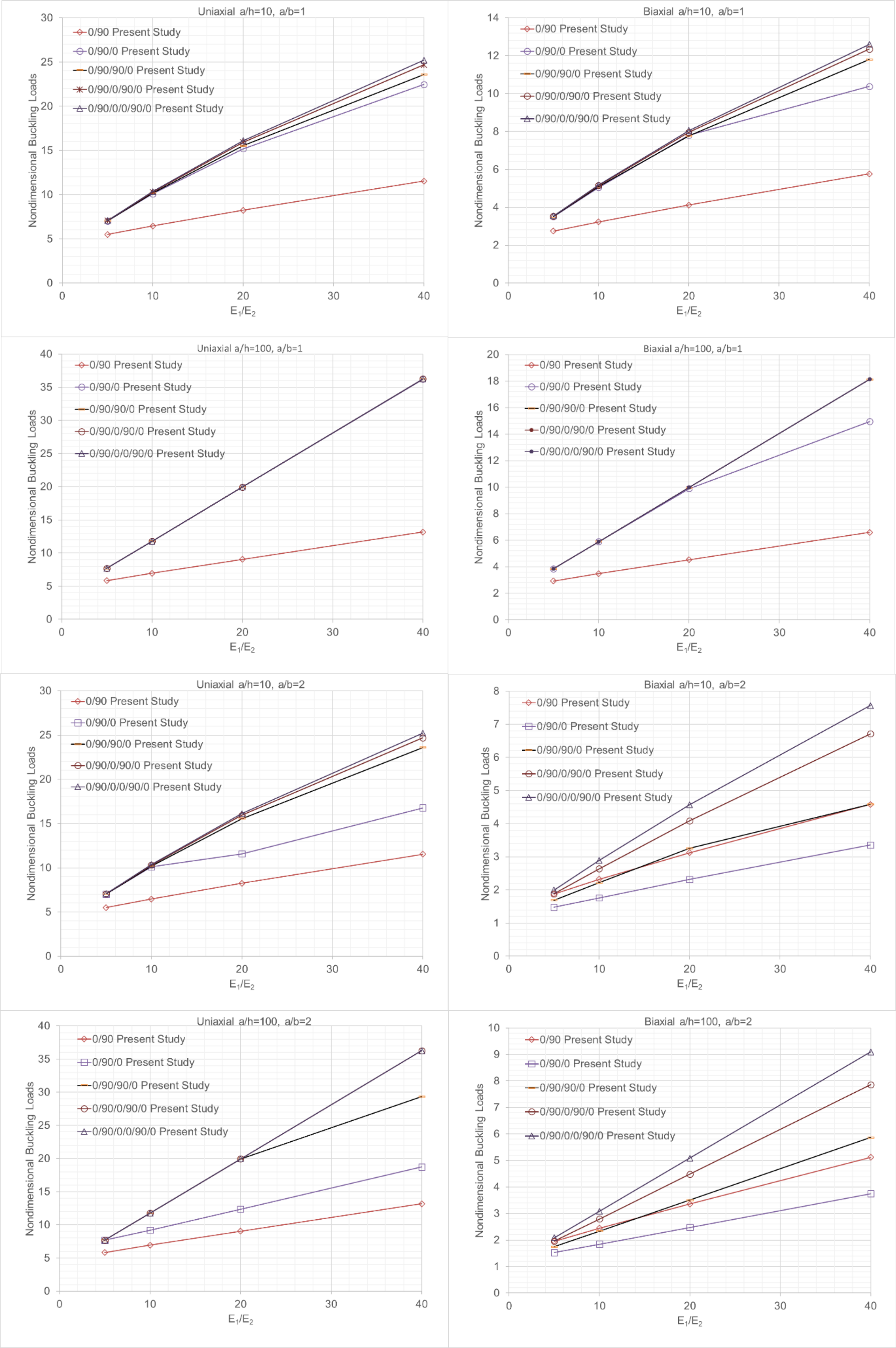

Fig. 7. Effect of anisotropy ratio on the uniaxial and biaxal buckling load factor of various laminated sequence

4. CONCLUSION

In this study, buckling analysis of symmetrically (LCP) resting is theoretically investigated. By applying Hamilton's principle, the governing equation for thick LCP is obtained. The solutions are gathered by using Navier solution method. The effects of a/b, E_1/E_2 ratios on buckling loads are examined. The most important observations and results are summarized as follows:

- The non-dimensional buckling load factors obtained for present study seem to be compatible with other study.
- The a/b, E_1/E_2 ratios, are playing a crucial role on buckling loads.
- The non-dimensional buckling load factors generally decrease when the ratio of a/b change from 1 to 2.
- The non-dimensional buckling load factors increase when the ratio of E_1/E_2 change from 3 to 40.
- The number of layer increases, the non-dimensional buckling load factors obtained by present study increase as well.

REFERENCES

Akavci SS, Yerli HR, Dogan A., 2007. The first order shear deformation theory for symmetrically laminated composite plates on elastic foundation. Arab J Sci Eng.32,341-8.

Akavci SS., 2014. Thermal buckling analysis of functionallygraded plates on an elastic foundation according to a hyperbolic shear deformation theory. Mech Compos Mater. 50(2), May, 2014 (Russian Original 50(2), March-April, (2014).

Akavci SS., 2007. "Buckling and Free Vibration Analysis of Symmetric and Antisymmetric Laminated Composite Plates on an Elastic Foundation" Journal of Reinforced Plastics and Composites. 26(18), p.1907-1919.

Dogan A, Arslan HM, Yerli HR., 2010. Effects of anisotropy and curvature on free vibration characteristics of laminated composite cylindrical shallow shells. Struct Eng Mech.35(4),493-510.

Dogan A, Arslan HM., 2012. Investigation of the effect of shell plan-form dimensions on mode-shapes of the laminated composite cylindrical shallow shells using SDSST and FEM. Steel and Composite Structures, An Int\'l Journal. 12(4),303-24.

Dogan A, 2019. Buckling Analysis of Symmetric Laminated Composite Plates. International Conference on Innovation, Sustainability, Technology and Education in Civil Engineering iSTE-CE'2019-13-15 June, 2019, Iskenderun, Hatay/TURKEY, 1360-1367.

Noor AK., 1975. Stability of Multilayered Composite Plates, Fibre Science Technology, 8(2), p.81-89.

Phan, N.D. ,Reddy, J.N. 1985. Analysis of Laminated Composite Plates Using a Higher-order Shear Deformation Theory. International Journal for Numerical Methods in Engineering. 21, p. 2201-2219.

Qatu M. S., Leissa A. W. 1991.Free vibrations of completely free doubly-curved laminated composite shallow shells, Journal of Sound and Vibration, Vol.151, No.1, pp.9-29.
Qatu MS., 2004. Vibration of laminated shells and plates. Elsevier, Netherlands.

Reddy JN, Khdeir AA., 1989. Buckling and vibration of laminated composite plates using various plate theories. AIAA J.12,1808–17.

Reissner E., 1945. The effect of transverse shear deformation on the bending of elastic plates. J Appl Mech.12, 69–77.

Sayyad A, Ghugal Y., 2014. "Buckling and free vibration analysis of orthotropic plates by using exponential shear deformation theory". Latin American Journal of Solids and Structures., 11, p.1298-1314.

Setoodeh, A. R., Karami, G. 2004. "Static, Free Vibration and Buckling Analysis of Anisotropic Thick Laminated Composite Plates on Distributed and Point Elastic SupportsUsing a 3-D Layer-wise FEM." Engineering Structures. 26, p.211-220.

Sophy M., 2013. Buckling and free vibration of exponentially graded sandwich plates resting on elastic foundations under various boundary conditions. Compos Struct.99,76-87.

TUJE

CONTENTS

ISSN 2587-1366

TURKISH JOURNAL OF ENGINEERING

VOLUME 4 ISSUE 4 OCTOBER 2020